# Gold nanoparticles meet medical radionuclides

Daems, Noami; Michiels, Carine; Lucas, Stéphane; Baatout, Sarah; Aerts, An

*Published in:*
Nuclear Medicine and Biology

*DOI:*
10.1016/j.nucmedbio.2021.06.001

*Publication date:*
2021

Nuclear Medicine and Biology 100–101 (2021) 61–90

Contents lists available at ScienceDirect

Nuclear Medicine and Biology

journal homepage: www.elsevier.com/locate/nucmedbio

# Gold nanoparticles meet medical radionuclides

Noami Daems [a,*], Carine Michiels [b], Stéphane Lucas [c], Sarah Baatout [a], An Aerts [a]

[a] Radiobiology Research Unit, Interdisciplinary Biosciences, Institute for Environment, Health and Safety, Belgian Nuclear Research Centre (SCK CEN), Boeretang 200, 2400 Mol, Belgium
[b] Unité de Recherche en Biologie Cellulaire-NARILIS, University of Namur, Rue de Bruxelles 61, 5000 Namur, Belgium
[c] Laboratory of Analysis by Nuclear Reaction (LARN)-NARILIS, University of Namur, Rue de Bruxelles 61, 5000 Namur, Belgium.

ARTICLE INFO

*Article history:*
Received 2 February 2021
Received in revised form 25 May 2021
Accepted 4 June 2021
Available online xxxx

*Keywords:*
Radiosensitization
Dose enhancement
Targeted radionuclide therapy
Cancer theranostics
Nuclear medicine
Nanobrachytherapy

ABSTRACT

Thanks to their unique optical and physicochemical properties, gold nanoparticles have gained increased interest as radiosensitizing, photothermal therapy and optical imaging agents to enhance the effectiveness of cancer detection and therapy. Furthermore, their ability to carry multiple medically relevant radionuclides broadens their use to nuclear medicine SPECT and PET imaging as well as targeted radionuclide therapy. In this review, we discuss the radiolabeling process of gold nanoparticles and their use in (multimodal) nuclear medicine imaging to better understand their specific distribution, uptake and retention in different *in vivo* cancer models. In addition, radiolabeled gold nanoparticles enable image-guided therapy is reviewed as well as the enhancement of targeted radionuclide therapy and nanobrachytherapy through an increased dose deposition and radiosensitization, as demonstrated by multiple Monte Carlo studies and experimental *in vitro* and *in vivo* studies.



**Contents**



*Abbreviations:* AuCBs, gold core nanoballs; AuNCages, gold nanocages; AuNCs, gold nanoclusters; AuNPs, gold nanoparticles; AuNR, gold nanorod; AuNS, gold nanoshells; CLI, Cerenkov luminescent imaging; Ctxb, Cetuximab; (c)RGD, (cyclic) Arginine-glycine-aspartate; CXCR4, C-X-C chemokine receptor type 4; DEF, dose enhancement factor; DOTA, dodecane tetraacetic acid; DTPA, diethylenetriaminepentaacetic acid; EBRT, external beam radiotherapy; ECM, extracellular matrix; EDTA, ethylenediaminetetraacetic acid; EGCg, pigallocatechin-gallate; EGF, epidermal growth factor; EGFR, epidermal growth factor receptor; EPR, enhanced permeability and retention; GA, gum arabic; GnRH, gonadotropin releasing hormone; GRP, gastrin-releasing peptide receptor; HYNIC, hydrazinonicotinamide; IA, intra-arterial; ICP-MS, inductively coupled plasma-mass spectrometry; IONP, iron oxide nanoparticle; IP, intraperitoneal; IT, intratumoral; IV, intravenous; LET, linear energy transfer; L/M, lung-to-muscle ratio; MMP9, matrix metallopeptidase 9; MRI, magnetic resonance imaging; PA, photo-acoustic; PEG, polyethylene glycol; PET, positron emission tomography; p.i., post-injection; PSMA, prostate-specific membrane antigen; PTT, photo-thermal therapy; RES, reticuloendothelial system; SERS, surface-enhanced Raman scattering; SLNs, sentinel lymph nodes; SPECT, Single photon emission computed tomography; SPR, surface plasmon resonance; TAT-Bn, TAT-bombesin; TRT, targeted radionuclide therapy; T/B, tumor-to-background ratio; T/Bl, tumor-to-blood ratio; % ID, percentage of injected dose.

* Corresponding author at: Boeretang 200, 2400 Mol, Belgium.
*E-mail address:* noami.daems@sckcen.be (N. Daems).

https://doi.org/10.1016/j.nucmedbio.2021.06.001

## 1. Background

### 1.1. An introduction in nuclear medicine

Nuclear medicine involves the internal administration of radionuclides to diagnose, stage, treat and follow-up of diseases, including cancer. Radiopharmaceuticals are developed by linking a radionuclide to a carrier molecule (also referred to the targeting molecule), which is directed against a cancer-specific antigen or process. The selection of the suitable radionuclide depends on its specific emission and the intended application [1]. In more detail, positron ($\beta^+$ particles)- and gamma-emitting radionuclides enable 3D positron emission tomography (PET) and single photon emission computed tomography (SPECT) imaging, respectively. Consequently, the radiopharmaceutical can be traced inside the body providing functional information about specific molecular and cellular processes in the tumor depending on the carrier molecule, such as blood flow, metabolism, receptor expression, tumor metastatic capacity, inflammation, programmed cell death. On the other hand, radionuclides emitting $\beta^-$ particles (e.g. iodine-131, lutetium-177, yttrium-90), $\alpha$-particles (e.g. actinium-225, astatine-221, bismuth-213, lead-212) or Auger electrons (e.g. iodine-125, iodine-123, indium-111, terbium-161, gallium-67), which are coupled to a cancer-targeting molecule, have the potential to deliver a cytotoxic radiation dose to the cancer cells. This therapeutic strategy is called targeted radionuclide therapy (TRT). TRT is a rapidly growing field. Some recent examples are the development of radiolabeled prostate-specific membrane antigen (PSMA) and the approval of [$^{177}$Lu]Lu-DOTA-TATE to treat neuroendocrine tumors [2–4]. However, research continues to investigate how to maximize the benefit of radionuclide therapies that are effective and safe for each individual patient [5].

### 1.2. The potential advantages of nanoparticles in nuclear medicine

A 'nanomaterial' is defined as a natural, incidental or manufactured material with one or more external dimensions in the size range of 1 nm to 100 nm. In this size range, material properties become controllable [6]. Hence, nanoparticles can arise in several shapes, such as spheres, rods, discs, cubes and cages. Furthermore, as the size of the nanoparticles decreases, their surface area-to-volume ratio is strongly increasing. Thanks to these specific properties, nanoparticles can offer a significant contribution to nuclear medicine.

First, a major advantage is the potential of a single nanoparticle to hold multiple radionuclides, achieving much higher payloads of radioactivity as compared to a conventional radiopharmaceutical agent that carries only one or a few radionuclides (Fig. 1A). In fact, Lucas, et al. calculated in a Monte Carlo simulation that nanoparticles containing multiple $\beta^-$emitters (yttrium-90, lutetium-177, iodine-131, iodine-124 or rhenium-188) may deliver a total absorbed radiation dose of >60 Gy to a solid, non-small-cell lung carcinoma model, which could not be achieved by antibodies that were each conjugated to a single radionuclide [7]. The number of radionuclides needed per nanoparticle to achieve 100% tumor control strongly depends on the physical properties of the radionuclide (the physical half-life, the radiation energy and the penetration depth) and on the biological properties of the nanoparticles and the tumor (tumor size, the intra-tumoral distribution, the biological half-life and the uptake kinetics of the nanoparticles).

Second, the predominant theory is that due to their small size, nanoparticles can efficiently extravasate through the gaps between endothelial cells of the leaky and immature blood vessels into the tumor mass. Furthermore, the decreased level of lymphatic drainage of the interstitial fluid within the tumor contributes to the nanoparticle tumor retention. This rationale is known as the enhanced permeability and retention (EPR) effect and causes the accumulation and prolonged retention of radiolabeled nanoparticles in the tumor tissue, increasing the tumor radiation dose [8,9]. However, it is important to point out that despite the EPR effect is tremendously succesful in preclinical animal models, the clinical efficacy and translation of cancer nanomedicines remains poor, indicating that the EPR phenomenon is less reliable in human cancers [10–13]. Therefore, interest is growing in the extravasation of nanoparticles into tumors via active transendothelial pathways, which appears not to be underestimated. In fact, Sindhwani, et al. demonstrated a very low frequency of interendothelial gaps in different xenograft models, such as U87-MG glioblastoma, 4T1 breast cancer, genetically engineered MMTV-PyMT breast cancer and patient derived breast cancer, as well as in biopsies of human ovarian, breast and glioblastima tumors. In contrast, fenestrae and vacuoles, which are associated with endothelial transcytosis, occur much more frequently in the tumor vasculature across all models. Furthermore, by deactivating active transendothelial transport pathways, the authors concluded that only 3–25% of nanoparticle tumor entry is attributed to the passive transport through gaps, depending on the nanoparticle size [14].

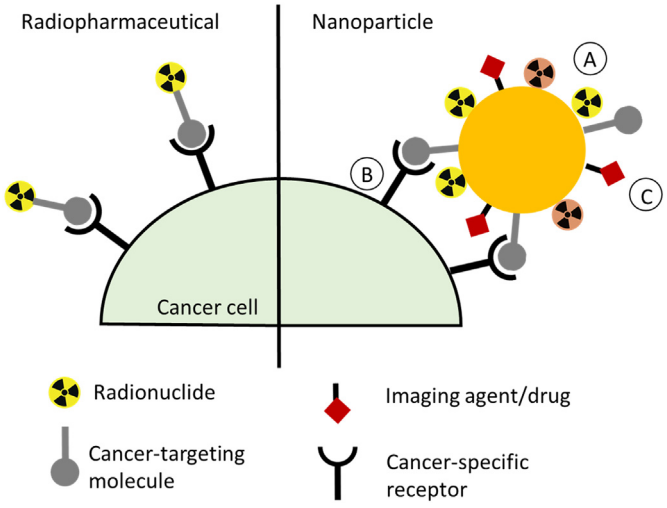


**Fig. 1.** The advantages of nanoparticles in nuclear medicine. (A) The delivery of a high payload of radionuclides. (B) Passive enhanced permeability and retention accumulation and the active multivalent binding of targeting moieties to cancer-specific receptors. (C) Functionalization with additional chemotherapeutic drugs and/or imaging molecules.

Third, the large surface area-to-volume ratio of nanoparticles facilitates the functionalization of the nanoparticle surface with multiple cancer targeting molecules, which creates a multivalent effect, promoting an efficient binding to the tumor cells (Fig. 1B). As a result, the use of targeted nanoparticles could enhance the delivery of radioactivity to the tumor, which in turn leads to an improved therapeutic efficacy [7,15,16].

Besides the use of cancer targeting molecules, conjugation of other functional moieties to the nanoparticle surface, such as imaging agents and chemotherapeutic drugs (Fig. 1C) allows the combination of therapeutic and diagnostic applications, a field called 'theranostics'. Theranostic nanoparticles allow a non-invasive and real-time tracking of the *in vivo* distribution of the nanomaterials and can facilitate the dose and toxicity management [17].

### *1.3. The benefits of gold nanoparticles in cancer detection en therapy*

In addition to the conjugation to multiple functional moieties and the labeling with radionuclides as described above, the use of gold nanoparticles (AuNPs) as radionuclide carrier in nuclear medicine has additional benefits (Fig. 2).

#### *1.3.1. Surface plasmon resonance*

One of the most important characteristics of AuNPs involves the surface plasmon resonance (SPR), which occurs when incident light of a specific wavelength causes a collective and coherent oscillation of free surface electrons, resulting in the extinction of light and the generation of heat. As a result, the SPR peak of AuNPs makes them interesting tools for therapeutic applications, such as photo-thermal therapy (PTT) as well as for optical imaging applications such as photo-acoustic (PA) imaging and surface-enhanced Raman scattering (SERS) [8,18–20]. In short, due to the conversion of light into heat, AuNPs can efficiently induce localized hyperthermia in the tumor tissue, causing irreversible damage to the tumor cells [21]. In addition, the heat production causes a thermo-elastic expansion of the AuNPs and the subsequent emission of acoustic transients, which can be probed by a transducer to construct photo-acoustic images [22,23]. Finally, Raman scattering is the inelastic and specific scattering of photons when they interact with molecules. The SPR of AuNPs during photon irradiation locally increases the electromagnetic field in the proximity of the nanoparticle surface, dramatically enhancing the Raman scattering of a conjugated Raman-active reporter [24,25].

#### *1.3.2. High atomic number of gold*

Second, AuNPs exhibit a high atomic number (Z = 79), causing the preferential absorption of X-ray photons by the AuNPs compared to soft tissue. As a result, introducing AuNPs into the body increases the X-ray attenuation and thus the contrast of the X-ray based images. Currently, iodine-based compounds are the most frequently used contrast agents. However, their rapid renal clearance requires short imaging times and potential catherisation. Furthermore, the increased kidney retention of the contrast media can increase the risk on renal injury. An additional shortcoming of the iodine-based compounds is the relatively high viscosity and high osmolality, due to the presence of only 3–6 iodine atoms per molecule, which potentially causes a poor patient tolerance. In contrast, 1.9 nm sized AuNPs contain 250 gold atoms per particle, and thus exhibit a much lower osmolality and viscosity at the same elemental concentration as the iodine agents. Furthermore, the higher molecular weight of the AuNPs causes a slower blood clearance as compared to the iodine agents, permitting longer imaging times after IV injection. Finally, gold has a higher atomic number and absorption coefficient (79 and 5.16 $cm^2/g$ at 100 keV, respectively) as compared to iodine (53 and 1.94 $cm^2/g$ at 100 keV, respectively) [26].

In addition, the high atomic number of AuNPs provides a benefit in radiotherapy. Indeed, the high atomic number of AuNPs causes several interactions to occur between the X-ray photons and the AuNPs. These include the photoelectric effect, Compton scattering and pair production, which release a burst of secondary electrons, enhancing the radiation dose deposition inside the tumor volume and thus increasing the effectiveness of radiotherapy [27]. As a result, radiolabeled gold nanoparticles have the potential to enhance the dose deposition of the radionuclides, improving the effectiveness of internal radionuclide therapy.

#### *1.3.3. Biological effects of gold nanoparticles*

Importantly, besides their ability to increase the dose deposition upon irradiation, AuNPs can also cause biological effects in cancer cells. Fig. 3 shows potential biological radiosensitization mechanisms of AuNPs. For example, AuNPs can catalyze the production of ROS and

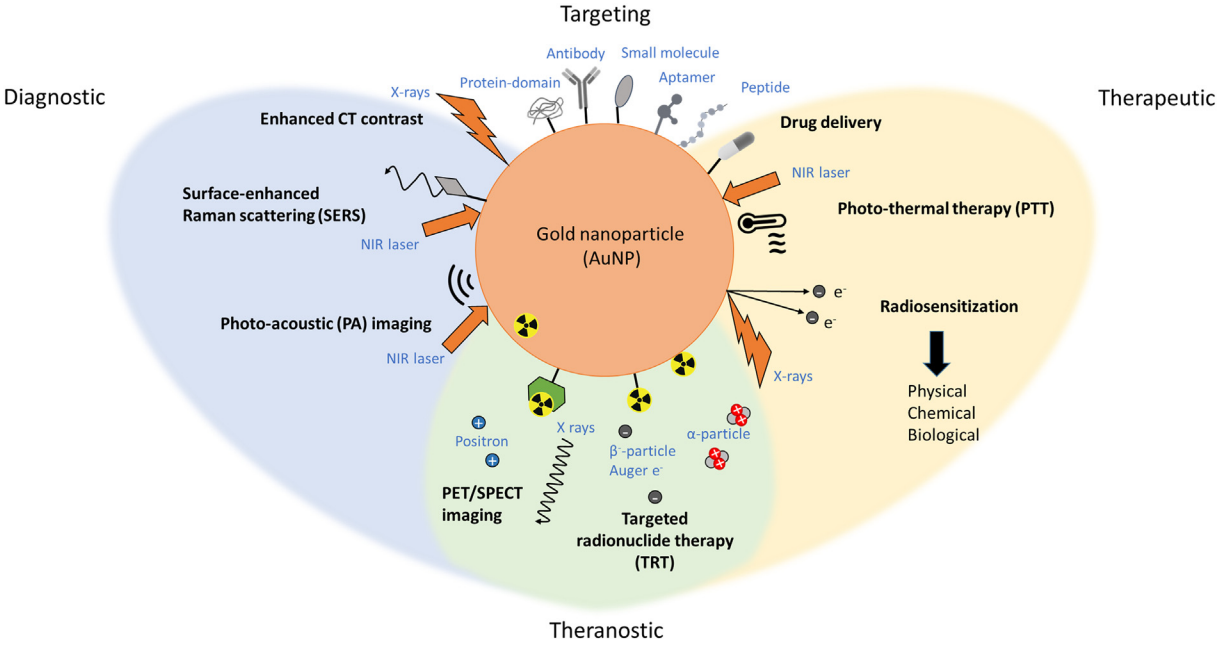


**Fig. 2.** Multifunctional AuNPs and their potential applications in the diagnosis and treatment of cancer. NIR: Near-infrared radiation.

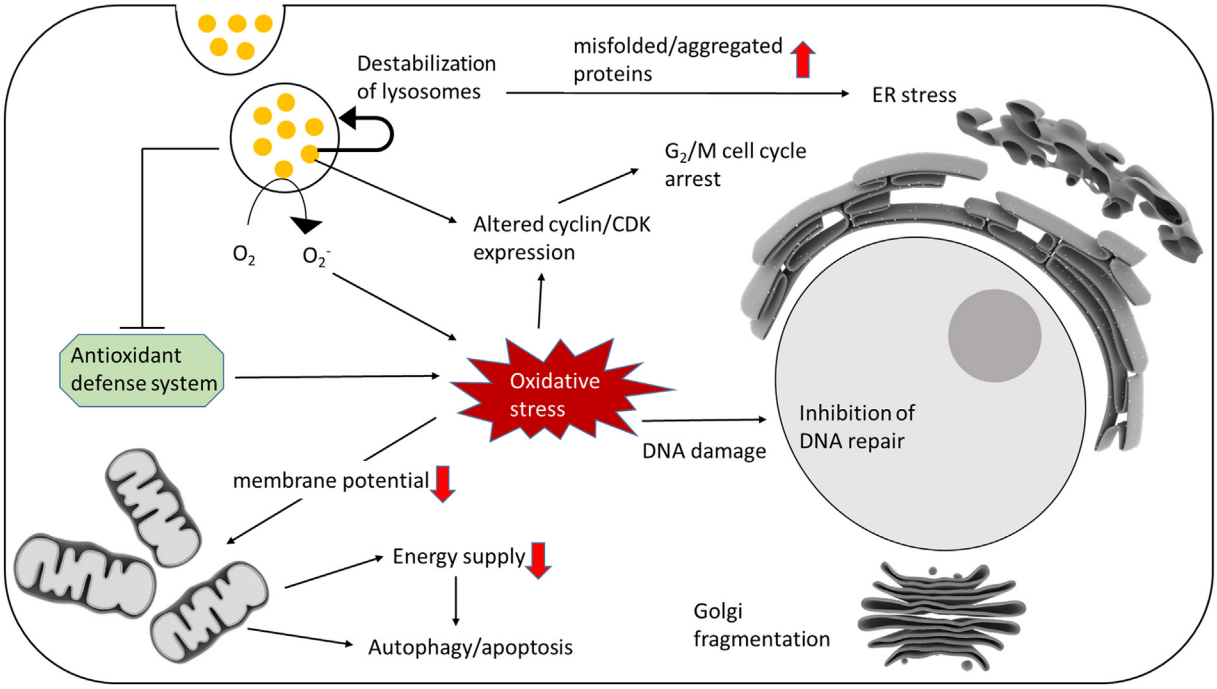


**Fig. 3.** Different potential biological radiosensitization mechanisms of gold nanoparticles. Based on [28] and [196]. (For interpretation of the references to colour in this figure legend, the reader is referred to the web version of this article.)

inhibit antioxidant defense systems. As a result, oxidative stress can cause mitochondrial dysfunction, DNA damage, autophagy, apoptosis and $G_2$/M cell cycle arrest, which is the most radiosensitive cell cycle phase. On the other hand, AuNPs could also inhibit DNA repair mechanisms or destabilize lysosomes, which increases the abundance of misfolded and aggregated proteins, causing ER stress. [28–42]. As a result of these biological effects of AuNPs, cancer cells might have a reduced capacity to respond adequately to ionizing radiation and are thus more sensitive to radiotherapy.

In conclusion, radiolabeled AuNPs do not only have the ability to improve nuclear medicine imaging and therapy by carrying a higher payload of radionuclides and accumulate in the tumor tissue, but also allows the combination of multiple optical imaging modalities to improve cancer detection and follow-up. On the other hand, combining multiple treatment modalities, such as targeted radionuclide therapy, photothermal therapy and (biological, chemical and physical) radiosensitization, can synergize the efficacy of the anticancer therapy to combat radio-resistant and/or chemo-resistant cancer cells [43].

In this review, we will give a broad overview on the radiolabeling of gold nanoparticles and their potential to improve cancer nuclear imaging and treatment, taking into account the intratumoral uptake, retention, biodistribution and the administration method. Furthermore, we will review the dose enhancement and radiosensitizing potentials of AuNPs in targeted radionuclide therapy and nanobrachytherapy. The potentials of radiolabeled AuNPs are often studies in different cancer models *in vitro* and *in vivo*, which are summarized in Fig. 4.

## 2. Radiolabeling of gold nanoparticles

The radionuclides that are used to radiolabel AuNPs and that are mentioned in this review are in further detail described in Table 1.

Importantly, a stable association between the radionuclide and the nanoparticle is essential for the successful implementation of radiolabeled nanoparticles in cancer diagnosis and therapy. Loss of the radionuclide can result in its accumulation in non-targeted tissues [45]. In literature, several methods for nanoparticle radiolabeling have been described (Fig. 5).

A frequently used strategy is the use of bifunctional chelators, which strongly complex radiometals. The bifunctional chelators can be directly attached to the AuNPs via thiolated linkers, for example consisting out of a glycine-glycine sequence acting as spacer followed by a cysteine res-

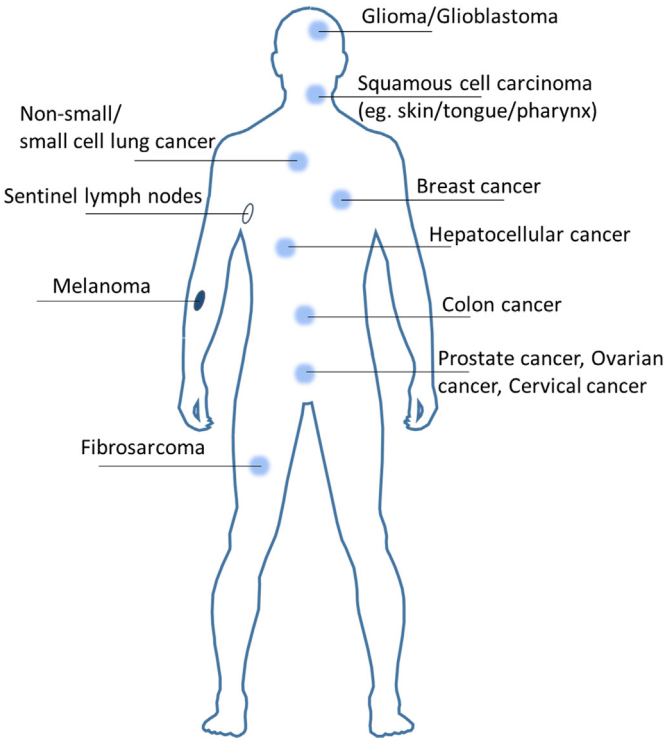


**Fig. 4.** Commonly used cancer types in research to assess the potential of radiolabeled AuNPs in nuclear medicine imaging and therapy.

**Table 1**
Useful medical radioisotopes for diagnosis and treatment of cancer-related diseases [44–48].

| Isotope | Simplified decay | Daughter nuclide | Half-life | Particle Energy (MeV) | Photon energy MeV (%) | Main clinical usage |
|---|---|---|---|---|---|---|
| Technetium-99m | γ | Ruthenium-99 | 6 h | / | 0.141 (98.6%) | Used for common diagnostic procedures |
| Astatine-211 | α<br>EC | Bismuth-207 (unstable)<br>Polonium-211 (unstable) | 7.2 h | 5.87<br>7.45 | / | Under investigation for targeted alpha therapy |
| Yttrium-90 | $\beta^-$ | Zirconium-90 | 64.1 h | 2.28 (100%) | / | Microspheres for SIRT of liver cancer |
| Iodine-131 | $\beta^-$ | Xenon-131 | 8.02 d | 0.607 (89.6%) | 0.365 (81.5%) | Treatment of hyperthyroidism, thyroid carcinoma and NETs |
| Lutetium-177 | $\beta^-$ | Hafnium-177 | 6.73 d | 0.498 (79%) | 0.208 (11%) | Treatment of prostate cancer and NETs |
| Iridium-192 | $\beta^-$<br>EC | Platina-192<br>Osmium-192 | 73.8 d | 0.672 (47.9%) | 0.468 (47.8%) | High-dose rate brachytherapy |
| Gold-198 | $\beta^-$ | Mercury-198 | 2.69 d | 0.960 (99%) | 0.412 (96%) | Brachytherapy |
| Iodine-125 | EC | Tellurium-125 | 59.5 d | / | 0.035 (7%) | Low-dose rate brachytherapy |
| Indium-111 | EC | Cadmium-111 | 2.8 d | / | 0.245 (94%) | Scintigraphy of NETs |
| Zirconium-89 | $\beta^+$<br>EC | Yttrium-89 | 3.27 d | 0.897<br>(23%) | 0.909<br>(99.9%) | Under investigation for PET imaging |
| Fluorine-18 | $\beta^+$<br>EC | Oxygen-18 | 1.83 h | 0.634 (97%) | / | Routinely used in the form of 2-[$^{18}$F]FDG as PET-CT imaging in cardiology, neurology and oncology |
| Copper-64 | $\beta^+$/EC<br>$\beta^-$ | Nickel-64<br>Zinc-64 | 12.7 h | $0.653_{\beta+}$ (17.5%)<br>$0.579_{\beta-}$ (38.5%) | 1.346 (0.47%) | Under investigation for PET imaging |
| Iodine-124 | $\beta^+$<br>EC | Tellurium-124 | 4.2 d | 2.137<br>(23%) | 0.603<br>(63%) | PET-CT in thyroid cancer |
| Palladium-103 | EC | Rhodium-103 | 17 d | / | 0.0397<br>(0.07%) | Brachytherapy permanent implant seeds |
| Actinium-225 | α<br>$\beta^-$ (later in decay) | Francium-211 (unstable) | 10 d | 5.8–8.4 (α)<br>0.6–2.0 ($\beta^-$) | 0.218 (11.4%)<br>0.440<br>(25.9%) | Under investigation for targeted alpha therapy |
| Ytterbium-169 | EC | Thulium-169 | 32 d | / | 0.06312<br>(44.05%) | High-dose rate brachytherapy |

**Abbreviations:** CT: computed tomography; EC: electron conversion; FDG: fluorodeoxyglucose; NET: neuroendocrine tumor; PET: positron emission tomography; SIRT: selective internal radiation therapy; SPECT: single-photon emission tomography.

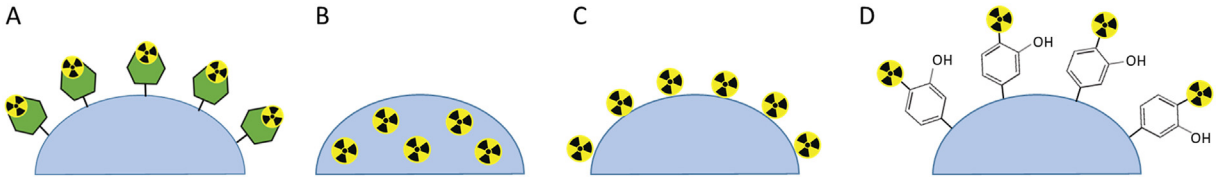


**Fig. 5.** Radiolabeling of nanoparticles by (A) chelation, (B) incorporation, (C) chemisorption and (D) covalent binding. Based on [45].

idue providing an active thiol group, which interacts with the AuNP surface [49–52]. In addition, the bifunctional chelators can be indirectly attached to the AuNPs via a covalent bond to the nanoparticle coating or to the vector molecule. In the development of radiopharmaceuticals, a successful bifunctional chelator minimizes the dissociation of the radionuclide from the chelator *in vivo*. This depends on the thermodynamic stability and the kinetic inertness of the bifunctional chelator. The thermodynamic stability reflects the direction of the dissociation reaction, while the kinetic inertness reflects the rate of the dissociation reaction. Two well-known bifunctional chelators are diethylenetriaminepentaacetic acid (DTPA) (Fig. 6A) and dodecane tetraacetic acid (DOTA) (Fig. 6B). Generally, the 'open-chain', acyclic structure of DTPA is typically characterized by fast dissociation kinetics and radiometal complexation. As a result, DTPA analogs rapidly achieve a high radiochemical yield under mild reaction conditions. The radiochemical yield is defined as the amount of activity in the product expressed as the percentage of the starting activity. A high radiochemical yield is required to obtain a high specific activity, which in turn is desirable for therapeutic applications [54,55]. However, the fast dissociation rate and the lower thermodynamic stability of DTPA might result in the release of the radionuclide when applied in biological solutions. Conversely, due to their 'caged', macrocyclic construction, DOTA analogs display a higher thermodynamic stability and are much more kinetically inert compared to DTPA analogs, creating radiometal-DOTA complexes that are more likely to retain their chemical integrity in the presence of natural chelators [53]. However, the radiolabeling kinetics of DOTA analogs are much slower, requiring elevated temperatures and a longer reaction time to achieve a high yield, which might affect the integrity of the biomolecules to which it is linked [56]. DOTA and DTPA analogs are often used to chelate lutetium-177, indium-111, copper-64 and yttrium-90, radioisotopes suitable for radionuclide therapy [57–61]. On the other hand, technetium-99m is an ideal radioisotope for SPECT imaging because of its low γ-radiation energy (140 keV) and short half-life (6.02 h). Next to DTPA and DOTA, hydrazinonicotinamide (HYNIC) is a suitable chelator to radiolabel

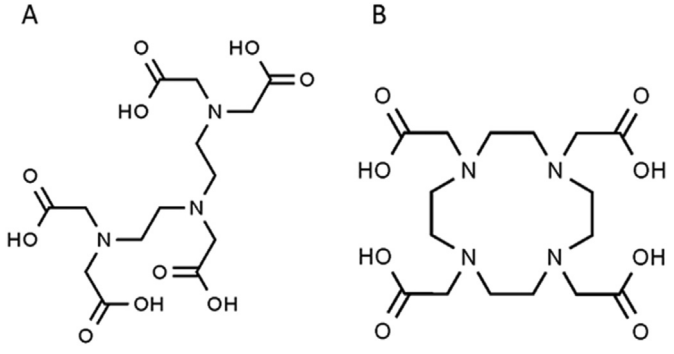


**Fig. 6.** Molecular structure of (A) diethylenetriaminepentaacetic acid (DTPA) and (B) dodecane tetraacetic acid (DOTA).

AuNPs with technetium-99m. In the presence of co-ligands, HYNIC forms monodentate or bidentate coordination bonds with technetium-99m, achieving a high radiochemical yield and stability [51,52,62,63]. Together with a good radiochemical yield and radiochemical stability, a high radiochemical purity, which measures the presence of other radionuclides within radiopharmaceutical sample, is a key property of the radiolabeled nanopharmaceutical product as a diagnostic or therapeutic agent in nuclear medicine. The radiochemical yield of radionuclides attached to AuNPs by using bifunctional chelators can widely range between 30% and >90%. After purification, the radiochemical purity is always higher than 95%. The stability can vary from 80% to >95% when incubated in serum during 24-72 h [51,52,57–60,64–67].

In order to avoid harsh radiolabeling conditions, possible instability and trans-chelation of the radionuclide, several studies preferred a chelator-free radiolabeling method, incorporating copper-64 and radioactive gold (gold-198 and gold-199) into the AuNPs during the production process [68–76]. $^{64}$Cu-doped AuNPs are reported with a radiochemical yield of nearly 100% after reduction of [$^{64}$Cu]$Cu^{2+}$ by hydrazine, which reduces to <30% without the use of hydrazine [72]. Furthermore, a stability of 90% to >95% is achieved when the $^{64}$Cu-doped AuNPs are challenged with ethylenediaminetetraacetic acid (EDTA) for 44–48 h [69,71]. In addition, they show 0–8% of degradation or trans-chelation in serum up to 24-48 h, while the stability of $^{64}$Cu[Cu]-DOTA is less stable [68,69,71]. Importantly, due to direct introduction of gold-199 or gold-198 into the reaction mixture of AuNPs production, the incorporation reaches a radiochemical yield as high as 80–96% [70,74]. In addition, after purification the radiochemical purity is 100%. In terms of the stability, $^{198}$Au-doped and $^{199}$Au-doped gold nanostructures show no dissociation of radioactive gold in serum during a week [70,74,76].

For radioiodination and radiofluorination of AuNPs, it is possible to covalently attach radioactive iodine (iodine-124, iodine-125 and iodine-131) and fluorine-18 to an aromatic phenol group via in situ oxidation and substitution [77]. In case of direct radiolabeling, the phenol group is present into the organic coating of the AuNPs or is provided by a tyrosine residue being part of an AuNP-conjugated peptide or antibody [78–84]. Indirect radiolabeling involves a linker molecule, which already carries the radiolabeled phenol group and facilitates its coupling to the AuNPs [85,86]. On the other hand, the phenol-free prosthetic probes [$^{18}$F]F-silicon and [$^{18}$F]F-bicyclononyne also effectively attach fluorine-18 to AuNPs [87,88]. Iodination and fluorination are both rapid radiolabeling methods achieving a radiochemical yield varying between 60% to >90% and after purification a purity of >95%. However, various studies observed some degree of radioiodine release resulting in a serum stability of the conjugate of 49–76.3% after 48-72 h [83,84]. As a result, the free radionuclides can accumulate in different organs and increase the dose in healthy tissues, such as in the thyroid, the stomach and the bladder [82]. To address this issue, Lee, et al. constructed a protective Au-shell around $^{124}$I-labeled AuNPs and showed that >98% of iodine-124 remained on the AuNPs for 48 h in human serum, while 'unprotected' AuNPs released 20% or more of iodine-124 [78–80,89,90].

Alternatively, the halogens iodine and astatine possess a strong affinity for the AuNP surface. As a result, radioactive iodine and the α-emitter astatine-211 could be attached to the AuNP surface via chemisorption [91–95]. Interestingly, Dziawer, et al. demonstrated that $^{211}$At-astatinated AuNPs exhibit a radiochemical yield of >99%, while $^{131}$I-iodinated AuNPs show a radiochemical yield ranging between 64% and >99%. Furthermore, the $^{211}$At-astatinated AuNPs demonstrate a better *in vitro* stability than $^{131}$I-iodinated and $^{125}$I-iodinated AuNPs in serum (99% vs 85%–93%) during 24 h [91,92,94,95]. Furthermore, it has been shown that the radioiodine adsorption strength onto the AuNP surface depends on the AuNP surface modifications and the incubation medium, which could lead to detachment of the radionuclides and hinder their applications *in vivo* [96]. In order to reduce iodine detachment from $^{131}$I-radiolabeled gold nanorods (AuNRs) *in vitro* and *in vivo*, Wang, et al. pre-oxidized radioactive Na[$^{131}$*I*]I via chloramine T or iodogen as oxidizing agents to convert sodium iodide to iodine. They demonstrated that the valence state of iodine significantly affects the adsorption strength of the radioiodine to AuNRs. Indeed, although both radiolabeled products have a labeling yield >90%, [$^{131}$I]I(0)-AuNRs exhibit a high radiochemical stability *in vitro* (98% in serum for 24 h), with only negligible uptake of radioiodine in the thyroid of treated mice and a high uptake in MCF-7 breast cancer cells. In contrast, [$^{131}$I]I(−1)-AuNRs release the iodine-131 (a stability of <75% in serum for 24 h), causing considerable uptake of iodine-131 in the thyroid and bladder of treated mice. To explain this result, the authors hypothesized that [$^{131}$I]I(−1) simply adsorbs onto the AuNRs, while [$^{131}$I]I(0) reacts with the AuNRs, forming a stronger bond [97].

## 3. Assessment of gold nanoparticles in nuclear medicine

### 3.1. Tumor uptake, retention and distribution

The inherent AuNP characteristics, such as their size, shape, and coating are determining factors that can affect the AuNP pharmacokinetics, biodistribution and tumor uptake. Therefore, these properties have to be carefully tuned in order to maximize the tumor uptake, the tumor-to-background ratio (T/B), and thus the effectiveness of radiolabeled AuNPs as diagnostic and therapeutic nano-radiopharmaceuticals. For this purpose, SPECT, PET and CT are useful imaging tools to better understand the *in vivo* behavior of radiolabeled AuNPs in real-time. In addition, inductively coupled plasma-mass spectrometry (ICP-MS), γ-counting and optical imaging, such as Raman scattering imaging, Cerenkov luminescence imaging, photoacoustic imaging and fluorescence imaging can be used to complement the nuclear imaging and to verify the quantity of AuNPs in the major organs and in the tumor [74,78,90,98–100]. Table 2 represents an overview of the studies using nuclear medicine imaging to assess the tumor uptake, retention and distribution of radiolabeled gold nanoparticles with respect to their specific characteristics and administration strategies.

#### 3.1.1. Pharmacokinetics and biodistribution

Following administration *in vivo*, the pharmacokinetics and biodistribution profile of targeted AuNP-based radiopharmaceuticals, carrying multiple targeting molecules, substantially differ from the monomeric radiopharmaceuticals lacking AuNPs (Fig. 7). For instance, the radiolabeled low-molecular weight monomers, [$^{99m}$Tc]Tc-RGD and [$^{64}$Cu]Cu-DOTA-polyethylene glycol (PEG) are cleared from the blood pool shortly after intravenous (IV) administration ($T_{1/2}$ < 10 min and 30 min, respectively), whereas [$^{99m}$Tc]Tc-AuNPs-RGD and [$^{64}$Cu]Cu-gold nanoshells (AuNS) exhibit a blood circulation $T_{1/2}$ of 47 min and 12.8 h, respectively. Arginine-glycine-aspartate or RGD is a peptide motif, which is displayed in many extracellular matrix (ECM) proteins and regulates cell-cell interactions and cell-ECM adhesion. The RGD peptide can be used as a targeting vector to bind integrins, such as integrin αvβ3, which is highly expressed on activated endothelial cells of the tumor neovasculature and on some tumor cells, such as melanoma, breast cancer, osteosarcoma and glioma [101]. The blood clearance of the small monomeric radiotracers is followed by early excretion, mainly via the kidneys and to a lesser extent via the hepatobiliary pathway, 0-20 h post-injection (Fig. 7 A-B) [102–105].

Unlike small molecules, high molecular weight targeting agents, such as antibodies, are not excreted via the renal system, but accumulate in the liver [64,106]. The most important difference in biodistribution pattern is the significantly higher uptake of the colloidal radiolabeled AuNP analogs in the liver, spleen and lungs, compared to the low-and high-molecular weight monomeric systems (Fig. 7 B–C) [51,64,103,106,107]. Excretion of the radiolabeled AuNPs can take place via both the renal system and the hepatobiliary system, depending on their size [51,68,103,104,107] (Fig. 7 A-B). However, Xie, et al. concluded that [$^{64}$Cu]Cu-AuNS are excreted via the hepatobiliary system at a slower pace than the monomeric controls [103]. This is potentially due to the sequestration of the AuNPs by

**Table 2**
Overview of radiolabeled gold nanoparticles under pre-clinical investigation for their nuclear imaging potentials.

| Isotope | Particle | Size (nm) | Functionalization | Labeling method | Cell model, administration | In vitro/in vivo | Application | Effect | Reference |
|---|---|---|---|---|---|---|---|---|---|
| Iodine-131 | [$^{131}$I]I-AuNPs-PEG-cRGD | 93.4 × 24.8 | Cyclic RGD | adsorption | B16F10, mouse skin melanoma (pos)<br>MCF-7, human breast cancer (neg)<br>IV, 1.5–7.4 MBq, 100 μl | In vivo | Targeted SPECT-CT, in vivo | % ID/g (pos): 3.6–4.0 - 5.1 \| T/M: 7.1–6.9 - 10.0 \| T/Bl: 1.0–0.8 -1.6 (1 h - 3 h - 6 h)<br>% ID/g (blocked): 2.2 \| T/M: 3.9 \| T/B: 0.6 (6 h)<br>% ID/g (neg): 1.3–1.8 -1.6 \| T/M: 2.2–3.3 - 3.7 \| T/Bl: 0.5–0.6 - 0.6 (1 h - 3 h - 6 h) | Zhang, et al. [92] |
| Iodine-124 | [$^{124}$I]I -Au@AuCBs-PEG | 87.1 | PEG | Covalent and encapsulation | 4 T1, mouse breast cancer retro-orbital injection, 1.5 MBq | In vivo | Combining PET and CLI | % ID/g: 5.4 (1 h) - 3.4 (6 h) - 1.8 (24 h)<br>T/M: ≈4–5 (1 h - 24 h) | Lee, et al. [90] |
| | [$^{124}$I]I AuNPs-PEG | 83.8 | PEG | Covalent and encapsulated | Sentinel lymph nodes (SLNs), subcutaneous | In vivo | PET-CLI detection of sentinel lymph nodes | SLNs visible 1 h p.i., strongest signal observed 6 h p.i. Signal decreased, but still evident at 24 h p.i.<br>% ID/g: ≈30 (1 h) – ≈10 (24 h) | Lee, et al. [78] |
| Iodine-125 | [$^{125}$I]I-cRP-AuNPs | 31 | Cyclic RGD | Adsorption | U87MG, human glioblastoma (pos)<br>MCF-7, human breast cancer (neg)<br>IV, 11 MBq | In vivo | targeted SPECT-CT | [$^{125}$I]I-cRP-AuNPs were localized inside αvβ3-positive U87MG cells, and were found in a negligible amount inside αvβ3-negative MCF7 cells. [$^{125}$I]I-cRP-AuNPs targeted the tumor site effectively (10 min) ~~1 % ID/g (1 h). After blocking: tumor was almost undetectable. | Kim, et al. [91] |
| | [$^{125}$I]I-AuNPs-Pt-RGD (T)<br>[$^{125}$I]I-AuNPs-Pt-RAD (UT)<br>[$^{125}$I]I-AuNRs-Pt-RGD (T)<br>[$^{125}$I]I-AuNRs-Pt-RAD (UT) | 56.4<br>56.1 × 22.4 | RGD (T)<br>RAD (UT) | Covalent | H1299, human lung cancer, IV, 11.1 MBq, 200 μl | In vivo | Targeted SPECT-CT of biodistribution and tumor uptake | Noticeable tumor uptake after 1 h. Maximal tumor uptake after 6 h. Significantly inhibited uptake after blocking with free RGD. UT probed only a low tumoral uptake.<br>% ID/g (AuNR-T 6 h): 6.93 ($T_{1/2}$: 227 min)<br>% ID/g (AuNP-T 6 h): 5.33 ($T_{1/2}$: 80 min)<br>% ID/g (AuNR-UT 6 h): 2.67 ($T_{1/2}$: 213 min)<br>% ID/G (AuNP-UT 6 h): 2.5 ($T_{1/2}$: 95 min) | Zhang, et al. [99] |
| Iodine-125<br>Indium-111 | dual-radiolabeled AuNPs | 10 | PEG<br>pMMP9 | Covalent<br>Chelation | A431 (high), human epidermoid carcinoma<br>4T1Luc (low), mouse breast cancer<br>IV<br>33.3 MBq indium-111<br>22.2 MBq iodine-125 | In vivo | Characterize MMP activity, biodistribution and tumor uptake using SPECT-CT | $^{125}$I signal was isolated to the thyroid, stomach, and bladder (4 h)<br>$^{111}$In chelation by DTPA stable in vivo (4 h)<br>% ID/g (A431): 7.25 (24 h) – 6.23 (48 h)<br>% ID/g (4T1Luc): 6.41 (24 h) – 10.2 (48 h)<br>T/M (both tumors):~8 (48 h) | Black, et al. [82] |
| Indium-111 | [$^{111}$In] In-AuNP-Trastuzumab | 54.2<br>42.1 | Trastuzumab (T)<br>Untargeted | Chelation | MDA-MB-361, human breast cancer<br>IT and IV<br>10–12 MBq | In vivo | SPECT-CT to track the in vivo fate of Trastuzumab-AuNP-$^{111}$In after IV and IT injection. | % ID/g (T-IV): 1.23 (48 h)<br>% ID/g (T-IT): 29.59 (48 h)<br>% ID/g (UT-IV): 2.20 (48 h)<br>% ID/g (UT-IT): 23.58 (48 h) | Chattopadhyay, et al. [110] |
| | RGD-modified $^{111}$In- labeled gold nanoparticles | 7 | RGD (T)<br>Untargeted (UT) | Incorporation | M21 (high), human melanoma<br>M21-L (low)<br>U87MG (high), human glioblastoma<br>IV, 1 MBq | In vivo | Targeted SPECT-CT to evaluate the imaging platform based on AuNPs | Uptake % ID/g (M21): 0.52<br>Uptake % ID/g (M21-L): 0.39<br>Uptake % ID/g (U87): 0.93 (T) – 0.37 (UT) | Ng, et al. [143] |
| | [$^{111}$In]In-EGF-Au-PEG | 32.5 | EGF | Chelation | MDA-MB-468 (pos), human breast cancer | In vivo | SPECT to evaluate tumor uptake of [$^{111}$In] In-EGF-Au-PEG in | Internalization: 11–15% in MDA-MB-468 cells, <2% in 231-H2N cells (4 h).<br>% ID/g (pos): 2.81 \| % ID/g (co-EGF): 3.91 (72 h) | Song, et al. [118] |

(continued on next page)

**Table 2** *(continued)*

| Isotope | Particle | Size (nm) | Functionalization | Labeling method | Cell model, administration | In vitro/in vivo | Application | Effect | Reference |
|---|---|---|---|---|---|---|---|---|---|
| | | | | | 231-H2N (neg), human breast cancer IV, 8 MBq | | co-administration of EGF | % ID/g (neg): 1.43 \| % ID/g (co-EGF): 1.29 (72 h) | |
| | [$^{111}$In]In-Au@HSANP | 213 | Albumin | Chelation | CT-26, mouse colon carcinoma IV, IP, 1.7 MBq | In vivo | SPECT to investigate the biodistribution and tumor uptake. | % ID/g (IV): 0.29–0.33 - 0.19 - 0.21 \| T/M: 9.5–11.1 - 9.3 - 7 (1 h - 24 h - 48 h - 96 h)<br>% ID/g (IP): 7.77–8.89 - 3.40 - 1.45 \| T/M: 89.4–217.4 - 128.8 - 28.3 (1 h - 24 h - 48 h - 96 h) | Chen, et al. [57] |
| Technetium-99m | [$^{99m}$Tc]Tc-AuNP-RGD | 21.7 | Cyclic RGD | Chelation | C6, rat glioma IV and IP, 3.7 MBq, 50 μl | In vivo | $R_v\beta_3$ expression imaging using targeted SPECT-CT | % ID/g (IV): 3.48–3.65 - 2.49 - 1.94 (0.5 h - 1 h - 3 h - 24 h); blocked: 1.46 (1 h)<br>% ID/g (IP): 2.09–3.28 - 8.18 - 3.20 (0.5 h - 1 h - 3 h - 24 h); blocked: 1.18 (1 h)<br>T/Bl (IV): 7.4 \| T/M: 10.0 \| T/Li: 0.2 \| T/S: 0.7 (1 h)<br>T/Bl (IP): 20.5 \|T/M: 27.3 \| T/Li: 2.1 \| T/S: 3.4 (1 h)<br>Tumor uptake is higher than that of UT form or [$^{99m}$Tc]Tc-RGD (1 h, IV) | Morales-Avila, et al. [51] |
| | [$^{99m}$Tc]Tc-AuNP-mannose | 23.3<br>20 | Mannose (T)<br>Untargeted (UT) | Chelation | Sentinel lymph nodes Subcutaneous, 1.85 MBq | In vivo | Sentinel lymph node detection using targeted SPECT-CT | % ID (T): 12.99 (1 h) and 21.02 (24 h)<br>% ID (UT): 5.41 (1 h) and 13.85 (24 h) | Ocampo-Garcia, et al. [52] |
| | [$^{99m}$Tc]Tc-AuNP-RGD | 22 | cRGD | Chelation | 4 T1-luc, mouse breast cancer IV, 1.85 MBq, 200 μl | In vivo | Targeted SPECT-CT to evaluate micrometastasis | % ID lung metastasis (1 h): 14.<br>[$^{99m}$Tc]Tc-AuNP-RGD achieved a 5.2× higher signal in lung metastases than the [$^{99m}$Tc]Tc-RGD (1 h). | Peiris, et al. [102] |
| | Gd/[$^{99m}$Tc]Tc-AuNPs-RGD | 29<br>51<br>80 | cRGD<br>Untargeted | Chelation | H1299, human non-small cell lung carcinoma IV, 7.4 MBq, 100 μl | In vivo | Combining MRI and SPECT-CT for image-guided radiosensitization | MRI rSIE (29): (T) 2.4 - (UT) 1.5 - (block) 1.5 (4 h)<br>MRI rSIE (51): (T) 1.6 - (UT) 1.3 - (block) 1.4 (4 h)<br>MRI rSIE (80): (T) 1.5 - (UT) 1.3 - (block) 1.4 (4 h)<br>% ID/g (29): (T) 14.6 – (UT) 4.0 – (Block) 6.2 (6 h)<br>% ID/g (51): (T) 9.4 – (UT) 4.4 – (block) 5.1 (6 h)<br>% ID/g (80): (T) 8.4 – (UT) 3.3 – (block) 4.9 (6 h) | Yang, et al. [66] |
| | {$(Au_0)_6$-G2-[$^{99m}$Tc]Tc-NOTA-PEG-RGD}-DENPs | 1.9 | RGD (T)<br>Untargeted (UT) | Chelation | C6, rat glioma IV, 21 MBq, 150 μl | In vivo | targeted SPECT/CT to evaluate $\alpha_v\beta_3$ integrin expressing tumors | T treatment: Increased signal SPECT (24×) and CT (>2×) intensities 30 min after injection compared to UT treatment. | Xu, et al. [65] |
| | {$(Au_0)_6$-G2-[$^{99m}$Tc]Tc-DTPA-PEG-FA} DENPs | 1.3–1.6 | Folic acid (T)<br>Untargeted (UT) | Chelation | HeLa, human cervical cancer IV, 37 MBq, 100 μl | In vivo | SPECT-CT imaging, in vivo | T treatment: CT intensity 1.3× higher than after UT treatment<br>SPECT intensity 2× higher than after UT treatment, 90 min after injection | Li, et al. [144] |
| | [$^{99m}$Tc]Tc — APAS-Au-PENPs | 3.3 | pH responsive APAS (T)<br>Untargeted (UT) | Chelation | HT1080, human fibrosarcoma | In vitro | SPECT-CT imaging of cancer cells in vitro | Increased acidity (pH 6.5–5.5), sharply increases the cellular uptake and the CT and SPECT intensities of the T form compared to UT form. | Zhu, et al. [145] |
| | [$^{99m}$Tc]Tc-Au-Ac-PENPs<br>$^{99m}$Tc-Au-Gly-PENPs | 3.3 | Acetylated or hydroxylated surface | Chelation | Sentinel lymph node (SLNs), subcutaneous 185 MBq, 0.5 ml | In vivo | Sentinel lymph node (SLNs) detection by SPECT-CT | The SLNs can be detected in CT-SPECT imaging at 0.5 h p.i. The accumulation becomes brighter with time. At 4 h p.i. the SLNs show accurate delineation. HU values: 6 (1 h) – 101 (4 h). | Zhao, et al. [63] and Wen, et al. [146] |
| | [$^{99m}$Tc]Tc-RGD-AuNPs-PENPs | 2.6<br>2.2 | RGD (UT)<br>Untargeted (UT) | Chelation | Orthotopic HCC-LM3, human hepatocellular carcinoma IV, 22.2 MBq, 150 μl | In vivo | SPECT-CT imaging of $\alpha v\beta 3$ integrin-overexpressing tumors | SPECT-CT signal intensities are much higher in the normal liver than in the cancer tissue.<br>HU (T): 47.1 – SPECT: 1.86 Mbq/mm$^3$ (0.5 h)<br>HU (UT): 32.6 – SPECT: 1.65 MBq/mm$^3$ (0.5 h) | Zhou, et al. [147] |
| | [$^{99m}$Tc]Tc-AuNP-Lys3-bombesin | 20.6 | Bombesin (T) | Chelation | PC-3, human prostate cancer IV, 1.85 MBq, 50 μl | In vivo | SPECT-CT for in vivo GRP-receptor imaging | % ID/g (T): 4.30–6.39–0.44 (0.5 h - 1 h - 24 h)<br>T/Bl (T): 5.8 (1 h) – Pacreas/Bl: 36<br>T/Bl (Monomer): 3.75 – Pancreas/Bl: 16 | Mendoza-Sanchez, et al. [104] |
| | [$^{99m}$Tc]Tc-duramycin-Au DENPs | 5.9<br>2.2 | Duramycin (T)<br>Untargeted (UT) | Chelation | C6, rat glioma IV, 74 MBq, 100 μl | In vivo | SPECT-CT to evaluate apoptosis in tumors induced by chemotherapy | T treatment: increased SPECT (>3×) and CT (1.56×) signal intensities 2 h–12 h p.i. compared to UT.<br>UT treatment: no signal intensity changes. | Xing, et al. [62] |
| Gold-199 | [$^{199}$Au]AuNPs | 5 (S) | D-Ala1-peptide | Incorporation | 4 T1, mouse | In vivo | SPECT imaging | T (S): % ID/g: 7.13 - T/M: 18.7 (24 h) | Zhao, et al. [70] |

| | | | | | | | | | |
|---|---|---|---|---|---|---|---|---|---|
| | | 18 (L) | T-amide (DAPTA) (T) Untargeted (UT) | | breast cancer IV, 185 kBq (biodistribution) 29.6 MBq (SPECT) | | | UT (S): % ID/g: 3.45 - T/M: 10.1 (24 h) UT (L): % ID/g:~3 - T/M: 11.9 (24 h) heterogeneous intratumoral distribution | |
| Copper-64 | [$^{64}$Cu] Cu-AuNCs—AMD3100 | 4.5 | AMD3100 (T) Untargeted (UT) | Incorporation | Orthotopic 4 T1, mouse breast cancer IV, 3.7 MBq, 100 μl | In vivo | PET imaging of orthotopic lung tumor and metastasis | Primary tumor (1 week post implantation): % ID (monomer): 2.13 – T/M: 3.55 (24 h) % ID (T): 7.15 – T/M: 18.9 (24 h) % ID (UT): 3.08 – T/M: 3.79 (24 h) Metastasis (4 weeks post implantation): % ID (monomer): 0.65 (24 h) % ID (T): 7.36 - L/M: 24.1 (24 h) % ID (UT): 0.79 (24 h) | Zhao, et al. [68] |
| | [$^{64}$Cu]Cu-cRGD-DOX-AuNPs | 10 × 45 | cRGD (T) Untargeted (UT) | Chelation | U87MG, human glioblastoma IV, 5–10 MBq | In vivo | PET imaging of biodistribution and tumor-targeting efficacy | % ID (T): 6.4–4.6 - 3.3 - 2.2 (1 h - 5 h - 24 h - 48 h) % ID (UT): 6.4–5.3 - 3.1 - 1.8 (1 h - 5 h - 24 h - 48 h) T/M (T): 16.6 (5 h) – 3.6 (48 h) | Xiao, et al. [148] |
| | [$^{64}$Cu]Cu-AuNS | 140 | PEG | Chelation | SCC-4, human head and neck squamous cell carcinoma IV, 17–18 MBq, | In vivo | PET/CT imaging of biodistribution and tumor accumulation for future image-guided PTT. | Tumor uptake was not significant after 1 h, but increased over time and plateaued after 20 h. The majority of accumulated particles still at the tumor site after 44 h. % ID/g [$^{64}$Cu]Cu-AuNS: 0.77 (46 h) % ID/g [$^{64}$Cu]Cu-DOTA(-PEG): 0.1–0.15 (46 h) | Xie, et al. [103] |
| | [$^{64}$Cu]Cu-AuNS-RGDfK | 140 | RGDfK (T) PEG (UT) | Chelation | SCC-4, human head and neck squamous cell carcinoma and IV, 22.2–29.6 MBq | In vivo | PET/CT imaging of tumor accumulation in SCC-4 for image-guided PTT in HCT116 colorectal cancer | No obvious accumulation at 1 h p.i. [$^{64}$Cu]Cu-AuNS-RGDfK accumulated in the tumor at 4 h p.i. Maximal accumulation at 20 h p.i. Gradual decline at 44 h p.i. UT AuNS accumulation less pronounced during each time point. | Xie, et al. [142] |
| | [$^{64}$Cu] Cu-DOTA-PEG-AuNCages | 55 (L) 30 (S) | PEG | Chelation | EMT-6, mouse breast cancer IV, 3.7 MBq, 100 μl | In vivo | PET-CT imaging: biodistribution and EPR tumor targeting of two differently sized AuNCs | % ID/g (L): <2 (1 h–24 h) T/M (L): 4.13–11.9 - 12.8 (1 h–4 h-24 h) T/Bl (L): 0.30–1.20 (1 h–24 h) % ID/g (S): 2.68–7.2 - 7.9 (1 h–4 h-24 h) T/M (S): 25.7 (24 h) T/Bl (S): 0.14–5.15 (1 h–24 h) | Wang, et al. [59] |
| | Pd[$^{64}$*Cu*] Cu@AuTripods-PEG-DAPTA | 24.8 × 5.8 | D-Ala1-peptide T-amide (DAPTA) (T) mPEG (UT) | incorporation | Orthotopic mouse 4 T1 breast cancer, IV, 3.7 MBq, 100 μl | In vivo | PET/CT of biodistribution and tumor uptake for image-guided PTT | % ID/g (T): 5.19–11.2 (4 h–24 h) % ID/g (UT): 4.64–6.83 (4 h - 24 h) SUV PET (T): 2.18 (24 h) SUV PET (UT): 1.47 (24 h) SUV PET (T-blocked): 1.59 (24 h) T/M (T): 28.6 (24 h); 32.7 (SUV PET) T/M (UT): 5.28 (24 h); 4.84 (SUV PET) T/M (T-blocked): 7.89 (SUV PET) (24 h) T/Bl (T): 5.70 (24 h) T/Bl (UT): 1.82 (24 h) | Pang, et al. [122] |
| | [$^{64}$Cu] Cu-AuNCages-PEG-MSH | 35 | MSH (1800 copies/AuNC) (T) MSH (5400 copies/AuNC) (T +) PEG (UT) | Chelation | B16/F10, mouse melanoma IV, 3.7 MBq, 100 μl | In vivo | PET/CT of biodistribution and tumor uptake | % ID/g (T): 4.57 (24 h) % ID/g (T blocked): 3.59 (24 h) % ID/g (T+): 7.43–7.54 (24 h–48 h) % ID/g (T+ blocked): 4.58 (24 h) % ID/g (UT): 3.40 (24 h) T/M (T): 20.26 (24 h) T/M (T+): 19.67–30.48 (24 h–48 h) T/M (UT): 10.11 (24 h) | Zhao, et al. [149] |
| | [$^{64}$Cu]Cu-AuNS | 170 | PEG | Chelation | SCC-4, human head and neck squamous cell carcinoma IV, 10.8–14.2 MBq IT, 17–18 MBq | In vivo | PET-CT to assess biodistribution for future PTT | IT: high tumor concentrations up to 44 h % ID/g: 6.28 (46 h) IV: much lower amount of AuNS in tumor, slow increase over time % ID/g: 0.77 (46 h) | Xie, et al. [111] |
| | [$^{64}$Cu]Cu-RGD-PEG-HAuNS | 44.7 | Cyclic RGD (T) iodized oil Untargeted (UT) | Chelation | VX2, rabbit squamous cell carcinoma IV, 25 MBq, 1 ml IA, 23 MBq, | In vivo | PET-CT to compare tumor uptake of HAuNS after IV and IA administration | % ID/g (IV-T): 0.16–0.15 (1 h–24 h) \| T/Li: 0.79 - T/M: 13.54 (1 h) % ID/g (IV-UT): 0.22–0.13 (1 h–24 h) \| T/Li: 1.11 - T/M: 17.37 (1 h) % ID/g (IA-T): 0.20 (1 h–24 h) \| T/Li: 0.81 - T/M: 12.74 (1 h) % ID/g (IA-UT): 0.13–0.10 (1 h–24 h) \| T/Li: 0.81 - T/M: 14.16 (1 h) % ID/g (IA-UT + oil): 0.51–0.33 (1 h–24 h) \| T/Li: 4.17 - T/M: | Tian, et al. [126] |

(continued on next page)

**Table 2** *(continued)*

| Isotope | Particle | Size (nm) | Functionalization | Labeling method | Cell model, administration | In vitro/in vivo | Application | Effect | Reference |
|---|---|---|---|---|---|---|---|---|---|
| | [$^{64}$Cu] Cu-NOTA-Au-IONP-Affibody | 24.4 | Anti-EGFR affibody | Chelation | 1.4 ml A431, human epidermoid carcinoma IV, 3.7 MBq, 150 μl | In vivo | Targeted PET and MRI imaging | 48.01 (1 h) % ID/g: 3.5 (4 h) - 4.6 (24 h) \| T/M: 6 (4-48 h) % ID/g (blocked): 1.9 (24 h) \| T/M: 2 (4-48 h) 44% decrease in MRI signal intensity 48 h after injection of T. No decrease in MRI signal intensity after blocking. | Yang, et al. [132] |
| | [$^{64}$Cu]Cu-AuNCs | 4.3 6.9 | PEG 350 Da PEG 1000 Da | Incorporation | PC-3, human prostate cancer IV, 3.7 MBq, 100 μl | In vivo | PET imaging | % ID/g: ~0.8 (1 h) - ~ 3 (24 h) for both T/M: ~0.5 (1 h) – ~2.5 (24 h) for both heterogeneous distribution of radioactivity across the tumor mass | Zhao, et al. [75] |
| | [$^{64}$Cu]Cu-AuNPs | 27 | PEG | Incorporation | EMT6, mouse breast cancer IV, 3.7 MBq, 100 μl | In vivo | Improving PET-CT accuracy and radiolabeling stability | Stable in mouse serum without degradation up to 48 h% ID/g: 4.93 (1 h) – 16.8 (48 h) T/M: 3.99 (1 h) – 11.9 (24 h) - 16.2 (48 h) | Zhao, et al. [71] |
| | [$^{64}$Cu]Cu-AuNR-RGD | 25 × 8 | RGD (T) Untargeted (UT) | Incorporation | U87MG, human glioblastoma IV, 5.55 MBq | In vivo | Targeted PET-CT for future image-guided PTT | % ID/g (T): 5–8 - 8.37 - 7.6 (4 h - 16 h - 24 h - 45 h) % ID/g (blocked): 6.17 (24 h) % ID/g (UT): 6.19 (24 h) | Sun, et al. [72] |
| | [$^{64}$Cu]Cu-AuNPs | 25 73 40 | NDM/Tw20 PEG S/QA | Incorporation | FaDu, human squamous cell carcinoma IV, 1.24–2.28 MBq | In vivo | PET-CT to investigate biodistribution of AuNPs | % ID/g (NDM/Tw20): 1.29 (24 h) % ID/g (PEG): 3.89 (24 h) % ID/g (S/QA): negligible | Frellsen, et al. [69] |
| | [$^{64}$Cu]Cu-PEG-HAuNS-DOX | 42.5 | DOX | Chelation | VX2, rabbit squamous cell carcinoma Embolization (E) | In vivo | PET-CT to visualize NP uptake in tumors after ablation | SUV tumor (E): 13.9–14.1 (1 h–18 h) \| T/Li: 1.1–1.7 (1 h–18 h) SUV tumor (E + RFA): 21.5–13.6 (1 h–18 h) \| T/Li: 4.7–1.4 (1 h–18 h) SUV tumor (E + IRE): 12.6–12.3 (1 h–18 h) \| T/Li: 0.81–2 (1 h–18 h) SUV tumor (E + LITT): 4.8–17.9 (1 h–18 h) \| T/Li: 2–1.5 (1 h–18 h) | Tam, et al. [58] |
| Zirconium-89 | [$^{89}$Zr] Zr-anti-CD105-AuNPs-PPAA | 103 4.8 | Anti-endoglin Ab (CD105) (T) Untargeted (UT) | Chelation | B16F10-luc, mouse skin melanoma IV, 2.9–4.1 MBq | In vivo | PET-CT to evaluate the impact of AuNP conjugation on the targeting of CD105 | % ID/ml (T): 4.6 (24 h) % ID/ml (blocked): 1.9 (6 h) % ID/ml (CD105-$^{89}$Zr): 6.5 (24 h) T/B: >4 (24 h) | Karmani, et al. [150] |
| | [$^{89}$Zr] Zr-Cetuximab-PPAA-AuNPs | 31 4.8 | Cetuximab (Ctxb) | Chelation | A431, human epidermoid carcinoma IV, 2.2–4.6 MBq | In vivo | PET to evaluate the impact of AuNP conjugation on the targeting of Ctxb | % ID/ml (T): 3.3 (48 h) % ID/ml (Blocked): 1.5 (48 h) % ID/ml (Ctxb-$^{89}$Zr): 3.9 (48 h) T/B (T): 12 (48 h), >20 (168 h) T/B (blocked): 3.4 (48 h) T/B (Ctxb-$^{89}$Zr): < 10 (48 h), <20 (168 h) | Karmani, et al. [106] |

**Abbreviations:** Ac: acetylated; Au@AuCB: crushed gold shell gold core nanoballs; AuNC: gold nanocluster; AuNP: gold nanoparticle; AuNR: gold nanorod; Au-PENPs: polyethylenimine-entrapped gold nanoparticles; APAS: alkoxyphenyl acylsulfonamide; cRP: cRGD-PEG; CLI: Cerenkov luminescent imaging; CT: computed tomography; DAPTA: D-Ala1-peptide T-amide; Au-DENPs: dendrimer-entrapped gold nanoparticles; DOX: doxorubicin; DOTA: 1,4,7,10-tetraazacyclododecane-1,4,7,10-tetraacetic acid; DTPA: diethylenetriaminepentaacetic acid; DTX: docetaxel; E: embolization; EGF: epidermal growth factor; EGFR: epidermal growth factor receptor; gly: glycol monomethyl; FA: folic acid; HAuNS: hollow gold nanoshells; Au@HSANP: gold nanocore-encapsulated human serum albumin nanoparticle; HU: Hounsfield unit; IA: intra-arterial; IONP: iron oxide nanoparticle; IP: intraperitoneal; IRE: irreversible electroporation; IT: intratumoral; IV: intravenous; L: large; LITT: laser induced thermal therapy; L/M: lung-to-muscle ratio; MRI: magnetic resonance imaging; NDM/Tw20: 1-dodecanethiol/tween 20; NOTA: 2-S-(4-isothiocyanatobenzyl)-1, 4, 7-triazacyclononane-1, 4, 7-triacetic acid; AuNS: gold nanoshells; PEG: polyethylene glycol; PET: positron emission tomography; p.i.: post-injection; PTT: photo-thermal therapy; pMMP9: matrix metalloproteinase-9 cleavable peptide; MSH: α-melanocyte-stimulating hormone; PPAA: plasma-polymerized allylamine; RFA: radiofrequency ablation; rSIE: relative signal intensity enhancement; S: small; SLN: sentinel lymph node; SPECT: single photon emission computed tomography; SUV: standardized uptake value; S/QA: sulphonate/quaternary ammonium; T: targeted; T/B: tumor-to-background ratio; T/Bl: tumor-to-blood ratio; TIONts: titanate nanotubes; T/L: tumor-to-lung ratio; T/Li: tumor-to-liver ratio; T/M: tumor-to-muscle ratio; T/S: tumor-to-spleen ratio; TRT: targeted radionuclide therapy; UT: untargeted; % ID: percentage of injected dose.

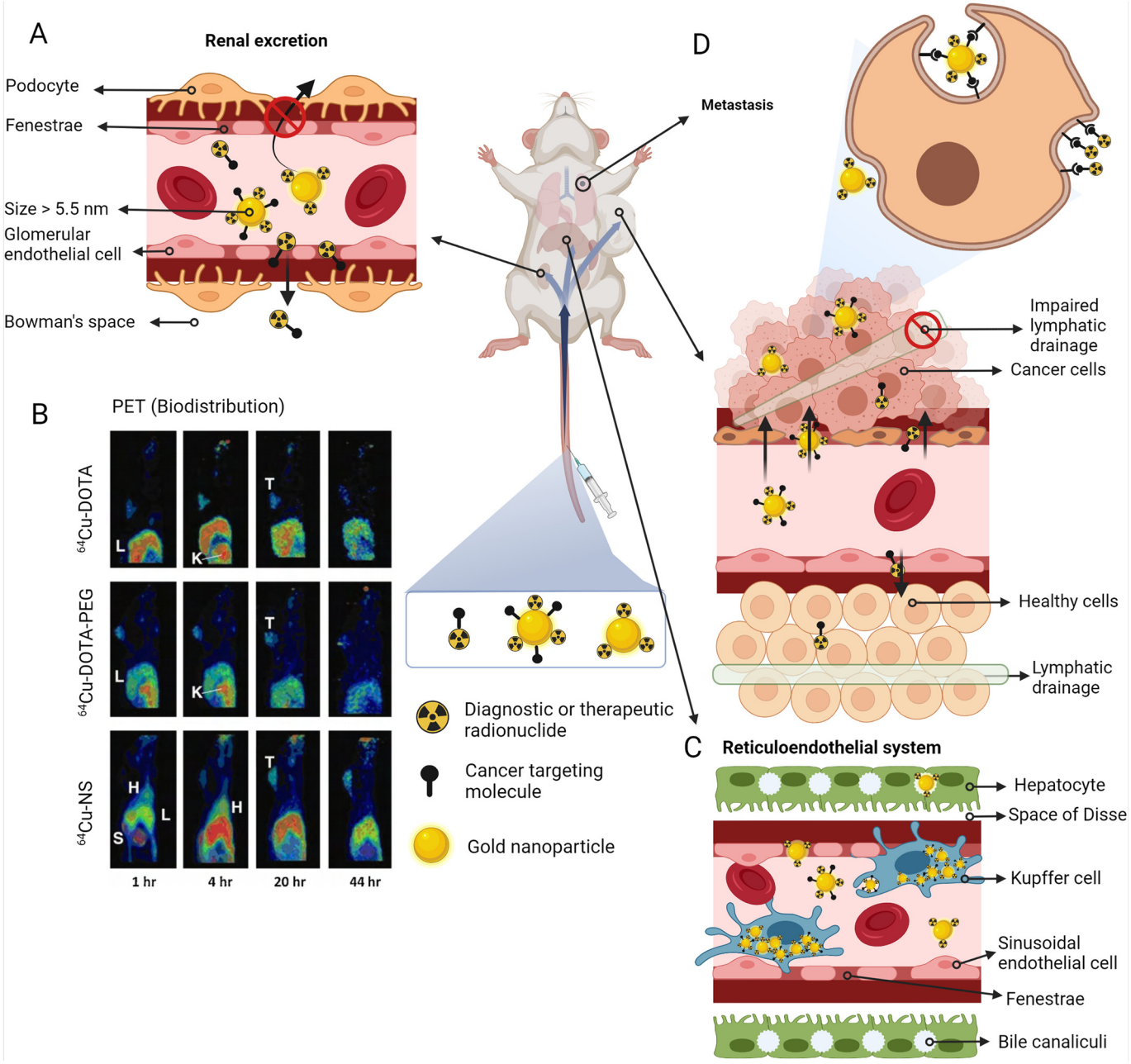


**Fig. 7.** Biodistribution and tumor uptake of radiolabeled targeted AuNPs, radiolabeled untargeted AuNPs or small radiolabeled monomers after IV administration. (A) After IV administration, small radiolabeled monomers demonstrate a short blood circulation half-life and are rapidly excreted via glomerular filtration. This is in contrast to AuNPs larger than 5.5 nm, which are unable to pass through the glomerular filtration barrier. (B) Sagittal PET images of three rats acquired at various time points after IV injection of [$^{64}$Cu]Cu-DOTA, [$^{64}$Cu]Cu-DOTA-PEG2K or [$^{64}$Cu]Cu-AuNS. (H, Heart; L, Liver; S, Spleen; K, Kidneys; T, Tumor). Color intensity scale is denoted as red > yellow > green > blue. The PET images show a rapid kidney uptake and a weaker tumor accumulation of the monomeric [$^{64}$Cu]Cu-DOTA and [$^{64}$Cu]Cu-DOTA-PEG2K compared to [$^{64}$Cu]Cu-AuNS, which demonstrate an increased tumor accumulation 4 h post-injection and a tumor retention longer than 44 h. Reprinted from [103][1]. (C) A major part of the targeted and untargeted radiolabeled AuNPs are typically sequestrated by Kupffer cells in the liver, being part of the reticuloendothelial system (RES) and which can delay or inhibit the hepatobiliary excretion of the AuNPs. (D) Radiolabeled AuNPs can accumulate in the tumor by the EPR effect and by active transendothelial transport pathways. There is a larger accumulation of targeted radiolabeled AuNPs in cancer cells compared to untargeted radiolabeled AuNPs and radiolabeled monomers, thanks to their multivalent binding to cancer-specific receptors, which improves cancer cell binding and uptake. (For interpretation of the references to colour in this figure legend, the reader is referred to the web version of this article.) [1]Fig. 7 B is reprinted from International Journal of Pharmaceutics, Volume 395, Issues 1–2, H. Xie, Z. J. Wang, A. Bao, B. Goins and W. T. Phillips, *In vivo* PET imaging and biodistribution of radiolabeled gold nanoshells in rats with tumor xenografts, Pages 324–30., Copyright (2010), with permission from Elsevier.

the phagocytic cells of the reticuloendothelial system (RES), which prevents their efficient hepatobiliary elimination [108] (Fig. 7 B–C). Intraperitoneal (IP) administration of [$^{99m}$Tc]Tc-AuNP-RGD, [$^{111}$In]In-AuNP@Albumin and [$^{67}$Ga]Ga-bombesin-AuNPs significantly reduces the nanoparticle sequestration by the RES, compared to IV administration [51,57,109]. Nevertheless, the glioma tumor uptake of [$^{99m}$Tc]Tc-AuNP-RGD is faster after IV injection (maximal after 1 h) than after IP administration (maximal after 3 h). Furthermore, the [$^{67}$Ga]Ga-bombesin-AuNPs prostate tumor uptake is higher after IV injection, than after IP injection [109]. Therefore, IV administration is probably more convenient for diagnostic purposes [51]. Alternatively, intratumoral (IT) injection delivers an immediate high concentration of radiolabeled AuNPs inside the tumor,

while the AuNP concentration in healthy tissues is lower than after an IV injection [110–114]. However, this administration method is not common for cancer detection.

Importantly, active targeting of AuNPs significantly improves the tumoral uptake compared to untargeted AuNPs (Fig. 7 D). However, certain targeting moieties can also increase the exposure of healthy tissues to the radiolabeled AuNPs. For example, a high accumulation of radiolabeled AuNPs is observed in the pancreas when the AuNPs are conjugated to the peptides bombesin or octreotide [104,107,109,115]. Bombesin and octreotide target the gastrin-releasing peptide receptor (GRP) and the somatostatin receptor, which are both highly expressed in the pancreas, but are also overexpressed on prostate cancer cells and neuroendocrine cancer cells, respectively. Orocio-Rodriguez, et al. demonstrated a higher uptake of [$^{99m}$Tc]Tc-AuNPs-Tyr3-octreotide in the pancreas compared to the monomeric [$^{99m}$Tc]Tc-Tyr3-octreotide [107]. Furthermore, the pancreas-to-blood ratio of [$^{99m}$Tc]Tc-AuNP-Lys3-bombesin was higher than that of monomeric [$^{99m}$Tc]Tc-Lys3-bombesin [104]. Both observations were explained by the faster renal

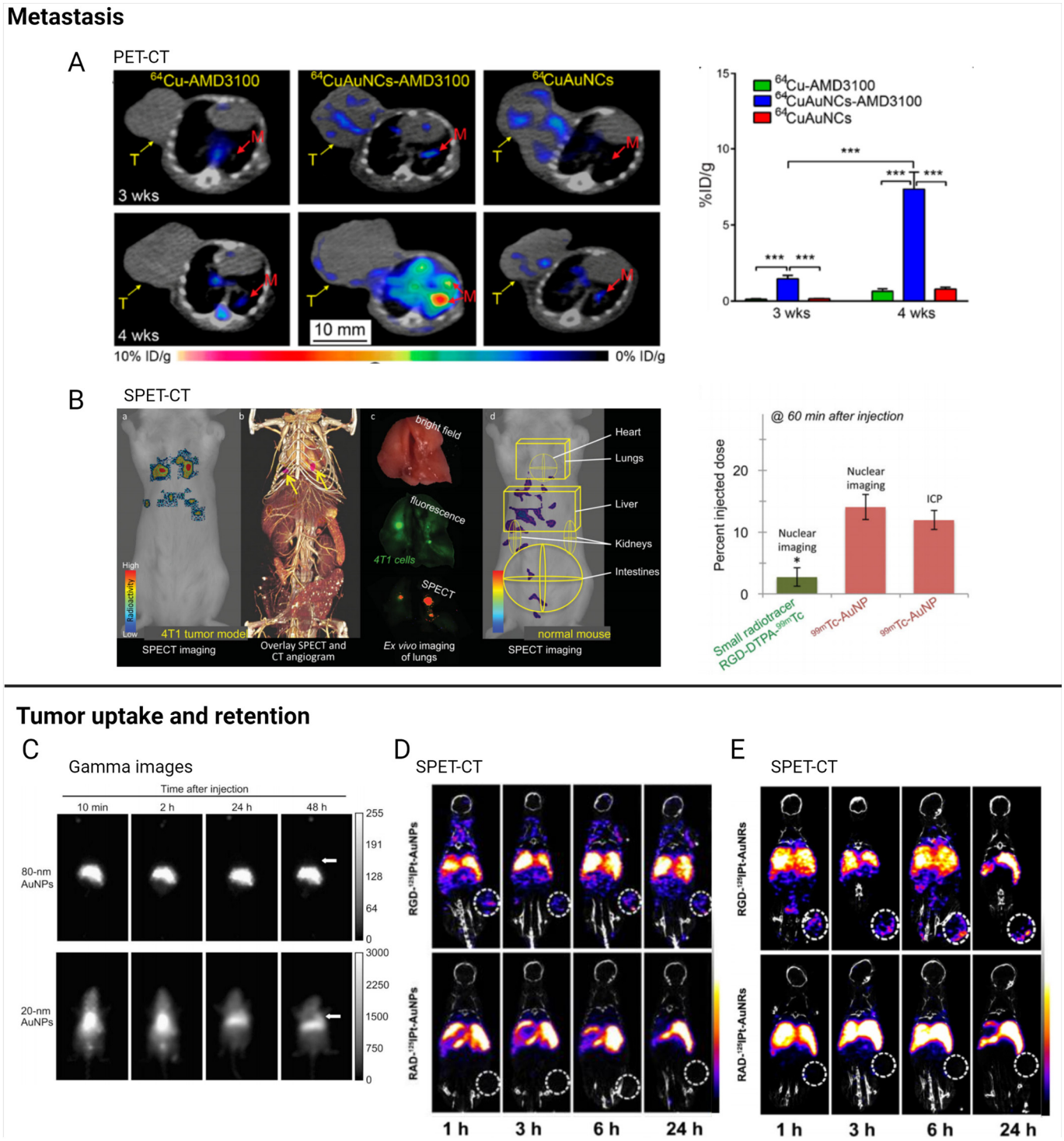

excretion of the monomeric carriers compared to the nanoconjugates. Another example is the higher liver and spleen uptake of AMD3100-conjugated [$^{64}$Cu]Cu-gold nanoclusters (AuNCs) compared to untargeted [$^{64}$Cu]Cu-AuNCs. AMD3100 is an antagonist of the chemokine receptor CXCR4, which is expressed on metastatic breast cancer cells. However, CXCR4 is also present on immune cells residing in the spleen and liver [68]. Similarly, conjugation of [$^{111}$In]In-AuNPs to Trastuzumab provokes a faster blood clearance and a higher uptake in the liver and spleen of the nanoparticles compared to untargeted [$^{111}$In]In-AuNPs, which is explained partly by the Fc-mediated recognition and uptake of the [$^{111}$In]In-AuNPs-Trastuzumab by the RES [110]. Despite the off-target uptake of these targeted, radiolabeled AuNPs, the studies did not assess the toxic effects in the healthy organs.

### 3.1.2. Enhanced tumor uptake and retention

Despite the higher RES sequestration after IV injection, the average tumor uptake of [$^{99m}$Tc]Tc-AuNPs-RGD (3.65% ID/g, glioma), [$^{99m}$Tc]Tc-AuNPs-Tyr$^3$-octreotide (≈3.4% ID/g, neuroendocrine tumor), [$^{64}$Cu]Cu-AuNCs-AMD3100 (7.15% ID/g, breast cancer), [$^{64}$Cu]Cu-AuNS (0.77% ID/g, squamous cell carcinoma) and [$^{99m}$Tc]Tc-resveratrol-AuNPs (colon cancer) is considerably higher than that of [$^{99m}$Tc]Tc-RGD (≈2.5% ID/g), [$^{99m}$Tc]Tc-Tyr$^3$-octreotide (≈2% ID/g), [$^{64}$Cu]Cu-AMD3100 (2.98%ID/g), [$^{64}$Cu]Cu-DOTA-PEG (0.09% ID/g) and [$^{99m}$Tc]Tc-Resveratrol without AuNPs, respectively [51,102,103,107,116] (Fig. 7 D). In addition, the early stage of 4T1 lung metastasis, which is currently difficult to detect, is successfully imaged by[$^{99m}$*Tc*]Tc-AuNPs-RGD (≈14% ID/g) and [$^{64}$Cu]Cu-AuNCs-AMD3100 (7.36% ID/g), whereas the small [$^{99m}$Tc]Tc-RGD and [$^{64}$Cu]Cu-AMD3100 radiotracers show a significantly lower uptake in these micro-metastatic lesions (≈2.7% ID/g and 0.65% ID/g, respectively) [68,102] (Fig. 8 A-B). Importantly, the extent of tumor uptake of radiolabeled AuNPs depends on the properties of the AuNPs, such as the size, the coating and the shape. In size-comparing studies, the smaller radiolabeled AuNPs, including 20 nm [$^{111}$In]In-PEG-AuNPs, 29 nm Gd/[$^{99m}$Tc]Tc-AuNPs-RGD and 30 nm [$^{64}$Cu]Cu-DOTA-PEG-AuNPs, consistently exhibit a longer blood circulation time, a higher tumor uptake and a lower RES sequestration compared to their larger counterparts (40 nm, 80 nm and 55 nm, respectively) (Fig. 8 C) [59,66,117]. Furthermore, a PEG coating on [$^{64}$Cu]Cu-AuNPs performs better in terms of a prolonged blood circulation, a delayed RES sequestration and an increased uptake in a squamous cell carcinoma compared to a zwitterionic coating or stabilization by Tween 20 [69]. The functionalization and the length of the PEG molecules have an influence on the stability and the *in vivo* behavior of the radiolabeled AuNPs. For instance, the immobilization of the PEG molecules on the AuNP surface via thioctic acid or lipoic acid providing two or more gold-sulfur bonds results in a higher stability and a longer blood circulation time of $^{177}$Lu-labeled AuNPs and $^{111}$In-labeled AuNPs compared to PEG immobilization via a single gold-sulfur bond [105,117]. In addition, longer PEG molecules (1000 and 5000 Da) prolongs the blood circulation time of PEG coated [$^{64}$Cu]Cu-AuNCs and [$^{111}$In]In-AuNPs, compared to 350 and 2000 Da PEG molecules, respectively [75,117]. However, increasing the length of the PEG molecules from 800 to 6000 Da also reduces the breast cancer cell uptake of the [$^{111}$In]In-EGF-AuNPs [118]. In addition, Zhang, et al. demonstrated that rod-shaped cisplatin (Pt)-loaded and $^{125}$I-labeled RGD-Pt-AuNRs exhibit a longer blood circulation time, a more efficient targeting of the lung tumor angiogenesis visualized by photoacoustic imaging and a higher tumor accumulation, compared to the spherical [$^{125}$I]I-AuNPs-Pt-RGD with a similar size (Fig. 8 D-E) [99]. A longer blood half-life might be attributed to a more efficient evasion of phagocytosis and clearance by macrophages. As a result, the [$^{125}$I]I-AuNRs-Pt-RGD have more chance to permeate into the tumor than the [$^{125}$I]I-AuNPs-Pt-RGD [99].

Next to an increased tumor uptake, AuNPs increase the tumor retention of the radionuclide. For instance, the residence time of [$^{177}$Lu]Lu-Tyr$^3$-octreotate-AuNPs in a 3D-multilayered culture of HeLa cells (17.10 h) is significantly higher than that of monomeric [$^{177}$Lu]Lu-Tyr$^3$-octreotate (5.13 h) [119]. Other studies confirmed the enhanced tumor retention of AuNP-based radiopharmaceuticals in *in vivo* tumor-bearing mice and rat models. In fact, [$^{177}$Lu]Lu-AuNPs-RGD show a rat glioma tumor residence time of 61.6 h after four IT injections, whereas [$^{177}$Lu]Lu-RGD remains in the tumor site for approximately 17.3 h [49] . In addition, the accumulation of [$^{64}$Cu]Cu-AuNS in the squamous cell carcinoma achieves a plateau 20 h after IV injection. At 44 h after IV injection, the majority of accumulated [$^{64}$Cu]Cu-AuNS are still present in the tumor, which is not the case for the monomeric [$^{64}$Cu]Cu-DOTA-PEG [103] (Fig. 7 B). Altogether, the enhanced tumor uptake and retention of targeted, radiolabeled AuNPs contribute to a high T/B ratio and are mainly attributed to the EPR effect, the multivalent targeting avidity and the high radionuclide cargo of the targeted, radiolabeled AuNPs, compared to the small monomeric radiotracers (Fig. 7 D) [51,68,102,103,119].

### 3.1.3. Intratumoral distribution

Once within the tumor matrix, the most beneficial scenario is that the radiolabeled AuNPs diffuse and spread uniformly throughout the tumor tissue [7]. Several studies assessed the local intratumoral distribution of the radiolabeled AuNPs using nuclear imaging, microscopic examination or autoradiography.In the majority of the studies, AuNPs are usually observed in the periphery of the tumor mass close to the vasculature where they generally display heterogeneous distribution [69,70,75,82,90,102,110,117,120–122]. The intratumoral diffusion of

**Fig. 8.** Radiolabeled AuNP uptake in tumors and metastatic lesions. (A) Quantitative uptake (in % ID/g) and PET/CT transverse images show the accumulation of [$^{64}$Cu]Cu-AMD3100, [$^{64}$Cu]Cu-AuNCs-AMD3100 and [$^{64}$Cu]Cu-AuNCs in the metastatic lesions of the lung of 4T1 tumor bearing mice at 3 weeks and 4 weeks post tumor implant. Images were acquired 24 h after IV administration. $^{*}$ $p < 0.05$, $^{**}$ $p < 0.005$, $^{***}$ $p < 0.001$. T: tumor. M: metastasis. Adapted from [68][2]. (B) First, coronal planar gamma scintigraphy image acquired 30 min after IV injection of $\alpha_v\beta_3$ integrin-targeting [$^{99m}$Tc]Tc-AuNPs detecting micrometastatic sites in the lungs of a mouse bearing 4 T1 breast cancer. Second, the gamma scintigraphy image was co-registered with a micromorphological angiogram image obtained by using a micro-CT and a liposome-based iodinated contrast agent (yellow arrows indicate the location of metastatic sites). Third, the lungs of the animals were imaged ex vivo using a SPECT system and a fluorescence imaging system, indicating the co-localization of the [$^{99m}$Tc]Tc-AuNPs and the 4T1 metastatic cells expressing GFP. Fourth, coronal planar gamma scintigraphy image showing a healthy mouse 30 min after IV injection of [$^{99m}$Tc]Tc-AuNPs, without tumor and metastatic lesions in the regions of interest. Graph: The PET signal of the [$^{99m}$Tc]Tc-AuNPs and the gold concentration in the 4T1 metastatic lesions shows a higher uptake of the [$^{99m}$Tc]Tc-AuNPs in the lesions compared to that of a small molecule analogue 60 min after injection. Reprinted from [102][3]. (C) Gamma images of the *in vivo* distribution of 80-nm and 20-nm $^{111}$In-labeled AuNPs in A431 tumor-bearing mice acquired 10 min, 2 h, 24 h, and 48 h after IV injection. Compared to 20-nm AuNPs, 80-nm AuNPs are cleared more rapidly from the blood and have higher concentrations in the liver and spleen. In contrast, 20-nm AuNPs have a longer blood pool activity and accumulate in the tumor 48 h after IV injection. Arrows indicate subcutaneous A431 tumors. Reprinted from [117][4]. (D-E) SPECT/CT imaging of H1299 tumor-bearing mice after IV administration of (D) [$^{125}$I]I-AuNPs-Pt-RGD or [$^{125}$I]I-AuNPs-Pt-RAD, or (E) [$^{125}$I]I-AuNRs-Pt-RGD or [$^{125}$I]I-AuNRs-Pt-RAD. Targeted [$^{125}$I]I-AuNPs-Pt-RGD and [$^{125}$I]I-AuNRs-Pt-RGD show a higher uptake compared to the untargered counterparts. In addition, [$^{125}$I]I-AuNRs-Pt-RGD show a higher tumor uptake compared to the [$^{125}$I]I-AuNPs-Pt-RGD. Adapted from [99][5]. (For interpretation of the references to colour in this figure legend, the reader is referred to the web version of this article.) [2]Fig. 8 A is adapted with permission from ACS Nano, Vol. 10 Issue 6, Y. Zhao, L. Detering, D. Sultan, M. L. Cooper, M. You, S. Cho, et al., Gold Nanoclusters Doped with (64)Cu for CXCR4 Positron Emission Tomography Imaging of Breast Cancer and Metastasis, Pages 5959–70, Copyright (2016) American Chemical Society. [3]Fig. 8 B is reprinted from Journal of Pharmaceutical Sciences, Vol. 104, Issue 8, P. M. Peiris, P. Deb, E. Doolittle, G. Doron, A. Goldberg, P. Govender, et al., Vascular Targeting of a Gold Nanoparticle to Breast Cancer Metastasis, Pages 2600–10, Copyright (2015), with permission from Elsevier. [4]Fig. 8 C is reprinted from Biomaterials, Vol. 30 Issue 10, G. Zhang, Z. Yang, W. Lu, R. Zhang, Q. Huang, M. Tian, et al., Influence of anchoring ligands and particle size on the colloidal stability and *in vivo* biodistribution of polyethylene glycol-coated gold nanoparticles in tumor-xenografted mice, Pages 1928–36, Copyright (2009), with permission from Elsevier. [5]Fig. 8 D and E are adapted from Zhang, L., Su, H., Wang, H., Li, Q., Li, X., Zhou, C., Xu, J., Chai, Y., Liang, X., Xiong, L. and Zhang, C, Tumor Chemo-Radiotherapy with Rod-Shaped and Spherical Gold Nano Probes: Shape and Active Targeting Both Matter, Theranostics, Vol. 9 Issue 7 Pages 1893–1908, https://www.thno.org/v09p1893.htm, Open access article distributed under the terms of the Creative Commons BY-NC 4.0 license (https://creativecommons.org/licenses/by-nc/4.0/). Copyright (2019) Ivyspring International Publisher. No changes were made to the images.

AuNPs depends on the characteristics of both the AuNPs (such as size, charge and shape) and the tumor tissue (such as the cellular density and the extracellular matrix stiffness) [123,124]. For instance, [$^{198}$Au]Au-nanospheres and [$^{198}$Au]Au-nanodisks were found in the periphery of a EMT-6 breast tumor, whereas [$^{198}$Au]Au-nanorods and [$^{198}$Au]Au-nanocages were detected throughout, including the central region of the tumor after IV injection [74]. Similarly, 30 nm [$^{64}$Cu]Cu-DOTA-PEG-gold nanocages (AuNCages) accumulated in the central region of the EMT-6 breast tumor 24 h after IV administration. The central tumor accumulation of the [$^{64}$Cu]Cu-DOTA-PEG-AuNCages is attributed to the small size and neutral charge of the AuNPs as well as to the low interstitial pressure and the uniform blood flow of the EMT-6 breast cancer model, as visualized by photoacoustic imaging [59,74]. In addition, rod-shaped [$^{125}$I]I-AuNRs-Pt-RGD penetrated much deeper into the lung tumor interstitium than spherical [$^{125}$I]I-AuNPs-Pt-RGD [99]. On the other hand, the heterogeneous distribution of Trastuzumab-targeted and Cetuximab-targeted [$^{111}$In]In-AuNPs in a breast tumor and a squamous cell carcinoma, respectively, is partly attributed to the

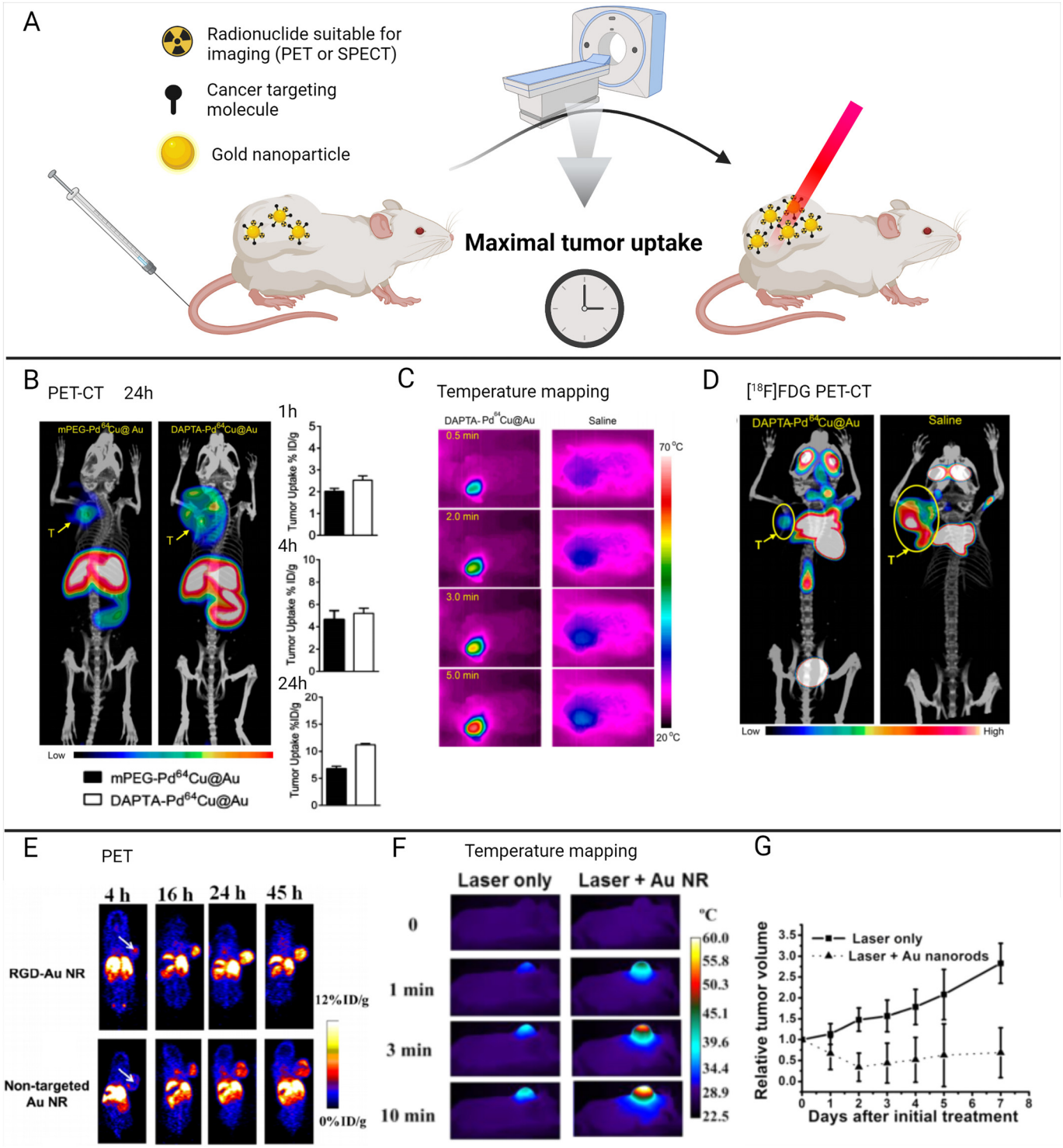

'binding-site barrier effect'. The binding-site barrier effect involves the strong binding of the antibodies to their target, which facilitates the extravasation of the AuNPs into the tumor, but also limits the intratumoral diffusion of the AuNPs [110,120,125]. Finally, in an advanced solid tumor with an aggressive tumor development, the presence of substantial necrotic foci limits the delivery of AuNPs or other anti-cancer pharmaceuticals [68]. Since [$^{177}$Lu]Lu-AuNP-RGD significantly decrease glioma progression and thus prevent the formation of necrotic foci, [$^{177}$Lu]Lu-AuNP-RGD display a more uniform intratumoral distribution as compared to [$^{177}$Lu]Lu-AuNPs or [$^{177}$Lu]Lu-RGD [49].

Intratumoral penetration of radiolabeled AuNPs can also be promoted by the application of external stimuli. For example, the uptake of [$^{64}$Cu]Cu-PEG-HAuNS-DOX in a squamous cell carcinoma in the liver is enhanced when injection into the hepatic artery (i.e. liver embolization) is followed by electroporation, radiofrequency ablation, or laser-induced thermal therapy. Electroporation causes cell membrane permeabilization via the use of electrical pulses, while radiofrequency ablation and laser-induced thermal therapy both generate heat via the delivery of an alternating electrical current and via laser irradiation, respectively. As a result, the [$^{64}$Cu]Cu-PEG-HAuNS-DOX are localized both in and around the tumor, whereas embolization alone results in a predominant peripheral tumor uptake [58]. Another strategy is the co-injection of an adjuvant such as lipiodol, which selectively enters liver tumors after liver embolization. It boosts the uptake of [$^{64}$Cu]Cu-PEG-HAuNS throughout the tumor achieving a high tumor-to-normal liver ratio of 4.17. Conversely, embolization of [$^{64}$Cu]Cu-PEG-HAuNS without lipiodol leads to a perivascular distribution and a lower tumor-to-normal liver ratio of 0.81 [126]. Similarly, IT co-injection of $^{103}$Pd/$^{198}$Au-dual radiolabeled AuNPs with the biocompatible polymer alginate sequestrates them in prostate tumor [127].

### 3.2. Imaging

An early diagnosis of cancer is often related to a better prognosis. Therefore, next to SPECT and PET imaging, the conventional, non-invasive imaging systems, such as CT and MRI are essential in the clinic. Gold nanoparticles have the potential to improve the contrast of CT images thanks to their high atomic number and high X-ray attenuation as described in Section 1.3.2.

Besides CT imaging [128], MRI is also a common clinical imaging modality offering anatomical information in high-spatial resolution, with a high contrast in soft tissue. MRI imaging is based on the relaxation of hydrogen protons and their electromagnetic energy emission after a radiofrequency pulse, under the influence of a strong external magnetic field. MRI contrast agents, $T_1$-positive or $T_2$-negative, affect the rate of the proton relaxation and enhance the sensitivity and quality of the images [129]. Thus, in order to exploit AuNPs as a contrast agent for MRI, they need to be complexed with MRI contrast materials. For instance, multicomponent nanoparticles have been produced by surrounding a magnetic core of iron oxide with a gold shell, or by coupling iron-oxide nanoparticles to AuNPs. Iron oxide is a superparamagnetic material exhibiting a strong magnetization under the influence of an external magnetic field, creating microscopic field heterogeneity. This accelerates the dephasing of the proton spins or the $T_2$ relaxation process. As a result, IV injection of these multicomponent NPs in tumor-bearing mice significantly decreases the signal intensity in the tumors using $T_2$-weighted MRI (Fig. 10 D) [17,130–132]. On the other hand, coupling AuNPs to paramagnetic metals, such as gadolinium or manganese, accelerates the $T_1$-relaxation process. As a result, administration of these nanomaterials increases the signal intensity in the murine tumors, creating bright $T_1$-weighted images (Fig. 10 A) [133–138].

Combination of multiple imaging modalities, such as PET or SPECT imaging with MRI or CT imaging improves the diagnostic accuracy by merging the high spatial resolution and precise anatomical detail provided by CT and MRI with the high sensitivity and the unique functional information of nuclear imaging [112,139–141]. Furthermore, multimodal nuclear imaging using radiolabeled AuNPs has also been used to perform image-guided, AuNPs-mediated PTT (Fig. 9 A-G) and enhanced external beam radiotherapy (EBRT) (Fig. 10 A-C) [66,72,122,142]. Table 2 provides an overview of the pre-clinical studies assessing the ability of radiolabeled AuNPs to improve or to combine multiple nuclear imaging modalities.

#### 3.2.1. Multimodal imaging

The radiolabeling of AuNPs enables the improvement of PET-CT and SPECT-CT. For instance, targeted dendrimer-entrapped AuNPs and polyethylenimine-entrapped AuNPs, radiolabeled with technetium-99m or with iodine-131, enhance the CT contrast on one hand and enable SPECT imaging on the other hand of sentinel lymph nodes as well as of glioma cells, fibrosarcoma cells, cervical cancer cells and hepatocellular carcinoma cellscells. The X-ray attenuation property of the AuNPs is exceeding that of Omnipaque, a clinically used iodine-based CT contrast agent [63,81,144–147,151]. Furthermore, the increase in SPECT(-CT) signal intensity is related to the concentration of gold and the radionuclide in the tumor cells. As a result, the SPECT(-CT) imaging contrast enhancement significantly improves when cancer targeting probes, such as chlorotoxin, chlorotoxin-like peptides, duramycin, cRGD, EGF, folic acid or pH-responsive moieties are linked to the nanocarriers as compared to the untargeted analogues, negative cancer cell models or blocked cancer cell receptors (Fig. 8 D-E and Fig. 10 B) [51,62,65,66,81,91,92,118,143–145,147,151,152]. Similarly, the PET(-CT) imaging signal after IV injection of targeted RGD-[$^{64}$Cu]Cu-AuNR, [$^{64}$Cu]Cu-AuNCs-AMD3100, Pd[$^{64}$*Cu*]Cu@AuTripods-PEG-DAPTA, [$^{64}$Cu]Cu-AuNS-RGDfK and [$^{64}$Cu]Cu-AuNCages-PEG-MSH in glioblastoma, breast cancer, squamous cell carcinoma and melanoma is higher than after IV injection of the untargeted [$^{64}$Cu]Cu-AuNR, [$^{64}$Cu]Cu-AuNCs, Pd[$^{64}$*Cu*]Cu@AuTripods-PEG, [$^{64}$Cu]Cu-AuNS and [$^{64}$Cu]Cu-AuNCages-PEG, respectively (Fig. 9 B; 9 E) [68,72,122,142,149]. Furthermore, PET imaging enables image-based photothermal therapy. Indeed, PET images showed a maximal uptake of RGD-[$^{64}$Cu]Cu-AuNR and Pd[$^{64}$*Cu*]Cu@AuTripods-PEG-DAPTA in a glioblastoma and breast tumor after 24 h, respectively, which was followed by photothermal therapy using 808 nm laser irradia-

**Fig. 9.** Image-guided therapy. (A) After IV injection of (targeted) radiolabeled AuNPs, nuclear imaging can be used to determine the maximal uptake of the AuNPs in the tumor site to start a treatment such as photothermal therapy. (B) PET/CT images acquired 24 h post-IV injection of CCR5-targeting, DAPTA-conjugated $^{64}$Cu-doped AuTripods (Pd[$^{64}$*Cu*]Cu@AuTripods-PEG-DAPTA) or untargeted Pd[$^{64}$*Cu*]Cu@AuTripods-PEG in 4T1 tumor-bearing mice. The quantitative tumor uptake at 1 h, 4 h and 24 h post-IV injection shows a maximal tumor uptake of Pd[$^{64}$*Cu*]Cu@AuTripods-PEG-DAPTA after 24 h, which is higher compared to the tumor uptake of Pd[$^{64}$*Cu*]Cu@AuTripods-PEG. T, tumor; L, liver. (C) Thermographs of tumor-bearing mice acquired 24 h post-IV injection of saline or Pd[$^{64}$*Cu*]Cu@AuTripods-PEG-DAPTA and after laser irradiation of the tumor for 0, 1, 3 or 10 min. The laser power density was 1.2 W/cm$^2$. (D) [$^{18}$F]FDG PET/CT images of mice IV injected with Pd[$^{64}$*Cu*]Cu@AuTripods-PEG-DAPTA or saline and acquired 24 h after photothermal therapy demonstrating a reduced tumor metabolic activity. B–D are adapted from [122]$^{6}$. (E) Coronal PET images of U87MG tumor-bearing mice aqcuired 4 h, 16 h, 24 h, and 45 h after IV injection of [$^{64}$Cu]Cu-AuNRs-RGD or untargeted [$^{64}$Cu]Cu-AuNRs, showing a maximal tumor uptake of the targeted AuNRs after 24 h, which is higher than the tumor uptake of the untargeted [$^{64}$Cu]Cu-AuNRs. Arrow = tumor area. (F) Temperature mapping of tumor-bearing mice upon laser irradiation (808 nm, 1 W cm$^{-2}$) for 1, 3, and 10 min, acquired 24 h after IV administration of [$^{64}$Cu]Cu-AuNRs-RGD or without [$^{64}$Cu]Cu-AuNRs-RGD. (G) Tumor growth curves of mice treated with or without [$^{64}$Cu]Cu-AuNRs-RGD and in combination with laser irradiation. *E*-G are adapted from [72]$^{7}$. $^{6}$Fig. 9 B-D are adapted with permission from ACS Nano, Vol. 10 Issue 3, B. Pang, Y. Zhao, H. Luehmann, X. Yang, L. Detering, M. You, et al. (6)(4)Cu-Doped PdCu@Au Tripods: A Multifunctional Nanomaterial for Positron Emission Tomography and Image-Guided Photothermal Cancer Treatment, Pages 3121–31, Copyright (2016) American Chemical Society. $^{7}$Fig. 9 E-G are adapted with permission from ACS Nano, Vol. 8 Issue 8, X. Sun, X. Huang, X. Yan, Y. Wang, J. Guo, O. Jacobson, et al. Chelator-free (64)Cu-integrated gold nanomaterials for positron emission tomography imaging guided photothermal cancer therapy, Pages 8438–46, https://pubs.acs.org/doi/10.1021/nn502950t, Copyright (2014) American Chemical Society. Permissions related to the material excerpted should be directed to the ACS.

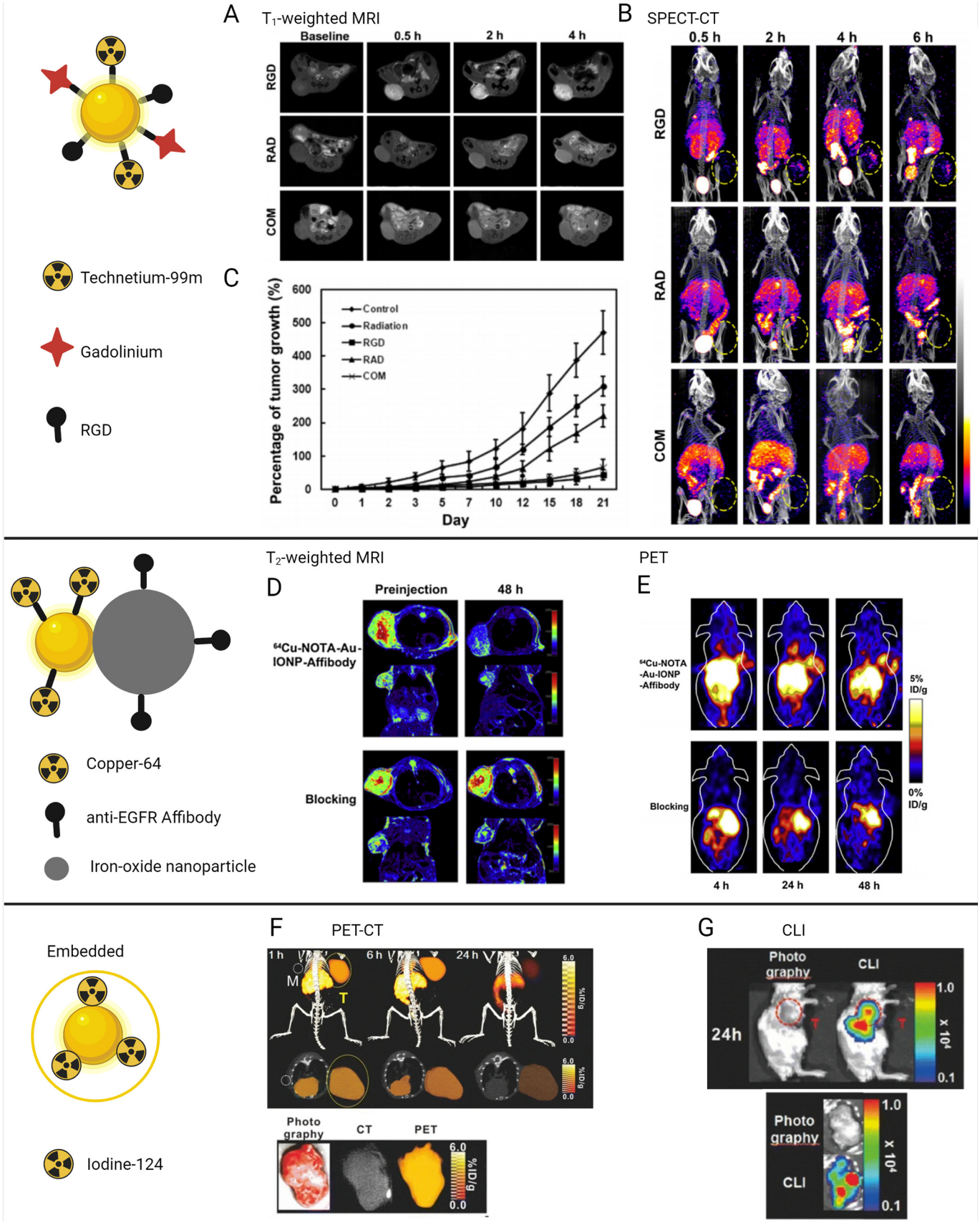
A
T1-weighted MRI
Baseline
0.5 h
2 h
4 h
RGD
RAD
COM
B
SPECT-CT
0.5 h
2 h
4 h
6 h
RGD
RAD
COM
Technetium-99m
Gadolinium
RGD
C
Percentage of tumor growth (%)
Control
Radiation
RGD
RAD
COM
Day
T2-weighted MRI
PET
D
Preinjection
48 h
64Cu-NOTA-Au-IONP-Affibody
Blocking
E
64Cu-NOTA-Au-IONP-Affibody
Blocking
5% ID/g
0% ID/g
4 h
24 h
48 h
Copper-64
anti-EGFR Affibody
Iron-oxide nanoparticle
F
PET-CT
1 h
6 h
24 h
M
T
%ID/g
Photography
CT
PET
G
CLI
Photography
CLI
24h
x 10⁴
Embedded
Iodine-124

tion (0.25–2 W/cm$^2$) inhibiting tumor growth and tumor metabolic activity (Fig. 9 A-G) [72,122].

Yang, et al., combined SPECT-CT and high-resolution MRI by conjugating 29 nm, 51 nm and 80 nm cRGD-AuNPs to technetium-99m and gadolinium (Fig. 10 A-C). From the three different AuNP sizes that were investigated, the 29 nm-sized AuNPs showed the greatest accumulation in the non-small-cell lung xenograft in mice. The authors found hyper-intense MRI signals in the tumor region, 30 min post-IV injection of 29 nm Tc/Gd-cRGD-AuNPs, after which the MRI signal intensity gradually increased to values that were 2.4 times higher than the baseline signal, reaching a plateau 2 h after injection. In addition, the MRI signal enhancement is much less pronounced in mice that received the untargeted Tc/Gd-AuNPs probes or free cRGD, which block the tumor binding sites (Fig. 10 A). The SPECT-CT images confirm the MRI observation, demonstrating high tumor accumulation of 29 nm [$^{99m}$Tc]Tc/Gd-cRGD-AuNPs (14.6% ID/g) after 2 h, which strongly reduces after blocking (6.2% ID/g) or after administration of the untargeted [$^{99m}$Tc]Tc/Gd-AuNPs probe (4.0% ID/g) (Fig. 10 B). However, SPECT-CT also reveals that the [$^{99m}$Tc]Tc/Gd-cRGD-AuNPs are present in the liver (≈20% ID/g) and spleen (≈55% ID/g). Furthermore, *ex vivo* studies demonstrate a high $^{99m}$Tc-content in the urine (>60% ID/g), while the amount of gold in the urine was low (≈10% ID/g), which demonstrates the detachment of technetium-99m from the AuNPs. Due to the size limitations during glomerular filtration, the presence of gold in the urine from the relatively large sized 29 nm, 51 nm and 80 nm AuNPs may be an indication of temporary kidney damage [153]. However, the authors did not observe any lesions, inflammation or other histological abnormalities in the kidneys. The [$^{99m}$Tc]Tc/Gd-cRGD-AuNPs are potentially suitable for image-based therapy as the authors were able to define the optimal time point post-injection at which the AuNP content in the tumor site was maximal to perform EBRT and benefit from the AuNP radiosensitization effect (Fig. 10 C) [66]. Alternatively, a targeted PET/MRI imaging probe was created by developing a multicomponent system consisting out of (I) AuNPs, which were radiolabeled with copper-64, and (II) iron-oxide nanoparticles (IONPs), which acted as MRI reporters and were conjugated to anti-EGFR affibodies (Fig. 10 D-E). The Au-IONPs show a similar $T_2$ relaxation rate of water as Feridex, a colloidal superparamagnetic iron oxide MRI contrast agent, and reduces the MR signal intensity at the tumor site by 44% on $T_2$-weighted MRI images, 48 h after IV injection in squamous cell carcinoma-bearing mice (Fig. 10 D). Next to RES accumulation, the PET images shows high tumor uptake (4.6% ID/g, 24 h p.i.) and a good tumor-to-muscle ratio of approximately 6 (Fig. 10 E). Blocking the tumor binding sites reduces the tumor uptake (1.9% ID/g, 24 h p.i.), resulting in a tumor-to-muscle ratio of approximately 2 and abolishes the effect on the MRI and PET signal intensity in the tumor region (Fig. 10 D-E) [132].

Another multimodal imaging possibility was demonstrated by coupling and embedding the positron-emitting iodine-124 in PEGylated gold core nanoballs (AuCBs) ([$^{124}$I]I-Au@AuCBs-PEG), which allowed *in vivo* PET-CT scanning and optical Cerenkov luminescence imaging (CLI). CLI is based on the detection of Cerenkov photons, which arise from charged particles originating from the radionuclide decay and traveling through a dielectric medium with a velocity exceeding the speed of light in the given medium. Particle deceleration polarizes the electrons of water molecules, which relax back to the equilibrium by emitting photons [154]. CLI can compensate for the relatively low spatial resolution of PET imaging, while PET overcomes the penetration depth limitation of the optical CLI imaging. Furthermore, CLI provides the opportunity to utilize existing clinical radiotracers for image-guided surgery. Despite the significant uptake in the liver and spleen, the PET-CT imaging shows a rapid accumulation of [$^{124}$I]I-Au@AuCBs-PEG in a xenograft breast tumor lesion as early as 1 h post-IV injection in mice (5.38% ID/g). Thereafter, the signal decreases, but remains detectable at 24 h post-injection (1.81% ID/g) with a desirable tumor-to-muscle (T/M) ratio of approximately 5 (Fig. 10 F). The authors do not demonstrate early time point evaluations of CLI imaging (1 h). However, consistent with the PET-CT results, *in vivo* CLI imaging also visualizes the uptake of the [$^{124}$I]I- Au@AuCBs-PEG in the tumor at 24 h post-injection (Fig. 10 G). As a result, there is a good linearity between the PET-CT and CLI imaging at 24 h ($R^2 = 0.85$) [90].

In addition, PET-CLI imaging is useful to detect sentinel lymph nodes (SLNs) after subcutaneous injection of [$^{124}$I]I –AuNP-PEG. SLNs are the first lymph nodes to which cancer cells of the primary tumor are likely to spread. Therefore, detection of the SLNs are required in order to determine the clinical cancer stage. The PET-CLI images show [$^{124}$I]I-AuNP-PEG uptake in the SLNs as early as 1 h post-injection (≈30% ID/g). The signal intensity increases to a maximum after 6 h and remains evident after 24 h (≈10% ID/g) [78]. As a result, PET/CLI could facilitate the clinical staging of cancer. Similarly, SLNs are also successfully imaged using SPECT-CT at 0.5 h, 1 h, 4 h and/or 24 h after subcutaneous injection of $^{99m}$Tc-labeled polymer-entrapped AuNPs and [$^{99m}$Tc]Tc-AuNP-mannose [52,63,146]. Conjugation of the AuNPs with mannose helps to improve the uptake of the [$^{99m}$Tc]Tc-AuNPs, since it targets the lymph node macrophages [52].

### 3.2.2. Dual radiolabeling

Alternative to multimodal imaging, dual radiolabeling of AuNPs with indium-111 and iodine-125 enables multispectral SPECT imaging, in which the emissions from iodine-125 and indium-111 are independently tracked at a window centered around 28 keV and 200 keV, respectively. Multispectral imaging helps to study the radiolabeling stability, the radionuclide anchor stability and biological parameters, such as enzyme activity. For example, indium-111 and iodine-125 are specifically linked to a matrix metallopeptidase 9 (MMP9) -cleavable peptide, which in turn is conjugated to the AuNPs. Indium-111 and iodine-125 are separated from each other by the cleaving sequence,

**Fig. 10.** Multimodal imaging. (A) $T_1$-weighted MR imaging of H1299 tumor-bearing mice at different time points after IV injection with 29 nm Gd/Tc-AuNPs-RGD (RGD), untargeted Gd/Tc-AuNPs-RAD (RAD) or Gd/Tc-AuNPs-RGD plus free RGD peptide (COM). Gd/Tc-AuNPs-RGD show an increased tumor uptake compared to the untargeted Gd/Tc-AuNPs-RAD and after blocking with free RGD. (B) SPECT/CT imaging of H1299 tumor-bearing mice at different time points after IV injection with Gd/[$^{99m}$Tc]Tc-AuNPs-RGD, untargeted Gd/[$^{99m}$Tc]Tc-AuNPs-RAD, or Gd/[$^{99m}$Tc]Tc-AuNPs-RGD plus free RGD peptide. Gd/[$^{99m}$Tc]Tc-AuNPs-RGD show an increased tumor uptake compared to the untargeted Gd/[$^{99m}$Tc]Tc-AuNPs-RAD and after blocking with free RGD. (C) Tumor growth curves following different treatment modes. Mice were IV injected with 29 nm Gd/Tc-AuNPs-RGD, Gd/Tc-AuNPs-RAD or Gd/Tc-AuNPs-RGD plus free RGD peptide at a dose of 2.5 mmol of Au/kg. Radiotherapy with 10 Gy of γ-ray irradiation was performed 4 h post-IV injection. Control groups received PBS. Gd/Tc-AuNPs-RGD enhance tumor radiotherapy. A-C are adapted from [66][8]. (D) *in vivo* $T_2$-weighted MR images of A431 tumor-bearing mice acquired before and at 48 h after IV injection of [$^{64}$Cu]Cu-NOTA-Au-IONP-Affibody and of a blocking dose of Affibody. (E) Coronal PET images of A431 tumor-bearing mice acquired 4 h, 24 h and 48 h after IV injection of [$^{64}$Cu]Cu-NOTA-Au-IONP-Affibody and the blocking dose of Affibody. [$^{64}$Cu]Cu-NOTA-Au-IONP-Affibody show excellent and specific tumor imaging ability. D-E are reprinted from [132][9]. (F) 3D and axial PET/CT images show uptake of [$^{124}$I]I-Au@AuCBs-PEG in breast cancer lesions of tumor-bearing mice after IV injection. White and yellow circles indicate muscle and tumor lesions, respectively. Ex vivo PET image of an excised tumor. (G) Photographs with CLI images showing uptake of [$^{124}$I]I-Au@AuCBs-PEG in breast cancer lesions of tumor-bearing mice, 24 h after IV injection. Ex vivo CLI image of an excised tumor. F-G are adapted from [90][10]. (For interpretation of the references to colour in this figure legend, the reader is referred to the web version of this article.) [8]Fig. 10 A-C are adapted with permission from ACS Appl Mater Interfaces, Vol. 8 Issue 3, Y. Yang, L. Zhang, J. Cai, X. Li, D. Cheng, H. Su, et al., Tumor Angiogenesis Targeted Radiosensitization Therapy Using Gold Nanoprobes Guided by MRI/SPECT Imaging, Pages 1718–32, Copyright (2016) American Chemical Society. [9]Fig. 10 D-E are reprinted from Biomaterials, Vol. 34 Issue 11, M. Yang, K. Cheng, S. Qi, H. Liu, Y. Jiang, H. Jiang, et al., Affibody modified and radiolabeled gold-iron oxide hetero-nanostructures for tumor PET, optical and MR imaging, Pages 2796–806, Copyright (2013), with permission from Elsevier. [10]Fig. 10 F-G are adapted from S. B. Lee, D. Kumar, Y. Li, I. K. Lee, S. J. Cho, S. K. Kim, et al., PEGylated crushed gold shell-radiolabeled core nanoballs for *in vivo* tumor imaging with dual positron emission tomography and Cerenkov luminescent imaging, J Nanobiotechnology, Vol. 16 Issue 1, https://jnanobiotechnology.biomedcentral.com/articles/10.1186/s12951-018-0366-x. Open access article distributed under the terms of the Creative Commons BY 4.0 license (https://creativecommons.org/licenses/by/4.0/). Copyright (2018) The Author(s). No changes were made to the images.

which means that upon peptide cleavage by MMP9, indium-111 is released, while iodine-125 should remain attached to the AuNP. However, 4 h after IV injection in tumor-bearing mice, iodine-125 is detected in the thyroid, stomach and bladder, indicating that radioiodination of the tyrosine residue in the peptide is lacking *in vivo* stability, whereas indium-111 remains chelated to the AuNPs, circulating in the blood pool. Tumor uptake was clearly visible 24 h post-injection in both MMP9-high expressing A431 squamous cell carcinoma and MMP9-low expressing 4T1Luc breast cancer due to the EPR effect, leading to a high T/M ratio of 8, after 48 h. However, due to the high MMP9 enzyme activity in the A431 tumor, the $^{111}$In-labeled peptide is cleaved from the AuNPs, facilitating its tissue clearance and potentially its kidney excretion. As a result, the $^{111}$In-signal intensity in the MMP9-high A431 tumor reduces between 24 h and 48 h (from 7.25 to 6.23% ID/g). In contrast, the signal intensity in the MMP9-low 4T1Luc tumor continues to increase (from 6.41 to 10.2% ID/g), indicating a low MMP9 enzyme activity [82]. Dual radiolabeling is also useful to establish the biodistribution of multi-component AuNPs. This was proven by IV administration of [$^{198}$Au]AuNPs with a [$^{14}$C]C-citrate surface coating to rats. Gamma spectrometry and liquid scintigraphy were used to detect and quantify the gold-198 and carbon-14 activity in the *ex vivo* organs, respectively. Interestingly, the biodistribution profile of the gold core and the citrate coating were different from each other and thus the authors concluded that the different components of the AuNPs separated one from each other and that the AuNPs did not remain intact [155].

### 3.3. Treatment

For therapeutic purposes, the goal of radiolabeled AuNPs is to deliver a lethal radiation dose to the tumor site, while minimizing the radiation damage to healthy tissue. The effectiveness of radiolabeled AuNPs for TRT and as multimodal therapeutic agents has been investigated *in vitro* and *in vivo*. These studies are presented in detail in Table 3.

#### 3.3.1. In vitro experiments

Radiolabeled AuNPs can potentially increase the effectiveness of TRT. For instance, *in vitro*, AuNPs conjugated to Lys$^3$-bombesin (Tat-BN) and radiolabeled with technetium-99m are stronger inhibitors prostate cancer cell (PC-3) proliferation (cell proliferation of <10%) than the monomeric [$^{99m}$Tc]Tc-Tat-BN without AuNPs (cell proliferation of ≈37%). Furthermore, the research group demonstrated an enhanced PC-3 cytotoxic effect of dual-radiolabeled [$^{99m}$Tc]Tc/[$^{177}$Lu]Lu-AuNP-Tat-Bn as compared to the single radiolabeled [$^{177}$Lu]Lu-AuNP-Tat-BN or [$^{99m}$Tc]Tc-AuNP-Tat-BN, which is attributed to the biological effects of Auger electrons and low-energy internal conversion of technetium-99m [50]. In line with the results of [$^{99m}$Tc]Tc-Tat-BN, the [$^{177}$Lu]Lu-AuNPs-RGD inhibited glioma cell (C6) proliferation (cell proliferation of 3.62%) significantly more as compared to the monomeric [$^{177}$Lu]Lu-RGD (cell proliferation of 29.67%) without AuNPs [49].

The combination of TRT with photothermal therapy was studied *in vitro*, showing radiotoxicity of [$^{99m}$Tc]Tc/[$^{177}$Lu]Lu-AuNP-Tat-BN and dendrimer-entrapped [$^{177}$Lu]Lu-AuNP conjugated to folate and bombesin ([$^{177}$Lu]Lu-DenAuNPs-folate-bombesin) in prostate cancer cells and breast cancer cells, while the corresponding unlabeled analogs, DenAuNP-folate-bombesin and AuNPs-Tat-BN, exhibit thermo-ablative properties following laser irradiation at 532 nm for 6 min (0.65 W/cm$^2$). It is important to note that laser irradiation at 532 nm, close to the SPR peaks of the respective AuNPs, has a limited clinical application, due to its poor tissue penetration [50,158]. Nevertheless, the studies highlight a proof-of-principle for future research on the TRT/photothermal combination therapy.

Various *in vitro* studies demonstrate that the conjugation of targeting ligands directed against EGFR1 (Cetuximab or EGF) or EGFR2 (Trastuzumab or Panitumumab) increases the effectiveness of AuNPs, radiolabeled with iodine-131, indium-111, lutetium-177, gold-198 or astatine-211, to reduce the viability of EGFR1- or EGFR2-expressing cancer cells, respectively [60,61,84,95,156,159]. First, [$^{111}$In]In-AuNPs-Trastuzumab, [$^{177}$Lu]Lu-AuNP-Panitumumab, [$^{177}$Lu]Lu-AuNPs-Trastuzumab and [$^{211}$At]At-AuNP-PEG-Trastuzumab show a higher cytotoxic effect than their untargeted, radiolabeled AuNPs analogs [61,95,156,159]. Second, increasing the EGF load on [$^{111}$In]In-EGF-AuNPs increases its cytotoxic efficacy [60]. Third, cancer cells with a low or intermediate HER1/HER2 expression profile are less affected by the targeted radiopharmaceuticals as compared to the cells with a high receptor expression [60,61,156,159]. Finally, pre-blocking the binding sites on A549 lung cancer cells diminishes the cytotoxic effect of [$^{131}$I]I-Cetuximab-AuNPs [84].

#### 3.3.2. Intravenous injection in tumor-bearing mice

There are a limited number of *in vivo* studies, which intravenously inject radiolabeled AuNPs to investigate their use as potential agents for TRT. For instance, IV administration of 7 doses of polyethylenimine-entrapped AuNPs, radiolabeled to iodine-131 and conjugated to chlorotoxin ([$^{131}$I]I-Au PENPs-BmK CTX and [$^{131}$I]I-Au PENPs-CTX) in glioma-bearing mice over a period of 3 weeks significantly slows down the tumor growth and prolongs the survival as compared to the saline control, the untargeted AuNP analogs or the non-radioactive AuNP analogs [81,151]. In addition, a single IV injection with three different doses of [$^{198}$Au]AuNPs-RGD, 18.5 MBq, 37 MBq and 55.5 MBq, in melanoma-bearing mice significantly retarded the tumor growth. More specifically, the tumor growth retardation enhances as the dose increased, with a minimal tumor growth delay using 18.5 MBq and with tumor regression using doses of 37–55.5 MBq. However, the body weight of the mice treated with 55.5 MB of [$^{198}$Au]AuNPs-RGD reduced by 10–15% over a period of 15 days, potentially due to radiotoxicity [164]. Next to the delivery of radionuclides to the tumor site, radiolabeled AuNPs can also act as radiosensitizers. This was investigated *in vivo,* where SPECT-CT imaging was used to define the maximal tumor delivery of iodine-125 after IV administration of [$^{125}$I]I-cRGD-AuNPs in small cell lung cancer-bearing mice, which was then followed by EBRT. Combined [$^{125}$I]I-cRGD-AuNPs and EBRT suppress the tumor growth more effectively during 21 days as compared to no treatment, EBRT alone, AuNPs+EBRT and cRGD-AuNPs +EBRT. However, there is no significant difference in the apoptotic degree caused by [$^{125}$I]I-cRGD-AuNPs and cRGD-AuNPs, 2 days after EBRT. The authors suggested that a significant increase in therapeutic efficacy might be possible if iodine-125 is exchanged by iodine-131, which has a higher therapeutic potency [83].

#### 3.3.3. Nanobrachytherapy: the Intratumoral injection of radiolabeled AuNPs in tumor xenografts

The majority of the research assessing the effectiveness of radionuclide therapy using radiolabeled AuNPs *in vivo* chose for an intratumoral route of administration, usually with the aim to improve the therapy of localized prostate cancer or breast cancer [49,105,127,156,159–163,165]. As mentioned before, studies comparing the biodistribution of radiolabeled AuNPs after IT administration and IV administration demonstrate that intratumoral administration maximizes the tumor concentration of the radiolabeled AuNPs and minimizes the accumulation in healthy tissue, such as the liver and spleen, compared to IV injection [110–114,156]. Furthermore, the intratumoral administration strategy of radiolabeled AuNPs is suggested as a potential alternative for the implantation of conventional radioactive seeds during interstitial brachytherapy, called nanobrachytherapy (Fig. 11) [127,165,167]. Interstitial brachytherapy is based on the implantation of millimeter-sized radioactive seeds in or near the tumor, providing a continuous dose delivery. The implantation of the radioactive seeds is often permanent for the treatment of prostate cancer. Although successful, there are certain limitations associated to this mode of therapy. For instance, the implantation procedure using catheters is invasive, causes bleeding and discomfort, and has an increased risk on trauma, edema, urinary obstruction and pain during urination. In addition, since each seed typically has an activity ranging between 18.5- and 74 MBq, the intratumoral dose distribution in the prostate gland is

**Table 3**
Overview of radiolabeled gold nanoparticles under pre-clinical investigation for their therapeutic potentials.

| Isotope | Particle name | Size (nm) | Functionalization | Labeling method | Cell model, administration | In vitro/in vivo | Purpose | Therapeutic effect | Reference |
|---|---|---|---|---|---|---|---|---|---|
| Iodine-131 | [$^{131}$I]I-C225-AuNPs-PEG | 52.9 | Cetuximab (C225) | Covalent | A549, Human lung cancer IV, 18.5 MBq | In vitro & In vivo | TRT in vitro SPECT-CT in vivo | %CS: [$^{131}$I]I-C225-AuNPs: 37 (2 h) %CS after blocking: >82. T/M: 3.9 (2 h) – 5.5 (4 h) | Kao, et al. [84] |
| | [$^{131}$I]I-Au PENP-BmK CTX | 147 | Chlorotoxin-like peptide (T) Untargeted (UT) | Covalent | C6, rat glioma, IV 7 × 9.25 MBq, 100 μl | In vivo | Targeted SPECT-CT and TRT | Tumor volume increased 17-22× (controls), 20× (UT) and 7× (T) after 3 weeks. Treatment with T results in prolonged survival compared to UT. Higher tumor SPECT (2×) and CT (1.67×) signal intensities compared to UT-form, 6-8 h p.i. | Sun, et al. [81] |
| | [$^{131}$I]I-Au PENPs-CTX | 151 | Chlorotoxin (T) Untargeted (UT) | Covalent | C6, rat glioma, IV 7 × 7.4 MBq, 100 μl | In vivo | Targeted SPECT-CT and TRT | Treatment with T leads to higher tumor SPECT (2.2–2.4×) and CT (1.7×) signal intensities compared to treatment with UT, 6-8 h p.i. Tumor volume increased 18.2× (UT), 9.7× (T) and 19.6–21.9× (controls). Survival time after treatment with T was significantly longer than after treatment with UT. | Zhao, et al. [151] |
| | [$^{131}$I]I(0)-AuNRs-PEG | 70.6 × 10.8 | PEG | Absorption | MCF-7, human breast cancer, IT 1.85 MBq | In vitro and In vivo | TRT and PTT | Cellular uptake after 24 h: barely uptake of Na[$^{131}$*I*]I and 32.1% of [$^{131}$I]I(0)-AuNRs. Cell viability after radionuclide therapy and PTT: - 6 μCi: Na[$^{131}$*I*]I: no therapeutic effect vs. [$^{131}$I]I (0)-AuNRs: 73.96% - PTT: [$^{131}$I]I(0)-AuNRs: 60.81% - 6 μCi + PTT: [$^{131}$I]I(0)-AuNRs: 31.09% More effective tumor growth inhibition by [$^{131}$I]I (0)-AuNRs-PEG than free iodine-131. Combining TRT and PTT leads to tumor regression. | Wang, et al. [97] |
| Iodine-125 | [$^{125}$I]I-cRGD-AuNPs | 45.2 | Cyclic RGD | Covalent | NCI-H446, human small cell lung carcinoma, IV 37 MBq, 100 μl | In vivo | RT and TRT. SPECT-CT | T/NT tumor uptake ratio: 2.07 (1 h) - 4.76 (2 h) - 4.25 (4 h). T/NT apoptosis ratio (2 days after RT): RT+[$^{125}$I] I-cRGD-AuNPs: 11.2\| RT + cRGD-AuNPs: 9.8\| RT + AuNPs: 5.5 \| RT alone: ≈5 \| no treatment: ≈3% increase in tumor vol. (grams) (after 21d): Control: 312 (0.538) \| RT: 137 (0.209) \|RT + AuNPs: 85.5 (0.171)\| RT+ cRGD-AuNPs: 33.1 (0.113) \| RT+[$^{125}$I] I-cRGD-AuNPs: 15.2 (0.116) ➔Therapeutic effect of [$^{125}$I]I- cRGD-AuNPs+RT not significantly improved compared to cRGD-AuNPs+RT. | Su, et al. [83] |
| Indium-111 | [$^{111}$In]In-EGF-Au NPs | 14 | EGF | Chelation | MDA-MB-468, MCF-7, human breast cancer | In vitro | TRT | SF MDA-MB-453: 42.8%. Increasing the EGF loading on the AuNP, reduces the SF to 17.1%. Not toxic to MCF-7 | Song, et al. [60] |
| | [$^{111}$In]In-AuNPs-Trastuzumab | 30 | Trastuzumab (T) Untargeted (UT) | Chelation | MDA-MB-361 (intermediate) IT,10 MBq, 100 μl SK-BR-3 (high) Human breast cancer | In vitro & in vivo | TRT | T form was internalized more efficiently in the perinuclear region, lead to more DSBs and cell death in both cell types than the UT form. The uptake and cell death is higher in SK-BR-3 cells than in MDA-MB-361 cells treated with T form. T form arrested tumor growth over 70 days. Control: 8× tumor volume increase over 70 days Absorbed dose: T: 60.5 Gy – UT: 28.4 Gy (48 h) | Cai, et al. [156] |
| Lutetium-177 | [$^{177}$Lu]Lu-AuNPs-cRGD | 26.6 25.6 | Cyclic RGD (T) Untargeted (UT) | Chelation | C6, rat glioma IT, 4 × 2 MBq, 50 μl | In vivo | Radionuclide therapy | Inhibited C6 cell proliferation (3.6%) compared to UT form (6.3%) and [$^{177}$Lu]Lu-cRGD (29.7%). % ID/g (T): 68.1 (3 h) - 34.7 (96 h) \| $SUV_{18F\text{-}FDG}$: 0.335 (23d) % ID/g (UT): 48.2 (3 h) - 25.5 (96 h) \| $SUV_{18F\text{-}FDG}$: 0.584 (23d) | Vilchis-Juarez, et al. [49] |

*(continued on next page)*

**Table 3** *(continued)*

| Isotope | Particle name | Size (nm) | Functionalization | Labeling method | Cell model, administration | In vitro/in vivo | Purpose | Therapeutic effect | Reference |
|---|---|---|---|---|---|---|---|---|---|
| | | | | | | | | % ID/g ([$^{177}$Lu]Lu-cRGD): 26.8 (3 h) - 5.7 (96 h) \| $SUV_{18F\text{-}FDG}$: 2.740 (23d)<br>Absorbed dose: T: 63.8 Gy - UT: 38.3 Gy - [$^{177}$Lu]Lu-RGD: 16.6 Gy (23d)<br>T treatment: Tumor size was 27× smaller than control, 12× smaller than [$^{177}$Lu]Lu-cRGD and 3× smaller than UT treatment (23d). | |
| | [$^{177}$Lu]Lu-T-AuNPs | 67.3<br>45.8 | Panitumumab (T)<br>Untargeted (UT) | Chelation | MDA-MB-468 (high)<br>MDA-MB-231 (moderate)<br>MCF-7 (low), human breast cancer | In vitro | TRT in vitro | %CS (high) T: 21.7 (1.5 MBq) - 0.1 (3 MBq) - <0.001 (4.5 MBq)<br>%CS (high) UT: 43.1 (1.5 MBq) - 22.5 (3 MBq) - 8.4 (4.5 MBq)<br>%CS (mod) T: 58.1 (1.5 MBq) - 46.4 (3 MBq) - 33.8 (4.5 MBq)<br>%CS (mod) UT: 84.2 (1.5 MBq) - 64.8 (3 MBq) - 51.6 (4.5 MBq)<br>%CS (low) T: 64.1 (1.5 MBq) - 30.3 (3 MBq) - 25.8 (4.5 MBq)<br>%CS (low) UT: 54.3 (1.5 MBq) - 31.9 (3 MBq) - 32.3 (4.5 MBq) | Yook, et al. [61] |
| | [$^{177}$Lu]Lu-T-AuNPs | 67.3<br>45.8 | Panitumumab (T)<br>Untargeted (UT) | Chelation | MDA-MB-468, human breast cancer<br>IT, 4.5 MBq, 30 μl | In vivo | Radionuclide therapy | % ID/g (T): 465.7 (1 h) and 196.6 (48 h)<br>% ID/g (UT): 341.1 (1 h) and 99.0 (48 h)<br>TGI of T was 35× lower (0.3) than TGI of control (11.1) (90d). No difference in TGI of T (0.3) and UT form (0.8). Mice treated with T and UT survived for 120d. Controls survived for 75-86d. Absorbed dose: T: 30.37 Gy - UT: 21.86 (48 h) | Yook, et al. [157] |
| | [$^{177}$Lu]Lu-DenAuNPs-folate-bombesin | 1–2.9 | Folate – bombesin (T)<br>Untargeted (UT) | Chelation | T47D, human breast cancer | In vitro | Optical imaging, PTT and TRT in vitro | Absorbed dose: T: 15.1 Gy – UT: 63.2 Gy (72 h, 14.8 Bq/cell)<br>Cell lethality 4 times higher after exposure to T form, compared to UT form. | Mendoza-Nava [158] |
| | [$^{177}$Lu]Lu-AuNPs-Trastuzumab | 30 | Trastuzumab (T)<br>Untargeted (UT) | Chelation | MDA-MB-361 (intermediate), IT, 3 MBq, 30 μl<br>BT-474 (high)<br>SK-BR-3 (high)<br>Human breast cancer | In vivo | TRT in vitro and in vivo | T form was internalized more in BT-474 and SK-BR-3 cells than in MDA-MB-361 cells. The T form was internalized and retained more efficiently than the UT form in SK-BR-3 cells, and lead to more DSBs and cell death.<br>TGI after 16 days: (T) = 2.5 \| (UT) = 4.2 \| (saline) = 5.6 | Cai, et al. [159] |
| Lutetium-177/ Technetium-99m | [$^{99m}$Tc]Tc/[$^{177}$Lu]Lu-AuNPs-Tat-BN | 8.07 | Bombesin/TAT (49–57) (T)<br>Untargeted (UT) | Chelation | PC-3, human prostate cancer | In vitro | PTT and TRT in vitro | 52% more internalization than UT form. Significantly inhibited cell proliferation compared to UT form or [$^{99m}$Tc]Tc-Tat-BN. | Jimenez-Mancilla, et al. [50] |
| Gold-198 | [$^{198}$Au]AuNPs-GA | 85 | Gum arabic | Incorporation | PC-3, human prostate cancer<br>IT, 15 MBq, 30 μl | In vivo | Radionuclide therapy | 3 weeks after treatment, tumor volume of treated group was 82% smaller (0.17 $cm^3$) as compared to the control group (0.86 $cm^3$). After 31 days: % ID: 19.9 | Chanda, et al. [160] |
| | [$^{198}$Au]AuNPs-EGCg | 80 | epigallocatechin-gallate | Incorporation | PC-3, human prostate cancer<br>IT, 5 MBq, 30 μl | In vivo | Radionuclide therapy | 72% tumor retention (24 h) - % ID: 37.4 (42d)<br>80% tumor volume reduction after 28 d (reduced by 0.28 $cm^3$) compared to controls (reduced by 0.05 $cm^3$) | Shukla, et al. [161] |
| | [$^{198}$Au]AuNPs-GA | 85 | Gum arabic | Incorporation | Naturally occurring prostate cancer, IT,<br>111–666 MBq, 100–200 μl | In vivo | Radionuclide therapy | % ID: 53 (30 min). Tumor volume was stable ($n = 6$) or reduced by 30–50% ($n = 2$). One dog had a tumor volume increase of 26%. | Axiak-Bechtel, et al. [162] |
| | [$^{198}$Au]AuNPs-MGF | 35 | Mangiferin | Incorporation | PC-3, human prostate cancer<br>IT, 6 MBq, 30 μl | In vivo | Radionuclide therapy | % ID: 80.98 (0.5 h) - 79.82 (24 h) – 60.96-69.7 (24d)<br>Tumor volume treated group: 0.18–0.22 $cm^3$ (stable) (24d) | Al-Yasiri, et al. [163] |

| | | | | | | | | |
|---|---|---|---|---|---|---|---|---|
| | [$^{198}$Au]AuNP-RGD | 12.5 | RGD (T) | Incorporation | B16F10, mouse melanoma, IV, 18.5 MBq, 37 MBq, 55.5 MBq | In vivo | Radionuclide therapy | Tumor volume control group: 1.31 $cm^3$ (6.5× increase) (24d)<br>% ID/g: 4.9–8.7 - 7.6 - 6.6 - 5.1 (1 h - 4 h - 24 h -72 h - 168 h)<br>% ID/g (blocked): 2.9 (4 h) - % ID/g (UT): 3 (4 h)<br>T/M: 9.6–29.8 (1 h - 168 h)<br>T/Bl: 1.4–10 (1 h - 168 h)<br>T/Li: 0.19–1.2 (1 h - 168 h)<br>Tumor growth retarded in treated mice compared to saline or AuNP-RGD. The growth deceleration enhanced with increasing dose. Mice treated with 37.0–55.5 MBq reduced in TGI. No change in body weight of mice treated with 18.5–37.0 MBq. There was 10–15% decrease in body weight of mice treated with 55.5 MBq. | Chakravarty [164] |
| Gold-199/ Palladium-103 | [$^{103}$Pd]Pd@ AuNPs-PEG (group 1)<br>[$^{103}$Pd]Pd@[$^{198}$Au]AuNPs-PEG (group 2) | 36–48 | PEG | Encapsulation | PC-3, human prostate cancer IT, 59–63 MBq, 4 μl | In vivo | Low-dose radionuclide therapy | After 4 weeks: Control group reached endpoint<br>Tumor volumes of treated group 1 were 56% smaller<br>Tumor volumes of treated group 2 were 75% smaller, but severe skin necrosis.<br>Prolonged survival compared to control: 38-62d or > 80d. | Laprise-Pelletier, et al. [127] |
| Palladium-103 | [$^{103}$Pd]Pd@Au nanoseeds | 140 | N.A. | Shell | PC-3, human prostate cancer IT, 55.5 MBq, 40 μl | In vivo | radionuclide therapy | % ID/g: 101.5 (24 h) – 274.5 (5w)<br>Tumor control $mm^3$: ([$^{103}$Pd]Pd@Au): 82.7 to 19.8 (5w) Metabolic activity decreased with 62% (5w)<br>Tumor control $mm^3$: (PBS): 67.1 to 187, (cold Au): 58.7 to 122 (5w) | Moeendarbari, et al. [165] |
| Actinium-225 | [$^{225}$Ac]Ac-Au@TADOTAGA | 5–9 | N.A. | Chelation | U87MG, human glioblastoma, IT, 3 × 5 kBq, 100 μl | In vivo | TRT in vivo | % IA/g: 60.67% (2 h) - 5.21% (228 h).<br>TGI of treated mice was 2.4-fold lower at 8 days and 3.9-fold lower at 22 days p.i. compared to saline control mice. | Salvanou, et al. [166] |
| Astatine-211 | [$^{211}$At] At-AuNPs-PEG-trastuzumab | 45.8<br>16.1 | Trastuzumab (T)<br>Untargeted (UT) | Adsorption | SKOV-3, human ovarian cancer | In vitro | TRT | $LD_{50}$ (T): 0.55 MBq/ml (24 h)<br>$LD_{50}$ (UT): 1.3 MBq/ ml (24 h)<br>Bioconjugates successfully penetrate SKOV-3 cells and were localized in the nuclear envelope area | Dziawer, et al. [95] |
| | [$^{211}$At]At-AuNPs-S-PEG-SP (5–11) | 24.6 | Substance P(5–11) (T)<br>Untargeted (UT) | Adsorption | T98G, human glioblastoma, 0.6 MBq | In vitro | TRT | metabolic activity: non-radiolabeled AuNP-S-PEG-SP (5–11): 88% (24 h)<br>metab. Act.: UT: ≈55% (24 h)<br>metab. Act.: T: ≈38% (24 h) | Dziawer, et al. [94] |

**Abbreviations:** AuNP: gold nanoparticle; Au-PENPs: polyethylenimine-entrapped gold nanoparticles; BmK-CTX: Buthus martensii Karsch chlorotoxin; CT: computed tomography; DenAuNPs: dendrimer conjugated gold nanoparticles; DSBs: double strand breaks; EGCg: epigallocatechin-gallate; EGF: epidermal growth factor receptor; FDG: fluorodeoxyglucose; GA: gum arabic; IT: intratumoral; IV: intravenous; LACT: *Lactobacillus rhamnosus*; $LD_{50}$: lethal dose for 50% of the cells; MGF: mangiferin; PEG: polyethylene glycol; p.i.: post-injection; PTT: photothermal therapy; RT: radiotherapy; SF: survival fraction; SPECT: single photon emission computed tomography; SP(5–11): substance P(5–11); SUV: standardized uptake value; T: targeted; TAT-Bn: TAT-bombesin; TGI: tumor growth index (ratio of the treated tumor volume by the initial tumor volume); T/M: tumor-to-muscle ratio; T/NT: target-to-non-target ratio; TRT: targeted radionuclide therapy; UT: untargeted; %CS: percentage of cell survival; % IA/g: percentage injected activity; % ID: percentage injected dose.

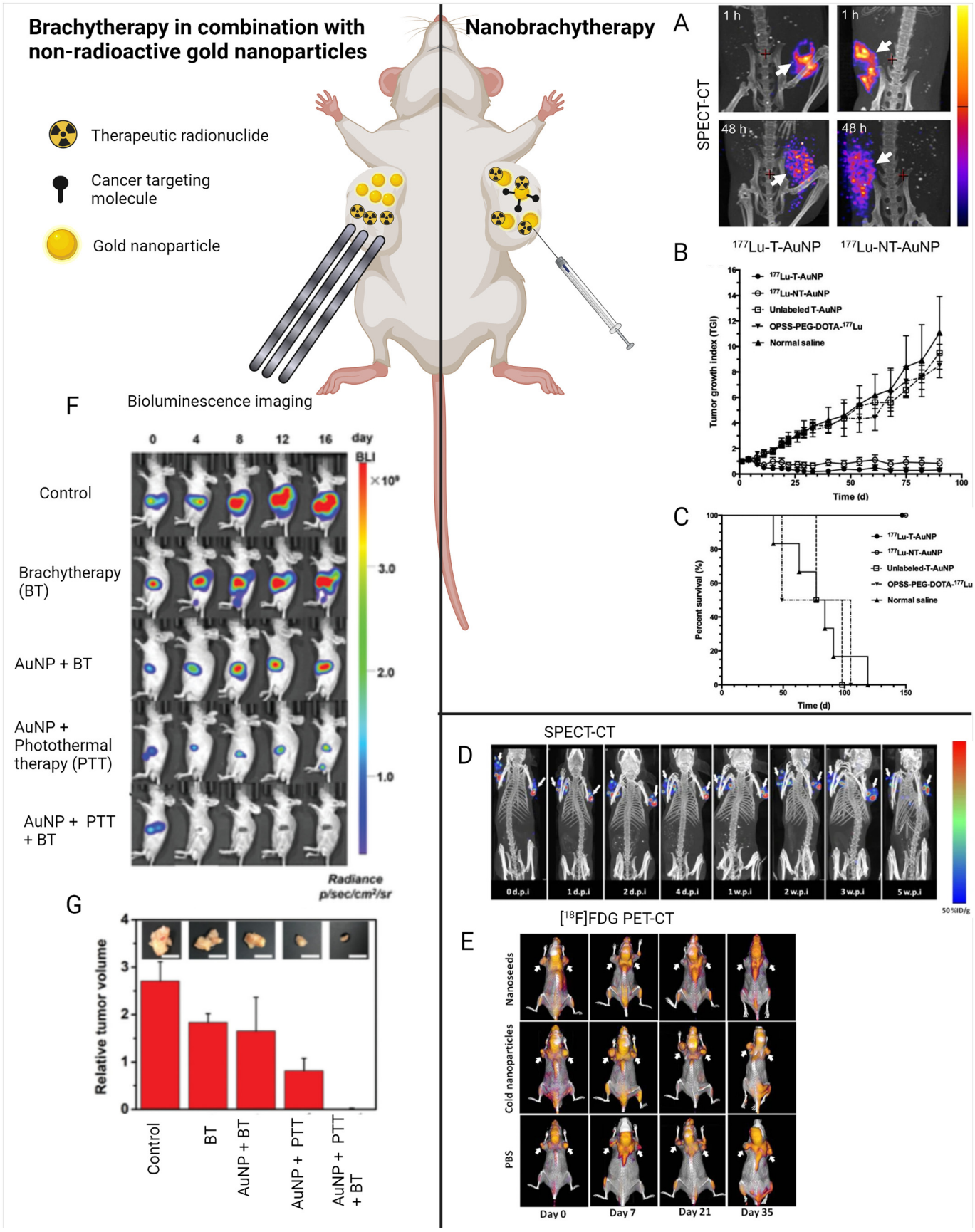
Brachytherapy in combination with non-radioactive gold nanoparticles
Therapeutic radionuclide
Cancer targeting molecule
Gold nanoparticle
Nanobrachytherapy
A
SPECT-CT
1 h
48 h
B
177Lu-T-AuNP
177Lu-NT-AuNP
Tumor growth index (TGI)
Time (d)
177Lu-T-AuNP
177Lu-NT-AuNP
Unlabeled T-AuNP
OPSS-PEG-DOTA-177Lu
Normal saline
C
Percent survival (%)
Time (d)
F
Bioluminescence imaging
day
BLI
Control
Brachytherapy (BT)
AuNP + BT
AuNP + Photothermal therapy (PTT)
AuNP + PTT + BT
Radiance p/sec/cm²/sr
G
Relative tumor volume
Control
BT
AuNP + BT
AuNP + PTT
AuNP + PTT + BT
D
SPECT-CT
0 d.p.i
1 d.p.i
2 d.p.i
4 d.p.i
1 w.p.i
2 w.p.i
3 w.p.i
5 w.p.i
%ID/g
E
[18F]FDG PET-CT
Nanoseeds
Cold nanoparticles
PBS
Day 0
Day 7
Day 21
Day 35

difficult to control and strongly depends on the correct positioning of the seeds [127,165]. Seed positioning errors can develop over time, which result in a heterogeneous dose distribution consisting out of hot and cold spots. In contrast, the injection of radiolabeled AuNPs would use much smaller needles, which could reduce the trauma. Furthermore, the dose delivery would be easier to control by adjusting the injection volume and would enable the treatment of smaller tumors. Local diffusion of small AuNPs from the injection site could facilitate the homogenization of the radiation dose in the tumor [166,167].

Importantly, although IT injection maximizes the concentration of AuNPs in the tumor, conjugation of targeting molecules is still useful. For instance, conjugation of Trastuzumab, Panitumumab, cRGD, pigallocatechin-gallate (EGCg) to AuNPs result in a >2 times prolonged tumor retention, compared to their untargeted radiolabeled AuNPs counterparts, which show a gradual tissue redistribution from the breast, prostate or glioma tumor site to the liver and spleen over time [49,157,159–161]. Furthermore, due to their relatively large size, 150 nm non-functionalized [$^{103}$Pd]Pd@Au nanoseeds show a prostate tumor xenograft retention of 5 weeks [165]. The significantly longer retention of [$^{198}$Au]AuNPs-EGCg (75 %ID/g after 24 h) within the prostate tumor compared to untargeted [$^{198}$Au]AuNPs (200 %ID/g after 24 h) allows to inject only one third of the activity, without compromising the tumor response (5 MBq for [$^{198}$Au]AuNP-EGCg vs 15 MBq for [$^{198}$Au]AuNP-GA) [160,161].

The longer tumor retention of the targeted AuNPs leads to a higher radiation dose delivered to the tumor. For instance, 48 h after injection of 10 MBq [$^{111}$In]In-AuNPs-Trastuzumab in a breast cancer xenograft, the cumulative absorbed radiation dose is estimated to be 60.5 Gy, compared to 28.4 Gy for untargeted [$^{111}$In]In-AuNPs [156]. Similarly, 48 h after injection of 4.5 MBq [$^{177}$Lu]Lu-AuNPs-Panitumumab in a breast cancer xenograft, the cumulative absorbed radiation dose is estimated to be 30.37 Gy, compared to 21.86 Gy for untargeted [$^{177}$Lu]Lu-AuNPs [157]. Finally, IT injection of 8 MBq of [$^{177}$Lu]Lu-cRGD-AuNPs in a glioma xenograft results in a cumulative absorbed radiation dose of 63.8 Gy after 23 days, compared to 38.3 Gy and 16.6 Gy for [$^{177}$Lu]Lu-AuNPs and [$^{177}$Lu]Lu-cRGD, respectively [49]. As a result, treatment of breast and prostate tumor xenografts with radiolabeled, targeted AuNPs inhibits the tumor growth and prolongs the survival of the treated mice, compared to the saline control (Fig. 11 A-C) [156,157,159–161,163]. In addition, [$^{177}$Lu]Lu-cRGD-AuNPs significantly reduces the glioma tumor metabolic activity, the intratumoral blood vessels formation and the VEGF tumoral gene expression, compared to the saline control group, [$^{177}$Lu]Lu-AuNPs and [$^{177}$Lu]Lu-cRGD [49]. Moreover, Wang, et al. confirmed the *in vitro* research on the possibility to combine TRT and PTT. The intratumoral injection of [$^{131}$I]I-AuNRs-PEG in breast cancer-bearing mice delayed the tumor growth more effectively than free iodine-131 therapy due to the higher accumulation of [$^{131}$I]I-AuNRs-PEG in the breast cancer cells. Tumor regression is observed when IT injection of [$^{131}$I]I-AuNRs-PEG is combined with photothermal therapy using 808 nm laser irradiation (1 W/cm$^2$) (Fig. 12) [97]. Due to the non-systemic, highly localized administration of the radiolabeled AuNPs into the tumor, the calculated absorbed radiation doses in the healthy organs was lower than 1.5 Gy [49,156,157]. Furthermore, the studies did not reveal significant tissue damage, inflammation, changes in serum alanine aminotransferase, creatinine and urea, and caused no decrease in blood cell counts [97,156,157,159–161,163].

One of the radionuclides used in the clinic during low-dose brachytherapy is palladium-103. Laprise-Pelletier produced core-shell nanoparticles (<50 nm) consisting of a core of radioactive $^{103}$Pd, surrounded by a shell of gold ([$^{103}$Pd]Pd@AuNPs-PEG). In addition, similar nanoparticles were co-labeled with the high-energy emitter gold-198 ([$^{103}$Pd]Pd@[$^{198}$Au]AuNPs-PEG). Four weeks after a single IT injection of 60 MBq of [$^{103}$Pd]Pd@AuNPs-PEG or [$^{103}$Pd]Pd@[$^{198}$Au]AuNPs-PEG in tumor-bearing mice, the PC3 prostate cancer xenograft volume decreases with 56% and 75%, respectively, as compared to the untreated controls. However, the tumor growth inhibition of [$^{103}$Pd]Pd@[$^{198}$Au]AuNPs-PEG is associated with severe necrosis at the skin of the treated mice. This observation is attributed to the emission of high-energy electrons and the long-range high-energy photons by gold-198, which could be a limitation of gold-198 when used for short-range nanobrachytherapy [127]. Alternatively, Moeendarbari, et al. produced $^{103}$Pd-coated gold nanoseeds, consisting of an 100 nm inner gold core and an outer shell of palladium-103. The [$^{103}$Pd]Pd@Au nanoseeds significantly inhibit the prostate tumor growth and reduce the tumor metabolic activity, 5 weeks after treatment, compared to the saline controls (Fig. 11 D-E) [165].

In contrast to the above described studies using AuNPs radiolabeled with lutetium-177, indium-111, gold-198 or palladium-103, there is one study investigating the use of AuNPs (5–9 nm) radiolabeled with the alpha-emitting $^{225}$Ac as nanobrachytherapeutic agents. The authors IT injected glioma xenografts in mice with a very low activity (a total of 15 kBq divided over three injections) and found tumor growth retardation over a period of 22 days and three times more necrotic lesions in the tumor compared to the saline-injected control group. The therapeutic response achieved with the delivery of a low activity is due to the high linear energy transfer (LET) of the alpha particles emitted by actinium-225 [166].

Altogether, the IT injection of radiolabeled AuNPs in xenograft tumor-bearing mouse models show their potential to treat localized cancers. Importantly, next to the development of a less invasive treatment procedure, AuNPs can interact with the radiation originating from radionuclides, enhancing the dose deposition, which can increase the efficacy of the nanobrachytherapy compared to conventional brachytherapy. Indeed, the next paragraphs gives an overview of the studies demonstrating that AuNPs increase the dose deposition of radionuclides during brachytherapy.

**Fig. 11.** Nanobrachytherapy, locally injecting radioactive AuNPs in the tumor, compared to brachytherapy, transplanting radioactive seeds in the tumor in close proximity to non-radioactive AuNPs. (A) SPECT/CT images of CD-1 athymic mice bearing MDA-MB-468 human breast cancer xenografts (white arrows) acquired 1 h or 48 h after IT injection of [$^{177}$Lu]Lu-AuNP-Panitumumab or [$^{177}$Lu]Lu-AuNP. (B) Tumor growth index (values shown represent mean ± SD) and (C) the percentage of survival over time for MDA-MB-468 tumor-bearing mice treated with 4.5 MBq of [$^{177}$Lu]Lu-AuNP-Panitumumab, [$^{177}$Lu]Lu-AuNP, unlabeled AuNP-Panitumumab, [$^{177}$Lu]Lu-DOTA-PEG-OPSS (not conjugated to AuNP) or normal saline. A-C were originally published in [157][11]. (D) SPECT/CT imaging acquired 0d, 1d, 2d, 4d, 7d, 14d, 21d and 35d post-IT injection of 1.51 mCi [$^{103}$Pd]Pd@Au nanoseeds in PC3-tumor bearing SCID mice. White arrows indicate tumors. (E) [$^{18}$F]FDG-PET/CT images acquired at 0d, 7d, 21d and 35d post-IT injection of PBS (lower panel), non-radioactive Pd@Au nanoseeds (middle panel) and [$^{103}$Pd]Pd@Au nanoseeds (upper panel). A significant tumor FDG uptake reduction was observed in the mice treated with [$^{103}$Pd]Pd@Au nanoseeds as compared to the FDG uptake of the mice treated with PBS or non-radioactive Pd@Au nanoseeds. White arrows indicate tumor sites. D-E are adapted from [165][12]. (F) Bioluminescence images of SW1990 pancreatic tumor-bearing mice acquired various days after treatment. The treatments are injection of PBS, brachytherapy using iodine-125 seed implantation (BT), injection of AuNPs (biodegradable honeycomb-like gold nanoparticles) + BT, injection of AuNPs + photothermal therapy (PTT), and injection of AuNPs + PTT + BT. (G) Relative tumor volume of mice 16 days after treatment with PBS, BT, AuNPs + BT, AuNPs + PTT, or AuNPs + PTT + BT. Insets: corresponding digital pictures of tumor post treatments. Scale bars are 1 cm. F-G are adapted from [192][13]. [11]Fig. 11 A-C were originally published in JNM. S. Yook, Z. Cai, Y. Lu, M. A. Winnik, J. P. Pignol and R. M. Reilly. Intratumorally Injected 177Lu-Labeled Gold Nanoparticles: Gold Nanoseed Brachytherapy with Application for Neoadjuvant Treatment of Locally Advanced Breast Cancer. J Nucl Med. 2016; Vol. 57 Issue 6: Pages 936–42. https://jnm.snmjournals.org/content/57/6/936. © SNMMI. [12]Fig. 11 D-E are adapted from S. Moeendarbari, R. Tekade, A. Mulgaonkar, P. Christensen, S. Ramezani, G. Hassan, et al., Theranostic Nanoseeds for Efficacious Internal Radiation Therapy of Unresectable Solid Tumors, Sci Rep, Vol. 6, 20614, https://www.nature.com/articles/srep20614, Open access article distributed under the terms of the Creative Commons BY 4.0 license (https://creativecommons.org/licenses/by/4.0/). Copyright (2016) The Author(s). No changes were made to the images. [13]Fig. 11 F-G are adapted from F. Zhang, X. Han, Y. Hu, S. Wang, S. Liu, X. Pan, et al., Interventional Photothermal Therapy Enhanced Brachytherapy: A New Strategy to Fight Deep Pancreatic Cancer, Advanced science, Vol. 6 Issue 5, 1801507, https://onlinelibrary.wiley.com/doi/full/10.1002/advs.201801507, Open access article distributed under the terms of the Creative Commons BY 4.0 license (https://creativecommons.org/licenses/by/4.0/). Copyright (2019) the author(s). No changes were made to the images.

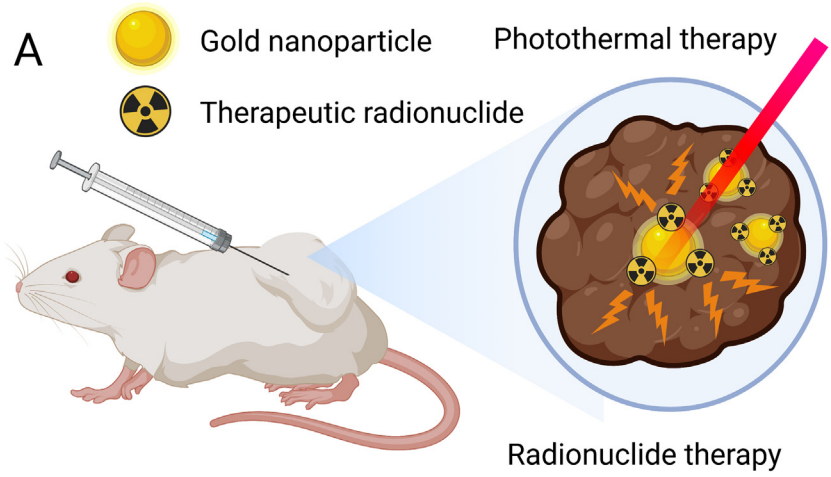
A
Gold nanoparticle
Therapeutic radionuclide
Photothermal therapy
Radionuclide therapy

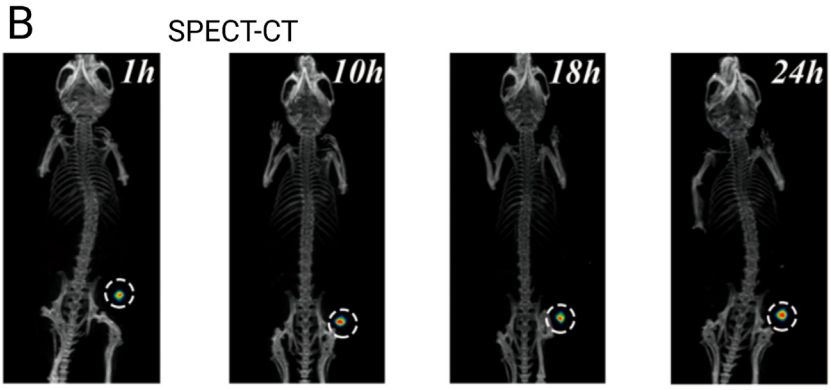
B
SPECT-CT
1h
10h
18h
24h

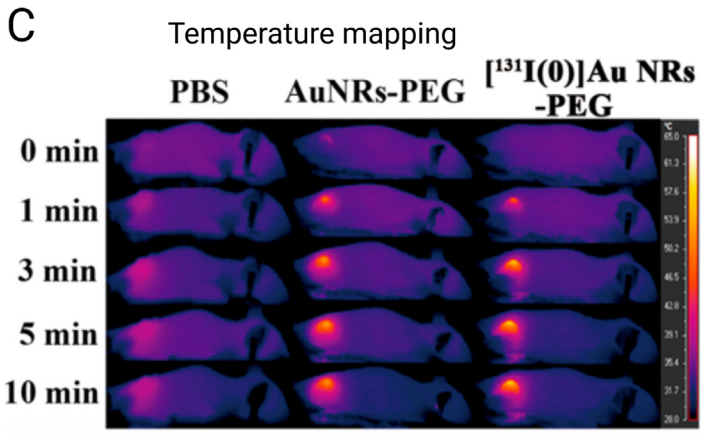
C
Temperature mapping
PBS
AuNRs-PEG
[131I(0)]Au NRs -PEG
0 min
1 min
3 min
5 min
10 min

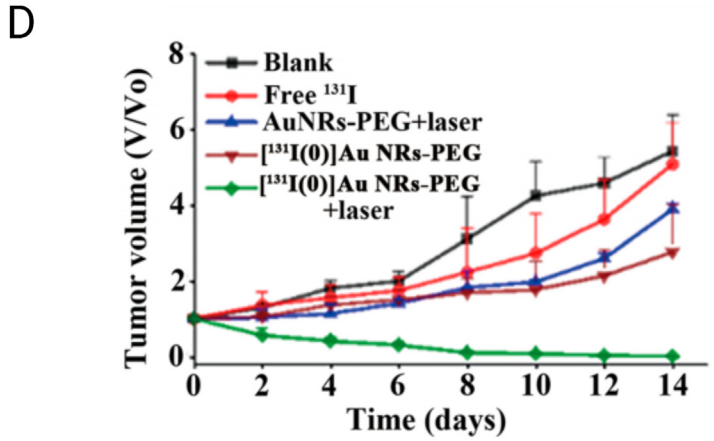
D
Blank
Free 131I
AuNRs-PEG+laser
[131I(0)]Au NRs-PEG
[131I(0)]Au NRs-PEG +laser
Tumor volume (V/Vo)
Time (days)
0
2
4
6
8
10
12
14

*3.3.4. Theoretical estimation of the dose enhancement of non-radiolabeled gold nanoparticles during brachytherapy*

Dose enhancement mediated by AuNPs has been well established for external X-ray irradiation as discussed in Section 1.3.2 of the Introduction. Similarly, multiple Monte Carlo simulations demonstrate dose enhancement when AuNPs are introduced in a tumor phantom region in close proximity to a radionuclide source or seeds. The most commonly studied radionuclides for brachytherapy purposes are the low-dose rate emitting iodine-125, palladium-103 and cesium-131, and the high-dose rate emitting ytterbium-169, iridium-192 and gold-198. The dose enhancement factor (DEF) is calculated as the ratio of the dose in the tumor or tissue region with and without the presence of AuNPs. The DEF strongly depends on the radiation source energy, the AuNP concentration in the tumor, the AuNPs distribution in the phantom, and the AuNP size. First, as shown in Supplementary Table 1, a higher DEF is reached as the AuNP concentration in the tumor increases [168–180]. In addition, higher DEF values are especially obtained for the low-energy emitting radionuclides palladium-103 (21 keV) and iodine-125 (29 keV), compared to the high energy emitting radionuclides ytterbium-169 (92.7 keV) and iridium-192 (354 keV). These results are attributed to the stronger and more important photoelectric absorption of AuNPs after interaction with low energy photons, causing a dose enhancement by the release of photoelectrons, Auger electrons and characteristic X-rays [170–175,178,180–182]. As a result, the calculated DEF increases with an increasing distance from the high-energy radioactive source, because of the shift in the emission spectra towards lower energies [169,174,182]. Although the photoelectric absorption is most efficient and abundant when using energies below the K-edge of gold (80.7 keV, the binding energy of the innermost and most strongly bound electrons), the emitted secondary electrons have a low energy and a high LET. Therefore, their traveling range is short (<100 μm), while the microscopic DEF in the area closely surrounding the AuNP is high, >80 [183]. Due to the limited travel range of the low-energy, high-LET electrons, small-sized AuNPs are required to minimize the internal absorption of the secondary electrons inside the nanoparticles and internalization of the AuNPs is necessary to cause cell damage. On the other hand, for high-energy photon sources, the energy of the released photoelectrons is higher, but their LET is lower. Therefore, the electrons can cross-fire across multiple cells. As a result, higher concentrations of AuNPs are required to increase the dose enhancement, while AuNP size and cellular localization are less relevant [181,183].

Importantly, multiple studies demonstrate that the presence of AuNPs not only increases the dose inside the tumor, but also shields healthy tissue from low-dose irradiation and thus decreases the dose delivery outside the tumor region, compared to brachytherapy without AuNPs [168–170,172,174,176,179,182,184–186]. For instance, Brivio, et al. studied the dose enhancement effects caused by a uniform and non-uniform distribution of AuNPs during prostate cancer brachytherapy with $^{125}$I-seeds [186]. More specifically, they compared the DEFs when the AuNPs were uniformly distributed in the prostate volume, confined at the seeds or located in between the seeds. Positioning the AuNPs between the seeds is the most beneficial scenario, since it causes a dose enhancement in the whole prostate. Importantly, the study highlighted that in all three distribution patterns, the urethra and rectum are spared and receive only 1/3 of the standard brachytherapy dose without AuNPs. This radiation attenuation effect observed in the healthy tissues is attributed to the high-Z AuNPs, which absorb the radionuclide X-rays and emit low-energy electrons. These low-energy electrons are in turn rapidly stopped within the nano- or micrometer range from the AuNPs [186]. Overall, the Monte Carlo simulations show that AuNPs might be a promising tool to increase the therapeutic ratio of brachytherapy and spare the surrounding healthy tissues.

In order to confirm and validate Monte Carlo simulation results, Khosravi, et al. embedded 15 nm AuNPs in a polymeric gel (Magic-f) that was located in the prostate region of a plexiglas pelvic phantom. The authors performed dosimetric measurements after irradiation of the gel using $^{192}$Ir-brachytherapy sources [187] The experimental results showed a DEF of 1.14 when AuNPs were present in the gel, which was in good agreement with the DEF estimated by the MCNP5 Monte Carlo calculation [187].

*3.3.5. In vitro and in vivo radiosensitization of non-radiolabeled AuNPs during brachytherapy*

The numerous simulation studies described above are supported by several experimental *in vitro* and *in vivo* studies. For instance, Shahhoseini, et al. inserted $^{192}$Ir-sources and electronic brachytherapy sources (eBx®) generating low-energy 50 kV X-rays into applicator ducts built under a 6-well plate. The wells were seeded with A549 lung cancer cells or Du145 prostate cancer cells, which were exposed to 1 mM AuNPs (15 nm) for 24 h before irradiation. According to colony forming unit assays, pre-exposure of cells to AuNPs caused DEFs of 1.54 and 2.06 for A549 cells and of 1.64 and 2.90 for Du145 cells after irradiation with iridium-192 and eBx, respectively. This *in vitro* study confirms the results of the theoretical studies demonstrating that higher DEF values are reached with low-energy emitting brachytherapy sources [188]. Furthermore, γH2AX staining shows that HeLa cells incubated with 0.2 mg/ml of 50 nm AuNPs and irradiated with a $^{125}$I-seeds plaque exhibit more unrepaired DNA damage after 24 h, with a DEF value ranging from 1.7 to 2.3, compared to irradiated cells without AuNPs [189]. In line with these results, 1 h after irradiation with an erbium filtered 250 kVp beam mimicking the photon radiation spectrum of ytterbium-169, goserelin-conjugated gold nanorods (gAuNRs) induce significantly more γH2AX foci in prostate cancer cells that overexpress the gonadotropin releasing hormone (GnRH) receptor compared to the irradiated control cells and irradiated cells exposed to untargeted AuNPs. Moreover, the growth rate of PC3 prostate cancer xenografts is significantly reduced over a period of 70 days when treated with IV injected gAuNRs and irradiated with the erbium filtered X-ray beam, compared to irradiation alone (a tumor volume of 1.87 $cm^3$ vs 4.01 $cm^3$, respectively) [190]. Similarly, a 2 h-incubation of Na/I symporter-expressing B16F10 melanoma cells or DHD/K12/TRb colorectal cancer cells with 25 μg/ml of polymer grafted-AuNPs significantly sensitizes the cells to $^{131}$I-exposure (0.1–0.2 MBq). Furthermore, the combination of IT injected polymer-grafted AuNPs and IP $^{131}$I-treatment attenuated the tumor growth of xenografted melanoma cells by 34% over $^{131}$I-treatment alone [191]. Finally, a small (but non-significant) decrease of the SW1990 pancreatic xenograft volume was observed 16 days after treatment with IV injected AuNPs and $^{125}$I-seed implantation, compared to $^{125}$I-brachytherapy alone (Fig. 11 F-G) [192].

*3.3.6. Radiosensitization mechanism of radiolabeled gold nanoparticles*

As described by the theoretical, *in vitro* and *in vivo* studies above, AuNPs are promising tools to enhance the dose deposition of radionu-

**Fig. 12.** Combination therapy. (A) The specific characteristics of radiolabeled AuNPs enable the combination of different treatments. IT administration of radiolabeled AuNPs deliver a therapeutic radiation dose to the tumor, while the surface plasmon resonance of the AuNPs enables photothermal therapy, increasing the tumor temperature (B) SPECT/CT imaging of MCF-7 tumor-bearing mice acquired 1 h, 10 h, 18 h and 24 h after IT injection of [$^{131}$I]I(0)-AuNRs-PEG. (C) Thermal imaging of MCF-7 tumor bearing mice after IT injection of PBS, AuNRs-PEG, or [$^{131}$I]I(0)-AuNRs-PEG. (D) Tumor growth rate after treatment with PBS, free Na[$^{131}$*I*]I, AuNRs-PEG + laser, [$^{131}$I]I(0)-AuNRs-PEG, [$^{131}$I]I(0)-AuNRs-PEG + laser. Tumor volumes were normalized to their initial size. The error bars represent the standard deviation of 5 mice per group. Compared with free Na[$^{131}$*I*]I, [$^{131}$I]I(0)-AuNRs-PEG inhibited the tumor growth more effectively. Upon 808 nm laser irritation (0.5 $W \cdot cm^{-2}$), the tumor temperature of the tumor injected with AuNRs-PEG or [$^{131}$I]I(0)-AuNRs-PEG increased to 50 °C within 2 min and the tumor growth delayed greatly. When combining the radionuclide therapy with photothermal therapy using [$^{131}$I]I(0)-AuNRs-PEG, the tumor growth is completely suppressed and the mice survival time greatly increases. Adapted from [97][14]. [14]Fig. 12 B-D are adapted with permission from ACS Applied Nano Materials, Vol. 2 Issue 3, *P. Wang*, W. Sun, Q. Wang, J. Ma, X. Su, Q. Jiang, et al., Iodine-Labeled Au Nanorods with High Radiochemical Stability for Imaging-Guided Radiotherapy and Photothermal Therapy, Pages 1374–1381. Copyright (2019) American Chemical Society.

clides. However, these studies were conducted using non-radioactive AuNPs that were placed in the vicinity of radioactive seeds. This approach would still require the invasive implantation of the radioactive seeds as explained before. Therefore, Laprisse, et al. studied the macroscopic and microscopic dose enhancement of $^{103}$Pd-radiolabeled AuNPs that were injected in prostate cancer xenografts [167]. Macroscopically, the radiolabeled AuNPs exhibit a smaller area of energy deposition compared to the conventional brachytherapeutic seeds due to the attenuation of the $^{103}$Pd-photons by the AuNP cloud. This attenuation effect could increase treatment precision and reduce dose deposition in healthy tissue. In their microdosimetric approach, the authors used TEM imaging to take into account the specific intracellular biological structures and well as the strong agglomeration of the radiolabeled AuNPs inside intracellular vesicles and their heterogeneous distribution in the tumor cells. In the very close vicinity of the AuNPs, the presence of gold enhances the dose deposition with a DEF of 25, compared to $^{103}$Pd-cores without AuNPs. There is a sharp fall-off of the DEF with an increasing distance, which reduces to 1 when the distance from the AuNPs reaches 2 μm. Importantly, since the radiolabeled AuNPs are strongly accumulated inside intracellular vesicles, there was no strong dose enhancement (DEF = 1) found in the cell nuclei. Nevertheless, IT injection of the [$^{103}$Pd]Pd@AuNPs-PEG showed strong tumor volume control [127]. Therefore, besides the physical dose enhancement, indirect damage via ROS production and the biological radiosensitization, which is discussed in detail in the introduction are potential leading mechanisms of the radiolabeled AuNPs to increase the therapeutic efficacy of radionuclide therapy.

Although IT injection of radiolabeled AuNPs show promising experimental results *in vivo*, from a clinical point of view, the use of radiolabeled AuNPs as an alternative for brachytherapy seeds remains challenging. In order to treat a human tumor, which is much larger than an *in vivo* xenograft, multiple IT injections of radiolabeled AuNPs in the tumor are required. These IT injections need to be spatially distributed with a high accuracy to minimize dose deposition heterogeneities in the tumor [193]. Therefore, Lai, et al. supports the implantation of nanoparticle release devices, which are loaded with a high concentration of radiolabeled AuNPs that are released into the surrounding tumor tissue. The authors describe this as an intermediate option combining the precise positioning using conventional seed implantation techniques and the advantage of homogenizing the dose deposition through the sustained delivery and diffusion of radiolabeled AuNPs out of the device [194]. Previous studies showed that during iodine-125 irradiation, the DEF at a close distance from the nanoparticle release device (5 mm) increases in function of time, due to the continuous AuNPs released from the device. Furthermore, the use of small-sized AuNPs (2–5 nm) results in higher DEFs due to their high release rate and homogeneous diffusion rate, compared to larger AuNPs (>15 nm) [193,195]. Lai, et al. studied the dose distribution of AuNPs labeled with lutetium-177, yttrium-90 and indium-111 from nanoparticle release devices or IT injected. The higher electron emitter yttrium-90 resulted in a greater penetration and delivered a more homogeneous dose distribution than the lower energy electron emitters lutetium-177 and indium-111. Furthermore, the dose distribution of radiolabeled AuNPs originating from a nanoparticle release device implanted in a tumor xenograft *in vivo* remains concentric around the device, while IT injection of the radiolabeled AuNPs results in irregularly shaped dose distribution, which are difficult to predict over time. Therefore, the authors highlighted the potential of the nanoparticle release device to improve the conventional brachytherapy strategies by providing a more predictable and homogeneous dose distribution to the tumor [194].

## 4. Conclusions and perspectives

In this review, we gave an overview on the radiolabeling processes of AuNPs and the potential of radiolabeled AuNPs to improve current nuclear imaging and therapy, taking into account the administration method, the biodistribution profile, tumor uptake, intratumoral distribution and tumor retention. We highlighted that targeted, radiolabeled AuNPs enhance the tumor uptake and retention, causing a better tumor control compared to their radiopharmaceutical analogs without AuNPs. Furthermore, radiolabeled AuNPs enable the use of multimodal imaging platforms for the visualization of their maximal tumor uptake to initiate photothermal therapy, to increase the effectiveness of external beam radiotherapy, or to define sentinel lymph nodes.

A large majority of the radiolabeled AuNPs that are administered systemically cause a sub-optimal biodistribution with a high and prolonged accumulation in non-targeted healthy tissues, such as in the liver, spleen and kidneys, which can result in an adverse dosimetric profile. In order to avoid the strong sequestration of the AuNPs by the RES, radiolabeled AuNPs as therapeutic agents are usually assessed after IT injection. This shifted our focus to the use of AuNPs in nanobrachytherapy. It is well established by numerous Monte Carlo simulations and experimental studies that non-radioactive AuNPs enhance the dose deposition of conventional brachytherapy seeds and reduces the dose deposition in healthy tissue due to the radiation absorption. However, the number of studies focusing on the dose enhancement using radiolabeled AuNPs, despite their ability to control tumor growth, remains limited. Furthermore, we want to point out that in many experimental dose enhancement studies, the interaction between high-Z AuNPs and the radionuclide radiation is often the only mechanism stated for the increased effectiveness of the (brachy)radiotherapy. This despite the numerous studies showing that AuNPs also have biological effects in cancer cells. Indeed, exposure of cancer cells to AuNPs alone can cause mitochondrial dysfunction, oxidative stress, increased DNA damage, lysosomal dysfunction, etc. These biological effects alone may not be lethal to the cancer cells, but certainly can increase the radiation sensitivity of the cancer cells and thus sensitize the cells to the radionuclide therapy. The dose enhancement studies discussed in this review often conclude that low-dose radionuclides are a good choice to achieve a strong dose enhancement from the AuNPs. However, the biological radiosensitization of the AuNPs should not be underestimated and thus could be a valuable reason to explore the use of AuNPs radiolabeled with high-energy radionuclides to improve targeted radionuclide therapy. The intratumoral delivery of radiolabeled AuNPs is less useful for the detection and imaging of cancer cells. However, besides the delivery of radionuclides, radiolabeled AuNPs also have the potential to carry chemotherapeutic drugs, mediate photothermal ablation and radiosensitize cancer cells, which makes them valuable tools to overcome radioresistance and/or chemoresistance cancer cells.

Supplementary data to this article can be found online at https://doi.org/10.1016/j.nucmedbio.2021.06.001.

## Declaration of competing interest

The authors declare no conflict of interests.

## Acknowledgements

We would like to thank Dr. Karen Van Hoecke for her support and the proofreading of this review. The review was inspired and derived from the PhD project of N.Daems who was financially supported by the Fonds de la Recherche Scientifique-FNRS (FRIA). Figs. 7-12 are created with BioRender.com.

## References

[1] Bhattacharyya S, Dixit M. Metallic radionuclides in the development of diagnostic and therapeutic radiopharmaceuticals. Dalton Trans. 2011;40:6112–28.
[2] Kraeber-Bodere F, Barbet J. Challenges in nuclear medicine: innovative theranostic tools for personalized medicine. Front Med. 2014;1:16.
[3] Czernin J, Sonni I, Razmaria A, Calais J. The future of nuclear medicine as an independent specialty. J Nucl Med. 2019;60:3S–12S.

[4] Herrmann K, Schwaiger M, Lewis JS, Solomon SB, McNeil BJ, Baumann M, et al. Radiotheranostics: a roadmap for future development. Lancet Oncol. 2020;21 (e146-e56).
[5] Terry SYA, Nonnekens J, Aerts A, Baatout S, de Jong M, Cornelissen B, et al. Call to arms: need for radiobiology in molecular radionuclide therapy. Eur J Nucl Med Mol Imaging. 2019;46:1588–90.
[6] Pothukuchi S, Li Y, Wong CP. Formulation of different shapes of nanoparticles and their incorporation into polymers. 9th International Symposium on Advanced Packaging Materials: Processes, Properties and Interfaces; 2004. p. 200–3.
[7] Lucas S, Feron O, Gallez B, Masereel B, Michiels C, Vander Borght T. Monte Carlo calculation of radioimmunotherapy with (90)Y-, (177)Lu-, (131)I-, (124)I-, and (188) Re-Nanoobjects: choice of the best radionuclide for solid tumour treatment by using TCP and NTCP concepts. Comput Math Methods Med. 2015;2015:284360.
[8] Sztandera K, Gorzkiewicz M, Klajnert-Maculewicz B. Gold nanoparticles in cancer treatment. Mol Pharm. 2019;16:1–23.
[9] Bertrand N, Wu J, Xu X, Kamaly N, Farokhzad OC. Cancer nanotechnology: the impact of passive and active targeting in the era of modern cancer biology. Adv Drug Deliv Rev. 2014;66:2–25.
[10] Nichols JW, Bae YH. EPR: evidence and fallacy. J Control Release. 2014;190:451–64.
[11] Nel A, Ruoslahti E, Meng H. New insights into "permeability" as in the enhanced permeability and retention effect of cancer nanotherapeutics. ACS Nano. 2017;11: 9567–9.
[12] Danhier F. To exploit the tumor microenvironment: since the EPR effect fails in the clinic, what is the future of nanomedicine? J Control Release. 2016;244:108–21.
[13] Wilhelm S, Tavares AJ, Dai Q, Ohta S, Audet J, Dvorak HF, et al. Analysis of nanoparticle delivery to tumours. Nat Rev Mater. 2016;1:16014.
[14] Sindhwani S, Syed AM, Ngai J, Kingston BR, Maiorino L, Rothschild J, et al. The entry of nanoparticles into solid tumours. Nat Mater. 2020;19:566–75.
[15] Bouchat V, Nuttens VE, Michiels C, Masereel B, Feron O, Gallez B, et al. Radioimmunotherapy with radioactive nanoparticles: biological doses and treatment efficiency for vascularized tumors with or without a central hypoxic area. Med Phys. 2010;37:1826–39.
[16] Bouchat V, Nuttens VE, Lucas S, Michiels C, Masereel B, Feron O, et al. Radioimmunotherapy with radioactive nanoparticles: first results of dosimetry for vascularized and necrosed solid tumors. Med Phys. 2007;34:4504–13.
[17] Zhong D, Zhao J, Li Y, Qiao Y, Wei Q, He J, et al. Laser-triggered aggregated cubic alpha-Fe2O3@Au nanocomposites for magnetic resonance imaging and photothermal/enhanced radiation synergistic therapy. Biomaterials. 2019;219: 119369.
[18] Singh P, Pandit S, Mokkapati V, Garg A, Ravikumar V, Mijakovic I. Gold nanoparticles in diagnostics and therapeutics for human cancer. Int J Mol Sci. 2018;19:1979.
[19] Vines JB, Yoon JH, Ryu NE, Lim DJ, Park H. Gold nanoparticles for photothermal cancer therapy. Front Chem. 2019;7:167.
[20] Yang W, Liang H, Ma S, Wang D, Huang J. Gold nanoparticle based photothermal therapy: development and application for effective cancer treatment. Sustain Mater Technol. 2019;22:e00109.
[21] Stabile J, Najafali D, Cheema Y, Inglut CT, Liang BJ, Vaja S, et al. Chapter 12 - engineering gold nanoparticles for photothermal therapy, surgery, and imaging. In: Chung EJ, Leon L, Rinaldi C, editors. Nanoparticles for biomedical applications. Elsevier; 2020. p. 175–93.
[22] Wang S, Fu L, Xin J, Wang S, Yao C, Zhang Z, et al. Photoacoustic response induced by nanoparticle-mediated photothermal bubbles beyond the thermal expansion for potential theranostics. J Biomed Opt. 2018;23:125002.
[23] Gao F, Bai L, Liu S, Zhang R, Zhang J, Feng X, et al. Rationally encapsulated gold nanorods improving both linear and nonlinear photoacoustic imaging contrast in vivo. Nanoscale. 2017;9:79–86.
[24] Huang X, El-Sayed MA. Gold nanoparticles: optical properties and implementations in cancer diagnosis and photothermal therapy. J Adv Res. 2010;1:13–28.
[25] Li M, Qiu Y, Fan C, Cui K, Zhang Y, Xiao Z. Design of SERS nanoprobes for Raman imaging: materials, critical factors and architectures. Acta Pharm Sin B. 2018;8:381–9.
[26] Hainfeld JF, Slatkin DN, Focella TM, Smilowitz HM. Gold nanoparticles: a new X-ray contrast agent. Br J Radiol. 2006;79:248–53.
[27] Hainfeld JF, Dilmanian FA, Slatkin DN, Smilowitz HM. Radiotherapy enhancement with gold nanoparticles. J Pharm Pharmacol. 2008;60:977–85.
[28] Daems N, Penninckx S, Nelissen I, Van Hoecke K, Cardinaels T, Baatout S, et al. Gold nanoparticles affect the antioxidant status in selected normal human cells. Int J Nanomedicine. 2019;14:4991–5015.
[29] Penninckx S, Heuskin AC, Michiels C, Lucas S. The role of thioredoxin reductase in gold nanoparticle radiosensitization effects. Nanomedicine. 2018;13:2917–37.
[30] Penninckx S, Heuskin AC, Michiels C, Lucas S. Thioredoxin reductase activity predicts gold nanoparticle radiosensitization effect. Nanomaterials. 2019;9:295.
[31] Sabella S, Carney RP, Brunetti V, Malvindi MA, Al-Juffali N, Vecchio G, et al. A general mechanism for intracellular toxicity of metal-containing nanoparticles. Nanoscale. 2014;6:7052–61.
[32] Ramalingam V, Revathidevi S, Shanmuganayagam TS, Muthulakshmi L, Rajaram R. Gold nanoparticle induces mitochondria-mediated apoptosis and cell cycle arrest in nonsmall cell lung cancer cells. Gold Bull. 2017;50:177–89.
[33] Pan Y, Leifert A, Ruau D, Neuss S, Bornemann J, Schmid G, et al. Gold nanoparticles of diameter 1.4 nm trigger necrosis by oxidative stress and mitochondrial damage. Small. 2009;5:2067–76.
[34] Zhang F, Zhu X, Gong J, Sun Y, Chen D, Wang J, et al. Lysosome-mitochondria-mediated apoptosis specifically evoked in cancer cells induced by gold nanorods. Nanomedicine. 2016;11:1993–2006.
[35] Mateo D, Morales P, Avalos A, Haza AI. Oxidative stress contributes to gold nanoparticle-induced cytotoxicity in human tumor cells. Toxicol Mech Methods. 2014;24:161–72.
[36] Taggart LE, McMahon SJ, Currell FJ, Prise KM, Butterworth KT. The role of mitochondrial function in gold nanoparticle mediated radiosensitisation. Cancer Nanotechnol. 2014;5:5.
[37] Ma N, Liu P, He N, Gu N, Wu FG, Chen Z. Action of gold Nanospikes-based nanoradiosensitizers: cellular internalization, radiotherapy, and autophagy. ACS Appl Mater Interfaces. 2017;9:31526–42.
[38] Manshian BB, Pokhrel S, Madler L, Soenen SJ. The impact of nanoparticle-driven lysosomal alkalinization on cellular functionality. J Nanobiotechnol. 2018;16:85.
[39] Ma X, Wu Y, Jin S, Tian Y, Zhang X, Zhao Y, et al. Gold nanoparticles induce autophagosome accumulation through size-dependent nanoparticle uptake and lysosome impairment. ACS Nano. 2011;5:8629–39.
[40] Abdel-Ghany S, Mahfouz M, Ashraf N, Sabit H, Cevik E, El-Zawahri M. Gold nanoparticles induce G2/M cell cycle arrest and enhance the expression of E-cadherin in breast cancer cells. Inorg Nano-Metal Chem. 2020;50:926–32.
[41] Butterworth KT, Coulter JA, Jain S, Forker J, McMahon SJ, Schettino G, et al. Evaluation of cytotoxicity and radiation enhancement using 1.9 nm gold particles: potential application for cancer therapy. Nanotechnology. 2010;21:295101.
[42] Martinez-Torres AC, Lorenzo-Anota HY, Garcia-Juarez MG, Zarate-Trivino DG, Rodriguez-Padilla C. Chitosan gold nanoparticles induce different ROS-dependent cell death modalities in leukemic cells. Int J Nanomedicine. 2019;14:7173–90.
[43] Alamzadeh Z, Beik J, Mirrahimi M, Shakeri-Zadeh A, Ebrahimi F, Komeili A, et al. Gold nanoparticles promote a multimodal synergistic cancer therapy strategy by co-delivery of thermo-chemo-radio therapy. Eur J Pharm Sci. 2020;145:105235.
[44] Association WN. Radioisotopes in Medicine; 2021.
[45] Jeon J. Review of therapeutic applications of radiolabeled functional nanomaterials. Int J Mol Sci. 2019;20:2323.
[46] Famulari G, Pater P, Enger S. Microdosimetric evaluation of current and alternative brachytherapy sources - a Geant4-DNA simulation study. Int J Radiat Oncol Biol Phys. 2017;100:270–7.
[47] Boros E, Holland J. Chemical aspects of metal ion chelation in the synthesis and application antibody-based radiotracers. J Label Compd Radiopharm. 2017;61: 652–71.
[48] Abdel-Aty A-H, Hassan HE, Hassan K, Khalaf A, Saleh Z. Cross sections for the formation of radioiodines in proton bombardment of natural tellerium with particular reference to the validation of data for the production of 123I. Radiochim Acta. 2011;99:317–23.
[49] Vilchis-Juarez A, Ferro-Flores G, Santos-Cuevas C, Morales-Avila E, Ocampo-Garcia B, Diaz-Nieto L, et al. Molecular targeting radiotherapy with cyclo-RGDFK (C) peptides conjugated to 177Lu-labeled gold nanoparticles in tumor-bearing mice. J Biomed Nanotechnol. 2014;10:393–404.
[50] Jimenez-Mancilla N, Ferro-Flores G, Santos-Cuevas C, Ocampo-Garcia B, Luna-Gutierrez M, Azorin-Vega E, et al. Multifunctional targeted therapy system based on (99m) Tc/(177) Lu-labeled gold nanoparticles-Tat(49-57)-Lys(3) -bombesin internalized in nuclei of prostate cancer cells. J Labelled Comp Radiopharm. 2013;56: 663–71.
[51] Morales-Avila E, Ferro-Flores G, Ocampo-Garcia BE, De Leon-Rodriguez LM, Santos-Cuevas CL, Garcia-Becerra R, et al. Multimeric system of 99mTc-labeled gold nanoparticles conjugated to c[RGDfK(C)] for molecular imaging of tumor alpha(v)beta (3) expression. Bioconjug Chem. 2011;22:913–22.
[52] Ocampo-Garcia BE, Ramirez Fde M, Ferro-Flores G, De Leon-Rodriguez LM, Santos-Cuevas CL, Morales-Avila E, et al. (99m)Tc-labelled gold nanoparticles capped with HYNIC-peptide/mannose for sentinel lymph node detection. Nucl Med Biol. 2011; 38:1–11.
[53] Byegård J, Skarnemark G, Skålberg M. The stability of some metal EDTA, DTPA and DOTA complexes: application as tracers in groundwater studies. J Radioanal Nucl Chem. 1999;241:281–90.
[54] Pellico J, Gawne PJ, de Rosales R. TM. Radiolabelling of nanomaterials for medical imaging and therapy. Chem Soc Rev. 2021;50:3355–423.
[55] Coenen HH, Gee AD, Adam M, Antoni G, Cutler CS, Fujibayashi Y, et al. Consensus nomenclature rules for radiopharmaceutical chemistry — setting the record straight. Nucl Med Biol. 2017;55 (v-xi).
[56] Liu S. Bifunctional coupling agents for radiolabeling of biomolecules and target-specific delivery of metallic radionuclides. Adv Drug Deliv Rev. 2008;60:1347–70.
[57] Chen CC, Li JJ, Guo NH, Chang DY, Wang CY, Chen JT, et al. Evaluation of the biological behavior of a gold nanocore-encapsulated human serum albumin nanoparticle (Au@HSANP) in a CT-26 tumor/ascites mouse model after intravenous/intraperitoneal administration. Int J Mol Sci. 2019;20:217.
[58] Tam AL, Melancon MP, Abdelsalam M, Figueira TA, Dixon K, McWatters A, et al. Imaging Intratumoral nanoparticle uptake after combining nanoembolization with various ablative therapies in hepatic VX2 rabbit tumors. J Biomed Nanotechnol. 2016;12:296–307.
[59] Wang Y, Liu Y, Luehmann H, Xia X, Brown P, Jarreau C, et al. Evaluating the pharmacokinetics and in vivo cancer targeting capability of Au nanocages by positron emission tomography imaging. ACS Nano. 2012;6:5880–8.
[60] Song L, Falzone N, Vallis KA. EGF-coated gold nanoparticles provide an efficient nano-scale delivery system for the molecular radiotherapy of EGFR-positive cancer. Int J Radiat Biol. 2016;92:716–23.
[61] Yook S, Cai Z, Lu Y, Winnik MA, Pignol JP, Reilly RM. Radiation nanomedicine for EGFR-positive breast cancer: Panitumumab-modified gold nanoparticles complexed to the beta-particle-emitter, (177)Lu. Mol Pharm. 2015;12:3963–72.
[62] Xing Y, Zhu J, Zhao L, Xiong Z, Li Y, Wu S, et al. SPECT/CT imaging of chemotherapy-induced tumor apoptosis using (99m)Tc-labeled dendrimer-entrapped gold nanoparticles. Drug Deliv. 2018;25:1384–93.
[63] Zhao L, Wen S, Zhu M, Li D, Xing Y, Shen M, et al. 99mTc-labelled multifunctional polyethylenimine-entrapped gold nanoparticles for dual mode SPECT and CT imaging. Artif Cells Nanomed Biotechnol. 2018;46:488–98.

[64] Karmani L, Bouchat V, Bouzin C, Leveque P, Labar D, Bol A, et al. (89)Zr-labeled anti-endoglin antibody-targeted gold nanoparticles for imaging cancer: implications for future cancer therapy. Nanomedicine 2014;9:1923–37.
[65] Xu X, Zhao L, Li X, Wang P, Zhao J, Shi X, et al. Targeted tumor SPECT/CT dual mode imaging using multifunctional RGD-modified low generation dendrimer-entrapped gold nanoparticles. Biomater Sci. 2017;5:2393–7.
[66] Yang Y, Zhang L, Cai J, Li X, Cheng D, Su H, et al. Tumor angiogenesis targeted radiosensitization therapy using gold nanoprobes guided by MRI/SPECT imaging. ACS Appl Mater Interfaces. 2016;8:1718–32.
[67] Pretze M, van der Meulen NP, Wangler C, Schibli R, Wangler B. Targeted (64) Cu-labeled gold nanoparticles for dual imaging with positron emission tomography and optical imaging. J Labelled Comp Radiopharm. 2019;62:471–82.
[68] Zhao Y, Detering L, Sultan D, Cooper ML, You M, Cho S, et al. Gold nanoclusters doped with (64)Cu for CXCR4 positron emission tomography imaging of breast cancer and metastasis. ACS Nano. 2016;10:5959–70.
[69] Frellsen AF, Hansen AE, Jolck RI, Kempen PJ, Severin GW, Rasmussen PH, et al. Mouse positron emission tomography study of the biodistribution of gold nanoparticles with different surface coatings using embedded Copper-64. ACS Nano. 2016;10:9887–98.
[70] Zhao Y, Pang B, Luehmann H, Detering L, Yang X, Sultan D, et al. Gold nanoparticles doped with (199) Au atoms and their use for targeted cancer imaging by SPECT. Adv Healthc Mater. 2016;5:928–35.
[71] Zhao Y, Sultan D, Detering L, Cho S, Sun G, Pierce R, et al. Copper-64-alloyed gold nanoparticles for cancer imaging: improved radiolabel stability and diagnostic accuracy. Angew Chem. 2014;53:156–9.
[72] Sun X, Huang X, Yan X, Wang Y, Guo J, Jacobson O, et al. Chelator-free (64)Cu-integrated gold nanomaterials for positron emission tomography imaging guided photothermal cancer therapy. ACS Nano. 2014;8:8438–46.
[73] Rovais MRA, Alirezapour B, Moassesi ME, Amiri M, Novin FB, Maadi E. Internalization capabilities of gold-198 nanoparticles: comparative evaluation of effects of chitosan agent on cellular uptake into MCF-7. Appl Radiat Isot. 2018;142:85–91.
[74] Black KC, Wang Y, Luehmann HP, Cai X, Xing W, Pang B, et al. Radioactive 198Au-doped nanostructures with different shapes for in vivo analyses of their biodistribution, tumor uptake, and intratumoral distribution. ACS Nano. 2014;8:4385–94.
[75] Zhao Y, Sultan D, Detering L, Luehmann H, Liu Y. Facile synthesis, pharmacokinetic and systemic clearance evaluation, and positron emission tomography cancer imaging of (6)(4)Cu-Au alloy nanoclusters. Nanoscale. 2014;6:13501–9.
[76] Wang Y, Liu Y, Luehmann H, Xia X, Wan D, Cutler C, et al. Radioluminescent gold nanocages with controlled radioactivity for real-time in vivo imaging. Nano Lett. 2013;13:581–5.
[77] Laprise-Pelletier M, Simao T, Fortin MA. Gold nanoparticles in radiotherapy and recent progress in nanobrachytherapy. Adv Healthc Mater. 2018;7:e1701460.
[78] Lee SB, Yoon G, Lee SW, Jeong SY, Ahn BC, Lim DK, et al. Combined positron emission tomography and Cerenkov luminescence imaging of sentinel lymph nodes using PEGylated radionuclide-embedded gold nanoparticles. Small. 2016;12:4894–901.
[79] Lee SB, Lee HW, Singh TD, Li Y, Kim SK, Cho SJ, et al. Visualization of macrophage recruitment to inflammation lesions using highly sensitive and stable radionuclide-embedded gold nanoparticles as a nuclear bio-imaging platform. Theranostics. 2017;7:926–34.
[80] Lee SB, Lee YJ, Cho SJ, Kim SK, Lee SW, Lee J, et al. Antigen-free radionuclide-embedded gold nanoparticles for dendritic cell maturation, tracking, and strong antitumor immunity. Adv Healthc Mater. 2018;7:e1701369.
[81] Sun N, Zhao L, Zhu J, Li Y, Song N, Xing Y, et al. (131)I-labeled polyethylenimine-entrapped gold nanoparticles for targeted tumor SPECT/CT imaging and radionuclide therapy. Int J Nanomedicine. 2019;14:4367–81.
[82] Black KCL, Akers WJ, Sudlow G, Xu B, Laforest R, Achilefu S. Dual-radiolabeled nanoparticle SPECT probes for bioimaging. Nanoscale. 2015;7:440–4.
[83] Su N, Dang Y, Liang G, Liu G. Iodine-125-labeled cRGD-gold nanoparticles as tumor-targeted radiosensitizer and imaging agent. Nanoscale Res Lett. 2015;10:160.
[84] Kao HW, Lin YY, Chen CC, Chi KH, Tien DC, Hsia CC, et al. Evaluation of EGFR-targeted radioimmuno-gold-nanoparticles as a theranostic agent in a tumor animal model. Bioorg Med Chem Lett. 2013;23:3180–5.
[85] Jeon J, Shim HE, Mushtaq S, Choi MH, Park SH, Choi DS, et al. An optimized protocol for the efficient radiolabeling of gold nanoparticles by using a 125I-labeled Azide Prosthetic Group. J Vis Exp. 2016(116):e54759.
[86] Guerrero S, Herance JR, Rojas S, Mena JF, Gispert JD, Acosta GA, et al. Synthesis and in vivo evaluation of the biodistribution of a 18F-labeled conjugate gold-nanoparticle-peptide with potential biomedical application. Bioconjug Chem. 2012;23:399–408.
[87] Ghiassian S, Yu L, Gobbo P, Nazemi A, Romagnoli T, Luo W, et al. Nitrone-modified gold nanoparticles: synthesis, characterization, and their potential as (18)F-labeled positron emission tomography probes via I-SPANC. ACS Omega. 2019;4:19106–15.
[88] Zhu J, Chin J, Wangler C, Wangler B, Lennox RB, Schirrmacher R. Rapid (18)F-labeling and loading of PEGylated gold nanoparticles for in vivo applications. Bioconjug Chem. 2014;25:1143–50.
[89] Lee SB, Lee SW, Jeong SY, Yoon G, Cho SJ, Kim SK, et al. Engineering of radioiodine-labeled gold core-shell nanoparticles as efficient nuclear medicine imaging agents for trafficking of dendritic cells. ACS Appl Mater Interfaces. 2017;9:8480–9.
[90] Lee SB, Kumar D, Li Y, Lee IK, Cho SJ, Kim SK, et al. PEGylated crushed gold shell-radiolabeled core nanoballs for in vivo tumor imaging with dual positron emission tomography and Cerenkov luminescent imaging. J Nanobiotechnol. 2018;16:41.
[91] Kim YH, Jeon J, Hong SH, Rhim WK, Lee YS, Youn H, et al. Tumor targeting and imaging using cyclic RGD-PEGylated gold nanoparticle probes with directly conjugated iodine-125. Small. 2011;7:2052–60.
[92] Zhang Y, Zhang Y, Yin L, Xia X, Hu F, Liu Q, et al. Synthesis and bioevaluation of Iodine-131 directly labeled cyclic RGD-PEGylated gold nanorods for tumor-targeted imaging. Contrast Media Mol Imaging. 2017;2017:6081724.
[93] Eskandari N, Yavari K, Outokesh M, Sadjadi S, Ahmadi SJ. Iodine-131 radiolabeling of poly ethylene glycol-coated gold nanorods for in vivo imaging. J Labelled Comp Radiopharm. 2013;56:12–6.
[94] Dziawer L, Koźmiński P, Męczyńska-Wielgosz S, Pruszyński M, Łyczko M, Wąs B, et al. Gold nanoparticle bioconjugates labelled with 211At for targeted alpha therapy. RSC Adv. 2017;7:41024–32.
[95] Dziawer L, Majkowska-Pilip A, Gawel D, Godlewska M, Pruszynski M, Jastrzebski J, et al. Trastuzumab-modified gold nanoparticles labeled with (211)At as a prospective tool for local treatment of HER2-positive breast cancer. Nanomaterials. 2019;9:632.
[96] Walsh AA. Chemisorption of iodine-125 to gold nanoparticles allows for real-time quantitation and potential use in nanomedicine. J Nanopart Res. 2017;19:152.
[97] Wang P, Sun W, Wang Q, Ma J, Su X, Jiang Q, et al. Iodine-labeled Au nanorods with high radiochemical stability for imaging-guided radiotherapy and photothermal therapy. ACS Appl Nano Mater. 2019;2:1374–81.
[98] Pretze M, Hien A, Radle M, Schirrmacher R, Wangler C, Wangler B. Gastrin-releasing peptide receptor- and prostate-specific membrane antigen-specific ultrasmall gold nanoparticles for characterization and diagnosis of prostate carcinoma via fluorescence imaging. Bioconjug Chem. 2018;29:1525–33.
[99] Zhang L, Su H, Wang H, Li Q, Li X, Zhou C, et al. Tumor chemo-radiotherapy with rod-shaped and spherical gold Nano probes: shape and active targeting both matter. Theranostics. 2019;9:1893–908.
[100] Mendoza-Nava H, Ferro-Flores G, Ramírez FdM, Ocampo-García B, Santos-Cuevas C, Aranda-Lara L, et al. $^{177}$Lu-Dendrimer conjugated to folate and bombesin with gold nanoparticles in the dendritic cavity: a potential theranostic radiopharmaceutical. J Nanomater. 2016;2016:1039258.
[101] Wang F, Li Y, Shen Y, Wang A, Wang S, Xie T. The functions and applications of RGD in tumor therapy and tissue engineering. Int J Mol Sci. 2013;14:13447–62.
[102] Peiris PM, Deb P, Doolittle E, Doron G, Goldberg A, Govender P, et al. Vascular targeting of a gold nanoparticle to breast cancer metastasis. J Pharm Sci. 2015;104:2600–10.
[103] Xie H, Wang ZJ, Bao A, Goins B, Phillips WT. In vivo PET imaging and biodistribution of radiolabeled gold nanoshells in rats with tumor xenografts. Int J Pharm. 2010;395:324–30.
[104] Mendoza-Sanchez AN, Ferro-Flores G, Ocampo-Garcia BE, Morales-Avila E, de MRF, De Leon-Rodriguez LM, et al.. Lys3-bombesin conjugated to 99mTc-labelled gold nanoparticles for in vivo gastrin releasing peptide-receptor imaging. J Biomed Nanotechnol. 2010;6:375–84.
[105] Yook S, Lu Y, Jeong JJ, Cai Z, Tong L, Alwarda R, et al. Stability and biodistribution of thiol-functionalized and (177)Lu-labeled metal chelating polymers bound to gold nanoparticles. Biomacromolecules. 2016;17:1292–302.
[106] Karmani L, Labar D, Valembois V, Bouchat V, Nagaswaran PG, Bol A, et al. Antibody-functionalized nanoparticles for imaging cancer: influence of conjugation to gold nanoparticles on the biodistribution of 89Zr-labeled cetuximab in mice. Contrast Media Mol Imaging. 2013;8:402–8.
[107] Orocio-Rodriguez E, Ferro-Flores G, Santos-Cuevas CL, Ramirez Fde M, Ocampo-Garcia BE, Azorin-Vega E, et al. Two novel nanosized radiolabeled analogues of somatostatin for neuroendocrine tumor imaging. J Nanosci Nanotechnol. 2015;15:4159–69.
[108] Poon W, Zhang YN, Ouyang B, Kingston BR, Wu JLY, Wilhelm S, et al. Elimination pathways of nanoparticles. ACS Nano. 2019;13:5785–98.
[109] Silva F, Zambre A, Campello MP, Gano L, Santos I, Ferraria AM, et al. Interrogating the role of receptor-mediated mechanisms: biological fate of peptide-functionalized radiolabeled gold nanoparticles in tumor mice. Bioconjug Chem. 2016;27:1153–64.
[110] Chattopadhyay N, Fonge H, Cai Z, Scollard D, Lechtman E, Done SJ, et al. Role of antibody-mediated tumor targeting and route of administration in nanoparticle tumor accumulation in vivo. Mol Pharm. 2012;9:2168–79.
[111] Xie H, Goins B, Bao A, Wang ZJ, Phillips WT. Effect of intratumoral administration on biodistribution of 64Cu-labeled nanoshells. Int J Nanomedicine. 2012;7:2227–38.
[112] Silva F, Paulo A, Pallier A, Meme S, Toth E, Gano L, et al. Dual imaging gold Nanoplatforms for targeted Radiotheranostics. Materials. 2020;13:513.
[113] Sakr TM, El-Hashash MA, El-Mohty AA, Essa BM. (99m)Tc-gallic-gold nanoparticles as a new imaging platform for tumor targeting. Appl Radiat Isot. 2020;164:109269.
[114] El-Ghareb WI, Swidan MM, Ibrahim IT, Abd El-Bary A, Tadros MI, Sakr TM. (99m)Tc-doxorubicin-loaded gallic acid-gold nanoparticles ((99m)Tc-DOX-loaded GA-Au NPs) as a multifunctional theranostic agent. Int J Pharm. 2020;586:119514.
[115] Chanda N, Kattumuri V, Shukla R, Zambre A, Katti K, Upendran A, et al. Bombesin functionalized gold nanoparticles show in vitro and in vivo cancer receptor specificity. Proc Natl Acad Sci U S A. 2010;107:8760–5.
[116] Kamal R, Chadha VD, Dhawan DK. Physiological uptake and retention of radiolabeled resveratrol loaded gold nanoparticles ((99m)Tc-Res-AuNP) in colon cancer tissue. Nanomedicine. 2018;14:1059–71.
[117] Zhang G, Yang Z, Lu W, Zhang R, Huang Q, Tian M, et al. Influence of anchoring ligands and particle size on the colloidal stability and in vivo biodistribution of polyethylene glycol-coated gold nanoparticles in tumor-xenografted mice. Biomaterials. 2009;30:1928–36.
[118] Song L, Able S, Johnson E, Vallis KA. Accumulation of (111)In-Labelled EGF-Au-PEG nanoparticles in EGFR-positive tumours is enhanced by coadministration of targeting ligand. Nanotheranostics. 2017;1:232–43.
[119] Azorín-Vega EP, Zambrano-Ramírez OD, Rojas-Calderón EL, Ocampo-García BE, Ferro-Flores G. Tumoral fibrosis effect on the radiation absorbed dose of 177Lu–

Tyr3-octreotate and 177Lu–Tyr3-octreotate conjugated to gold nanoparticles. Appl Radiat Isot. 2015;100:96–100.
[120] Melancon MP, Lu W, Yang Z, Zhang R, Cheng Z, Elliot AM, et al. In vitro and in vivo targeting of hollow gold nanoshells directed at epidermal growth factor receptor for photothermal ablation therapy. Mol Cancer Ther. 2008;7:1730–9.
[121] Chen CH, Lin FS, Liao WN, Liang SL, Chen MH, Chen YW, et al. Establishment of a trimodality analytical platform for tracing, imaging and quantification of gold nanoparticles in animals by radiotracer techniques. Anal Chem. 2015;87:601–8.
[122] Pang B, Zhao Y, Luehmann H, Yang X, Detering L, You M, et al. (6)(4)Cu-Doped PdCu@Au tripods: a multifunctional nanomaterial for positron emission tomography and image-guided photothermal cancer treatment. ACS Nano. 2016;10:3121–31.
[123] Le Goas M, Testard F, Taché O, Debou N, Cambien B, Carrot G, et al. How do surface properties of nanoparticles influence their diffusion in the extracellular matrix? A model study in Matrigel using polymer-grafted nanoparticles. Langmuir. 2020;36:10460–70.
[124] Le Goas M, Roussel T, Kalbazova M, Carriere D, Barruet E, Geertsen V, et al. Combining surface chemistry modification and in situ small-angle scattering characterization to understand and optimize the biological behavior of nanomedicines. J Mater Chem B. 2020;8:6438–50.
[125] Adams GP, Schier R, McCall AM, Simmons HH, Horak EM, Alpaugh RK, et al. High affinity restricts the localization and tumor penetration of single-chain fv antibody molecules. Cancer Res. 2001;61:4750–5.
[126] Tian M, Lu W, Zhang R, Xiong C, Ensor J, Nazario J, et al. Tumor uptake of hollow gold nanospheres after intravenous and intra-arterial injection: PET/CT study in a rabbit VX2 liver cancer model. Mol Imaging Biol. 2013;15:614–24.
[127] Laprise-Pelletier M, Lagueux J, Cote MF, LaGrange T, Fortin MA. Low-dose prostate cancer brachytherapy with radioactive palladium-gold nanoparticles. Adv Healthc Mater. 2017;6:1601120.
[128] Cormode DP, Naha PC, Fayad ZA. Nanoparticle contrast agents for computed tomography: a focus on micelles. Contrast Media Mol Imaging. 2014;9:37–52.
[129] Li J, You J, Wu C, Dai Y, Shi M, Dong L, et al. T1-T2 molecular magnetic resonance imaging of renal carcinoma cells based on nano-contrast agents. Int J Nanomedicine. 2018;13:4607–25.
[130] Elbialy NS, Fathy MM, Al-Wafi R, Darwesh R, Abdel-Dayem UA, Aldhahri M, et al. Multifunctional magnetic-gold nanoparticles for efficient combined targeted drug delivery and interstitial photothermal therapy. Int J Pharm. 2019;554:256–63.
[131] Abed Z, Beik J, Laurent S, Eslahi N, Khani T, Davani ES, et al. Iron oxide-gold core-shell nano-theranostic for magnetically targeted photothermal therapy under magnetic resonance imaging guidance. J Cancer Res Clin Oncol. 2019;145:1213–9.
[132] Yang M, Cheng K, Qi S, Liu H, Jiang Y, Jiang H, et al. Affibody modified and radiolabeled gold-iron oxide hetero-nanostructures for tumor PET, optical and MR imaging. Biomaterials. 2013;34:2796–806.
[133] Hebert EM, Debouttiere PJ, Lepage M, Sanche L, Hunting DJ. Preferential tumour accumulation of gold nanoparticles, visualised by Magnetic Resonance Imaging: radiosensitisation studies in vivo and in vitro. Int J Radiat Biol. 2010;86:692–700.
[134] Liu J, Xiong Z, Zhang J, Peng C, Klajnert-Maculewicz B, Shen M, et al. Zwitterionic gadolinium(III)-complexed dendrimer-entrapped gold nanoparticles for enhanced computed tomography/magnetic resonance imaging of lung cancer metastasis. ACS Appl Mater Interfaces. 2019;11:15212–21.
[135] Zhou B, Xiong Z, Wang P, Peng C, Shen M, Mignani S, et al. Targeted tumor dual mode CT/MR imaging using multifunctional polyethylenimine-entrapped gold nanoparticles loaded with gadolinium. Drug Deliv. 2018;25:178–86.
[136] Xu C, Wang Y, Zhang C, Jia Y, Luo Y, Gao X. AuGd integrated nanoprobes for optical/MRI/CT triple-modal in vivo tumor imaging. Nanoscale. 2017;9:4620–8.
[137] Coughlin AJ, Ananta JS, Deng N, Larina IV, Decuzzi P, West JL. Gadolinium-conjugated gold nanoshells for multimodal diagnostic imaging and photothermal cancer therapy. Small. 2014;10:556–65.
[138] Pitchaimani A, Duong T, Nguyen T, Maurmann L, Key J, Bossmann SH, et al. Gd(3)(+) tethered gold nanorods for combined magnetic resonance imaging and photo-thermal therapy. J Biomed Nanotechnol. 2017;13:417–26.
[139] Maurer AH. Combined imaging modalities: PET/CT and SPECT/CT. Health Phys. 2008;95:571–6.
[140] National Research C and Institute of Medicine Committee on State of the Science of Nuclear M. The National Academies Collection: Reports funded by National Institutes of Health. Advancing Nuclear Medicine Through Innovation. Washington (DC): National Academies Press (US) National Academy of Sciences; 2007.
[141] Maccora D, Dini V, Battocchio C, Fratoddi I, Cartoni A, Rotili D, et al. Gold Nanoparticles and Nanorods in Nuclear Medicine: A Mini Review, 9; 2019; 3232.
[142] Xie H, Diagaradjane P, Deorukhkar AA, Goins B, Bao A, Phillips WT, et al. Integrin alphavbeta3-targeted gold nanoshells augment tumor vasculature-specific imaging and therapy. Int J Nanomedicine. 2011;6:259–69.
[143] Ng QK, Olariu CI, Yaffee M, Taelman VF, Marincek N, Krause T, et al. Indium-111 labeled gold nanoparticles for in-vivo molecular targeting. Biomaterials. 2014;35:7050–7.
[144] Li X, Xiong Z, Xu X, Luo Y, Peng C, Shen M, et al. (99m)Tc-labeled multifunctional low-generation dendrimer-entrapped gold nanoparticles for targeted SPECT/CT dual-mode imaging of tumors. ACS Appl Mater Interfaces. 2016;8:19883–91.
[145] Zhu J, Zhao L, Yang J, Chen L, Shi J, Zhao J, et al. (99m)Tc-labeled polyethylenimine-entrapped gold nanoparticles with pH-responsive charge conversion property for enhanced dual mode SPECT/CT imaging of cancer cells. Langmuir. 2019;35:13405–12.
[146] Wen S, Zhao L, Zhao Q, Li D, Liu C, Yu Z, et al. A promising dual mode SPECT/CT imaging platform based on (99m)Tc-labeled multifunctional dendrimer-entrapped gold nanoparticles. J Mater Chem B. 2017;5:3810–5.
[147] Zhou B, Wang R, Chen F, Zhao L, Wang P, Li X, et al. (99m)Tc-labeled RGD-polyethylenimine conjugates with entrapped gold nanoparticles in the cavities for dual-mode SPECT/CT imaging of hepatic carcinoma. ACS Appl Mater Interfaces. 2018;10:6146–54.
[148] Xiao Y, Hong H, Matson VZ, Javadi A, Xu W, Yang Y, et al. Gold nanorods conjugated with doxorubicin and cRGD for combined anticancer drug delivery and PET imaging. Theranostics. 2012;2:757–68.
[149] Zhao Y, Pang B, Detering L, Luehmann H, Yang M, Black K, et al. Melanocortin 1 receptor targeted imaging of melanoma with gold nanocages and positron emission tomography. Mol Imaging. 2018;17:1536012118775827.
[150] Karmani L, Bouchat V, Bouzin C, Levêque P, Labar D, Bol A, et al. (89)Zr-labeled anti-endoglin antibody-targeted gold nanoparticles for imaging cancer: implications for future cancer therapy. Nanomedicine. 2014;9:1923–37.
[151] Zhao L, Li Y, Zhu J, Sun N, Song N, Xing Y, et al. Chlorotoxin peptide-functionalized polyethylenimine-entrapped gold nanoparticles for glioma SPECT/CT imaging and radionuclide therapy. J Nanobiotechnol. 2019;17:30.
[152] Cheng Y, Zhu J, Zhao L, Xiong Z, Tang Y, Liu C, et al. (131)I-labeled multifunctional dendrimers modified with BmK CT for targeted SPECT imaging and radiotherapy of gliomas. Nanomedicine. 2016;11:1253–66.
[153] Longmire M, Choyke PL, Kobayashi H. Clearance properties of nano-sized particles and molecules as imaging agents: considerations and caveats. Nanomedicine. 2008;3:703–17.
[154] Grootendorst MR, Cariati M, Kothari A, Tuch DS, Purushotham A. Cerenkov luminescence imaging (CLI) for image-guided cancer surgery. Clin Transl Imaging. 2016;4:353–66.
[155] Rambanapasi C, Barnard N, Grobler A, Buntting H, Sonopo M, Jansen D, et al. Dual radiolabeling as a technique to track nanocarriers: the case of gold nanoparticles. Molecules. 2015;20:12863–79.
[156] Cai Z, Chattopadhyay N, Yang K, Kwon YL, Yook S, Pignol JP, et al. (111)In-labeled trastuzumab-modified gold nanoparticles are cytotoxic in vitro to HER2-positive breast cancer cells and arrest tumor growth in vivo in athymic mice after intratumoral injection. Nucl Med Biol. 2016;43:818–26.
[157] Yook S, Cai Z, Lu Y, Winnik MA, Pignol JP, Reilly RM. Intratumorally injected 177Lu-labeled gold nanoparticles: gold nanoseed brachytherapy with application for neoadjuvant treatment of locally advanced breast cancer. J Nucl Med. 2016;57:936–42.
[158] Mendoza-Nava H, Ferro-Flores G, Ramirez FM, Ocampo-Garcia B, Santos-Cuevas C, Azorin-Vega E, et al. Fluorescent, plasmonic, and radiotherapeutic properties of the (177)Lu-Dendrimer-AuNP-Folate-bombesin nanoprobe located inside cancer cells. Mol Imaging. 2017;16:1536012117704768.
[159] Cai Z, Yook S, Lu Y, Bergstrom D, Winnik MA, Pignol JP, et al. Local radiation treatment of HER2-positive breast cancer using Trastuzumab-modified gold nanoparticles labeled with (177)Lu. Pharm Res. 2017;34:579–90.
[160] Chanda N, Kan P, Watkinson LD, Shukla R, Zambre A, Carmack TL, et al. Radioactive gold nanoparticles in cancer therapy: therapeutic efficacy studies of GA-198AuNP nanoconstruct in prostate tumor-bearing mice. Nanomedicine. 2010;6:201–9.
[161] Shukla R, Chanda N, Zambre A, Upendran A, Katti K, Kulkarni RR, et al. Laminin receptor specific therapeutic gold nanoparticles (198AuNP-EGCg) show efficacy in treating prostate cancer. Proc Natl Acad Sci U S A. 2012;109:12426–31.
[162] Axiak-Bechtel SM, Upendran A, Lattimer JC, Kelsey J, Cutler CS, Selting KA, et al. Gum arabic-coated radioactive gold nanoparticles cause no short-term local or systemic toxicity in the clinically relevant canine model of prostate cancer. Int J Nanomedicine. 2014;9:5001–11.
[163] Al-Yasiri AY, Khoobchandani M, Cutler CS, Watkinson L, Carmack T, Smith CJ, et al. Mangiferin functionalized radioactive gold nanoparticles (MGF-(198)AuNPs) in prostate tumor therapy: green nanotechnology for production, in vivo tumor retention and evaluation of therapeutic efficacy. Dalton Trans. 2017;46:14561–71.
[164] Chakravarty R, Chakraborty S, Guleria A, Kumar C, Kunwar A, Nair KVV, et al. Clinical scale synthesis of intrinsically radiolabeled and cyclic RGD peptide functionalized (198)Au nanoparticles for targeted cancer therapy. Nucl Med Biol. 2019;72-73:1–10.
[165] Moeendarbari S, Tekade R, Mulgaonkar A, Christensen P, Ramezani S, Hassan G, et al. Theranostic nanoseeds for efficacious internal radiation therapy of unresectable solid tumors. Sci Rep. 2016;6:20614.
[166] Salvanou E-A, Stellas D, Tsoukalas C, Mavroidi B, Paravatou-Petsotas M, Kalogeropoulos N, et al. A proof-of-concept study on the therapeutic potential of au nanoparticles radiolabeled with the alpha-emitter Actinium-225. Pharmaceutics. 2020;12:188.
[167] Laprise-Pelletier M, Ma Y, Lagueux J, Cote MF, Beaulieu L, Fortin MA. Intratumoral injection of low-energy photon-emitting gold nanoparticles: a microdosimetric Monte Carlo-based model. ACS Nano. 2018;12:2482–97.
[168] Ghorbani M, Bakhshabadi M, Golshan A, Knaup C. Dose enhancement by various nanoparticles in prostate brachytherapy. Australas Phys Eng Sci Med. 2013;36:431–40.
[169] Cho SH. Estimation of tumour dose enhancement due to gold nanoparticles during typical radiation treatments: a preliminary Monte Carlo study. Phys Med Biol. 2005;50:N163–73.
[170] Cho SH, Jones BL, Krishnan S. The dosimetric feasibility of gold nanoparticle-aided radiation therapy (GNRT) via brachytherapy using low-energy gamma-/x-ray sources. Phys Med Biol. 2009;54:4889–905.
[171] Ngwa W, Makrigiorgos GM, Berbeco RI. Applying gold nanoparticles as tumor-vascular disrupting agents during brachytherapy: estimation of endothelial dose enhancement. Phys Med Biol. 2010;55:6533–48.
[172] Yoon M, Cho S, Jeong H, Kim CH. Monte Carlo simulation study on dose enhancement by gold nanoparticles in brachytherapy. J Korean Phys Soc. 2010;56:1754–8.

[173] Ngwa W, Makrigiorgos GM, Berbeco RI. Gold nanoparticle-aided brachytherapy with vascular dose painting: estimation of dose enhancement to the tumor endothelial cell nucleus. Med Phys. 2012;39:392–8.
[174] Bahreyni Toossi MT, Ghorbani M, Mehrpouyan M, Akbari F, Sobhkhiz Sabet L, Soleimani Meigooni A. A Monte Carlo study on tissue dose enhancement in brachytherapy: a comparison between gadolinium and gold nanoparticles. Australas Phys Eng Sci Med. 2012;35:177–85.
[175] Roeske JC, Nunez L, Hoggarth M, Labay E, Weichselbaum RR. Characterization of the theorectical radiation dose enhancement from nanoparticles. Technol Cancer Res Treat. 2007;6:395–401.
[176] Khodadadi A, Nedaie HA, Sadeghi M, Ghassemi MR, Mesbahi A, Banaee N. Determination of the dose enhancement exclusively in tumor tissue due to the presence of GNPs. Appl Radiat Isot. 2019;145:39–46.
[177] Amato E, Italiano A, Pergolizzi S. Gold nanoparticles as a sensitising agent in external beam radiotherapy and brachytherapy: a feasibility study through Monte Carlo simulation. Int J Nanotechnol. 2013;10:1045–54.
[178] Al-Musywel HA, Laref A. Effect of gold nanoparticles on radiation doses in tumor treatment: a Monte Carlo study. Lasers Med Sci. 2017;32:2073–80.
[179] Rezaei H, Zabihzadeh M, Ghorbani M, Goli Ahmadabad F, Mostaghimi H. Evaluation of dose enhancement in presence of gold nanoparticles in eye brachytherapy by 103Pd source. Australas Phys Eng Sci Med. 2017;40:545–53.
[180] Asadi S, Vaez-Zadeh M, Vahidian M, Marghchouei M, Masoudi SF. Ocular brachytherapy dosimetry for 103Pd and 125I in the presence of gold nanoparticles: a Monte Carlo study. J Appl Clin Med Phys. 2016;17:90–9.
[181] Lechtman E, Chattopadhyay N, Cai Z, Mashouf S, Reilly R, Pignol JP. Implications on clinical scenario of gold nanoparticle radiosensitization in regards to photon energy, nanoparticle size, concentration and location. Phys Med Biol. 2011;56:4631–47.
[182] Ghorbani M, Pakravan D, Bakhshabadi M, Meigooni A. Dose enhancement in brachytherapy in the presence of gold nanoparticles: a Monte Carlo study on the size of gold nanoparticles and method of modelling. Nukleonika. 2012;57:401–6.
[183] Jones BL, Krishnan S, Cho SH. Estimation of microscopic dose enhancement factor around gold nanoparticles by Monte Carlo calculations. Med Phys. 2010;37:3809–16.
[184] Zhang SX, Gao J, Buchholz TA, Wang Z, Salehpour MR, Drezek RA, et al. Quantifying tumor-selective radiation dose enhancements using gold nanoparticles: a Monte Carlo simulation study. Biomed Microdevices. 2009;11:925–33.
[185] Asadi S, Vaez-zadeh M, Masoudi SF, Rahmani F, Knaup C, Meigooni AS. Gold nanoparticle-based brachytherapy enhancement in choroidal melanoma using a full Monte Carlo model of the human eye. J Appl Clin Med Phys. 2015;16:344–57.
[186] Brivio D, Nguyen PL, Sajo E, Ngwa W, Zygmanski P. A Monte Carlo study of I-125 prostate brachytherapy with gold nanoparticles: dose enhancement with simultaneous rectal dose sparing via radiation shielding. Phys Med Biol. 2017;62:1935–48.
[187] Khosravi H, Hashemi B, Rahmani F, Ebadi A. Investigation of the gold nanoparticles effects on the prostate dose distribution in brachytherapy: gel dosimetry and Monte Carlo method. J Contemp Brachytherapy. 2016;8:422–8.
[188] Shahhoseini E, Ramachandran P, Patterson WR, Geso M. Determination of dose enhancement caused by AuNPs with Xoft(®) Axxent(®) Electronic (eBxTM) and conventional brachytherapy: in vitro study. Int J Nanomedicine. 2018;13:5733–41.
[189] Ngwa W, Korideck H, Kassis AI, Kumar R, Sridhar S, Makrigiorgos GM, et al. In vitro radiosensitization by gold nanoparticles during continuous low-dose-rate gamma irradiation with I-125 brachytherapy seeds. Nanomedicine. 2013;9:25–7.
[190] Khoo AM, Cho SH, Reynoso FJ, Aliru M, Aziz K, Bodd M, et al. Radiosensitization of prostate cancers in vitro and in vivo to erbium-filtered orthovoltage X-rays using actively targeted gold nanoparticles. Sci Rep. 2017;7:18044.
[191] Le Goas M, Paquet M, Paquirissamy A, Guglielmi J, Compin C, Thariat J, et al. Improving (131)I radioiodine therapy by hybrid polymer-grafted gold nanoparticles. Int J Nanomedicine. 2019;14:7933–46.
[192] Zhang F, Han X, Hu Y, Wang S, Liu S, Pan X, et al. Interventional photothermal therapy enhanced brachytherapy: a new strategy to fight deep pancreatic cancer. Adv Sci. 2019;6:1801507.
[193] Lai P, Lechtman E, Mashouf S, Pignol JP, Reilly RM. Depot system for controlled release of gold nanoparticles with precise intratumoral placement by permanent brachytherapy seed implantation (PSI) techniques. Int J Pharm. 2016;515:729–39.
[194] Lai P, Cai Z, Pignol JP, Lechtman E, Mashouf S, Lu Y, et al. Monte Carlo simulation of radiation transport and dose deposition from locally released gold nanoparticles labeled with (111)In, (177)Lu or (90)Y incorporated into tissue implantable depots. Phys Med Biol. 2017;62:8581–99.
[195] Sinha N, Cifter G, Sajo E, Kumar R, Sridhar S, Nguyen PL, et al. Brachytherapy application with in situ dose painting administered by gold nanoparticle eluters. Int J Radiat Oncol Biol Phys. 2015;91:385–92.
[196] Cui L, Her S, Borst GR, Bristow RG, Jaffray DA, Allen C. Radiosensitization by gold nanoparticles: will they ever make it to the clinic? Radiother Oncol. 2017;124:344–56.